Technische Universität München
TUM School of Medicine and Health

Bio-engineering of *in-vitro* vascularized 3D tissue models in context of metabolic syndrome and obesity

Maren Marder

Vollständiger Abdruck der von der TUM School of Medicine and Health der Technischen Universität München zur Erlangung einer

Doktorin der Naturwissenschaften (Dr. rer. nat.)

genehmigten Dissertation.

Vorsitz: Prof. Dr. Alessandra Moretti

Prüfende der Dissertation:

1. Prof. Dr. Matthias Meier

2. Prof. Dr. Martin Klingenspor

Die Dissertation wurde am 29.01.2025 bei der Technischen Universität München eingereicht und durch die TUM School of Medicine and Health am 18.06.2025 angenommen.

Eidesstaatliche Erklärung

Ich, Maren Marder, erkläre an Eides statt, dass ich die bei der promotionsführenden Einrichtung

der TUM zur Promotionsprüfung vorgelegte Arbeit mit dem Titel:

"Bio-engineering of *in-vitro* vascularized 3D tissue models in context of metabolic syndrome and obesity"

unter der Anleitung und Betreuung durch: Prof Dr. Matthias Meier

ohne sonstige Hilfe erstellt und bei der Abfassung nur die gemäß § 7 Abs. 6 und 7 angegebenen Hilfsmittel benutzt habe.

☒ Ich habe keine Organisation eingeschaltet, die gegen Entgelt Betreuer*innen für die Anfertigung von Dissertationen sucht, oder die mir obliegenden Pflichten hinsichtlich der Prüfungsleistungen für mich ganz oder teilweise erledigt.

☒ Ich habe die Dissertation in dieser oder ähnlicher Form in keinem anderen Prüfungsverfahren als Prüfungsleistung vorgelegt.

☒ Teile der Dissertation wurden in Marder and Remmert et al.,2024 veröffentlicht.

☒ Ich habe den angestrebten Doktorgrad noch nicht erworben und bin nicht in einem früheren Promotionsverfahren für den angestrebten Doktorgrad endgültig gescheitert.

☐ Ich habe bereits am _____ bei der promotionsführenden Einrichtung _____ der Hochschule _____ unter Vorlage einer Dissertation mit dem Thema _____

die Zulassung zur Promotion beantragt mit dem Ergebnis:

_____

☒ Ich habe keine Kenntnis über ein strafrechtliches Ermittlungsverfahren in Bezug auf wissenschaftsbezogene Straftaten gegen mich oder eine rechtskräftige strafrechtliche Verurteilung mit Wissenschaftsbezug.

Die öffentlich zugängliche Promotionsordnung sowie die Richtlinien zur Sicherung guter wissenschaftlicher Praxis und für den Umgang mit wissenschaftlichem Fehlverhalten der TUM sind mir bekannt, insbesondere habe ich die Bedeutung von § 27 PromO (Nichtigkeit der Promotion) und § 28 PromO (Entzug des Doktorgrades) zur Kenntnis genommen. Ich bin mir der Konsequenzen einer falschen Eidesstattlichen Erklärung bewusst.

Mit der Aufnahme meiner personenbezogenen Daten in die Alumni-Datei bei der TUM bin ich

☒ einverstanden, ☐ nicht einverstanden.

München, 26.01.2025

Ort, Datum, Unterschrift

Acknowledgements

First of all, I would like to thank my supervisor Prof. Dr. Matthias Meier who gave me the opportunity to research in the fascinating field of bioengineering. He encouraged me to think interdisciplinary and to broaden my biologic background for exploiting data science. I enjoyed his scientific input and help where I needed it by prospering my creativity, my confidence and my autonomy for finding scientific solutions on my own.

Next, I sincerely would like to thank Prof. Dr. Martin Klingenspor for supervising my thesis at University of Munich. He together with my mentor, Prof. Dr. Anja Zeigerer, contributed significantly to the fruitful scientific feedback sessions at the Thesis Advisory Committee meetings.

Next, I am incredibly grateful to the whole Meier lab for making these 3.5 years to such a great experience. I enjoyed the team spirit of each team member in professional and in personal support manner with a lot of fun through my whole thesis: Alina Platen, Dr. Scott Atwell, Dr. Nina Huber, Dr. Johannes Wirth, Jessi Ardila, Sophie Dengler, Dr. Simon Rosowski, Dr. Nico Laumann-Lipp, Stefan Veit, Revanth Coimbatore Varadarajan, Che-Wei Chang, Dr. Magdalena Motz, Dr. Sandra Wiedenmann, Daniel Kokotek, Julius A. Perschel, Dr. Caroline Remmert, Munkhtur Otgonbayar, Zoë Kentischer, Débora Pino García, Lucie Angevin, Yiran Zheng, Naeimeh Hosseini.

My special thanks go to “Maro” describing my outstanding teamwork and lab partnership with Caroline Remmert. Every up and down in our vessel-on-chip project was mastered way better together with you. Furthermore, Julius A. Perschel and Munkhtur Otgonbayar have greatly contributed with their engineering skills and creative ideas to the project. Julius A. Perschel, our encyclopedia, always knows a state-of-the-art tool for any research purpose. And Munkhtur Otgonbayar remembered me to have fun, even on the most stressful day in the lab, always having a little joke on his mind. Next, I would like to thank Dr. Johannes Wirth who helped when I was stuck in coding. An outstanding regard goes to Daniel Kokotek as “Papa single-cell” who patiently taught and helped me with scRNAseq pre- and postprocessing pipeline. I would like to mention my mentee Zoë Kentischer who eagerly soaked up any knowledge I could transfer to her and helped me during my last three very lab-work-intensive months. Finally, my special thanks goes to Dr. Sandra Wiedenmann, meanwhile she is our lab mom, supporting me with her scientific, programming, PhD career and personal experience wherever she can. Our lab is inconceivable without

our lab manager Alina Platen. She taught me a lot about generic lab basics and stem cell cultivation and provided great help in any bureaucratic organization.

Also within the Helmholtz Munich environment, I express my great thanks to Dr. Celia Martinez and her lab members Dr. Giannis K. Deligiannis and Mateusz Strzelecki for providing me their expertise and enduring practical help with the extraction and sequencing of nuclei. Then, I would like to mention the great support with cryo-preparations by Dr. Annette Feuchtinger and her team. Also, the mass-spectrometry team of Dr. Stephanie Hauck, especially Dr. Christine von Toerne who joyful supported with her knowledge in proteomic data analysis.

An outstanding regard goes to my cooperation partners at HI-MAG in Leipzig, especially Dr. Bilal Sheikh who brought fresh ideas into both of the projects and he and his group warmly welcomed me for a research visit in their lab in Leipzig. I am very grateful for Fabiana Oliveira's support with the experimental burden of the knockdown-subproject.

I also would like to thank for the cooperation with Dr. Maria Rohm who encouraged for the interesting cooperation in the cancer cachexia subproject in tight co-work with her team member Tuna F Samanci. Although we did not get publishable data yet, I very much appreciate their expertise in adipose tissue field which I could also transfer to my main project.

A big hug goes out to my friends for cheering me up, distracting me and generally supporting me through the whole time. Last, but not least, I very much need to express the appreciation for my family, for my Dad from whom I inherited my thirst for knowledge, my loving Mum, for my brother and my sister who are always there for me.

Table of Contents

Publications during the doctoral studies

During my doctoral researcher period, following papers have been published or have been submitted:

(1) Rosowski Simon, Remmert Caroline, **Marder Maren**, Akishiba Misao, Bushe Judith, Feuchtinger Annette, Platen Alina, Ussar Siegfried, Theis Fabian, Wiedenmann Sandra, Meier Matthias#. Single-cell characterization of neovascularization using hiPSC-derived endothelial cells in a 3D microenvironment. **Stem Cell Reports**. 2023 Oct, 18(10):1972-1986. doi: 10.1016/j.stemcr.2023.08.008.[1]

(2) **Marder Maren***, Remmert Caroline*, Perschel Julius A, Otgonbayar Munkhtur, von Toerne Christine, Hauck Stefanie, Bushe Judith, Feuchtinger Annette, Sheikh Bilal, Moussus Michel, Meier Matthias#. Stem cell-derived vessels-on-chip for cardiovascular disease modeling. Cell Rep. 2024 Apr, 43(4):114008. doi: 10.1016/j.celrep.2024.114008.[2]

(3) Remmert Caroline, Otgonbayar Munkhtur, **Marder Maren**, Perschel Julius A, Meier Matthias#. Protocol to generate a microfluidic vessels-on-chip platform using human pluripotent stem cell-derived endothelial cells. STAR Protoc. 2024 Sep 20;5(3):103300. doi: 10.1016/j.xpro.2024.103300.[3]

(4) **Marder Maren***, Wiedenmann Sandra, Oliveira Fabiana, Kentischer Zoë E., Remmert Caroline, Zheng Yiran, Sheikh Bilal, Meier Matthias#. Human vascularized adipose tissue organoids reveal endothelial-adipocyte interactions at single-cell resolution. Manuscript is submitted.

* First-author or first author co-contribution

Corresponding author

In this thesis, original data from Marder and Remmert, et al. (2) were presented as well as from the submitted manuscript of Marder, et al. (4).

Zusammenfassung

Das endotheliale Blutgefäßsystem ist für den Transport von Sauerstoff und Nährstoffen im ganzen Körper unverzichtbar und sorgt so für die Homöostase jedes Organs. Blutgefäße sind in räumlicher, funktioneller und strömungsmechanischer Dimension hochgradig organisiert. Diese Komplexität erschwert die Untersuchung von Gefäßen im gesunden und veränderten Zustand bei Herz-Kreislauf-Erkrankungen. Daher sind *in-vitro* Humanmodelle, die diese Vielschichtigkeit nachbilden und der *in-vivo* Situation ähneln, sehr gefragt. Insbesondere die Schaffung einer physiologischen Umgebung, die die extrazelluläre Matrix widerspiegelt, steht zunehmend im Fokus und soll durch dreidimensional wachsende Zellkulturen als Fortschritt gegenüber der konventionellen Einzellschichtkultur gelöst werden. Mikrofluidische Organ-Chip-Systeme haben sich in jüngster Zeit als vielversprechende Plattformen für die Erzeugung von Endothellumen herausgestellt, die in eine dreidimensionale physiologische Umgebung eingebettet und unter Blutperfusionsfluss gestellt werden. In dieser Arbeit wurde ein perfundiertes Gefäß-Chip-System entwickelt, das im Vergleich zu einem statischen System verbesserte endotheliale Funktionen wie Migration, Diffusionsbarriere und Stickstoffmonoxid-Synthese zeigt. Zudem zeigte die Einzelzell-RNA Sequenzierungsanalyse der organtypischen, strömungsinduzierten Gefäße eine erhöhte transkriptionelle Ähnlichkeit zu Gefäßen *in-vivo* auf. Herz-Kreislauf-Erkrankungen sind eine Untergruppe von Erkrankungen des Gefäßsystems, die stark mit dem metabolischen Syndrom korrelieren. Konstanter Nahrungsüberschuss, geringe körperliche Aktivität und genetische Prädisposition führen zu Stoffwechselstörungen wie Adipositas und Diabetes mellitus Typ 2 mit weltweit zunehmender Inzidenz. Metabolisches Ungleichgewicht im Gefäßsystem manifestiert sich deutlich in Atherosklerose, einem fibrotisch-entzündlichen Prozess, der die Gefäßlumen durch Ansammlung von fettspeichernden und nekrotisierenden Zellen in der Gefäßwand verengt. Im Rahmen dieser Arbeit wurden initiale pro-atherosklerotische Prozesse auf der organtypischen Gefäßplattform durch Induktion von oxidativem Stress, als ein ursächlicher Auslöser von Atherosklerose, untersucht. Das System spiegelte krankheitsbedingte Veränderungen im Proteom und Sekretom, aber auch auf funktioneller Ebene durch eine verminderte endotheliale Stickstoffmonoxid-Produktion glaubwürdig wider. Zusammengenommen erwies sich der mikrofluidische Gefäß-Chip als vielseitiges Werkzeug für die hochskalierbare,

kostengünstige und zeiteffiziente Herstellung von *in-vitro*-Endothelgefäßen mit einer Bandbreite an Analyseoptionen zur Untersuchung von Herz-Kreislauf-Erkrankungen.

Es steht im starken Interesse, Blutgefäße nicht nur isoliert, sondern auch im Zusammenhang mit der Organfunktion bei Stoffwechselerkrankungen, zum Beispiel im Fettgewebe, zu untersuchen. Das Fettgewebe ist der Hauptspeicher für energiehaltige Fettdepots im Körper, aber seine funktionelle Rolle bei der metabolischen und hormonellen Homöostase des gesamten Körpers hat zunehmend an Bedeutung gewonnen. Während der weiße Subtyp hauptsächlich die Energiespeicherfunktion abdeckt, rückten braunes und beiges Fett mit ihrer energieverbrennenden und wärmeproduzierenden Funktion in den Fokus zur Intervention des metabolischen Syndroms. Immer mehr Forschungsergebnisse untermauern das funktionale Zusammenspiel von Fettgewebe und dem umgebenden Endothel im gesunden Zustand, aber auch bei Adipositas. Daher besteht eine hohe Nachfrage nach dreidimensionalen *in-vitro*-Modellen von vaskularisiertem Fettgewebe, die es ermöglichen, physiologische Zusammenhänge in einem kontrollierten Versuchsaufbau zu untersuchen. In dieser Arbeit habe ich ein vaskularisiertes Fettgewebsmodell in einem dreidimensionalen Format mit hoher Reproduzierbarkeit entwickelt. Die selbstorganisierende Ko-Kultur von Endothelzellen und Fettzellen (Adipozyten) entwickelte sich zu gewebsdichten Organoiden nach Einbettung in eine physiologische Matrix. Die Organoide zeigten ein komplex ausgebildetes Gefäßnetzwerk und eine zunehmende Größe der Fetttröpfchen auf, charakteristisch für *in-vivo* gereifte weiße, unilokulare Adipozyten. Sowohl das Endothel als auch Adipozyten trugen zur Glukoseaufnahme in das Fettgewebe bei, und die ß-adrenerge Lipolyse war im vaskularisierten Modell im Vergleich zu einer nicht-vaskularisierten Kontrolle stimuliert. Das Einzelzell-Transkriptom der vaskularisierten Fettgewebsorganoide zeigte Ähnlichkeiten zu perivaskulären Fettgewebs-Vorläuferzellen mit beigen Differenzierungspotential *in-vivo* auf, sowie eine Reifung der Endothelzellen in der Umgebung der Adipozyten. Damit erwies diese Studie einen Neuheitsstatus in der tieferen transkriptionellen Charakterisierung eines *in-vitro* vaskularisierten Fettgewebsmodels. Ein endothelspezifischer Knockdown von *PDGFB* führte zu einer Dissoziation perivaskulär angelagerter glatter Muskelzellen, begleitet von einer gestörten Regulation der Lipolyse in Adipozyten. Zusammengenommen erwies sich das vaskularisierte Fettgewebsmodell als wertvolles Instrument zur Untersuchung des Zusammenspiels von Vaskularisierung

und Fettgewebe im gesunden Zustand als auch in Zukunft im Kontext des metabolischen Syndroms und Adipositas. Ein Ziel wäre es, das Gefäß-Chip-System mit den vaskularisierten Fettgewebe-Organoiden zu kombinieren, um zukünftig eine umfassende Fettgewebsplattform mit organrelevanter Perfusion zu schaffen.

Summary

The endothelial blood vessel system is indispensable for the transport of oxygen and nutrients throughout the whole body thus providing homeostasis of any organ. Blood vessels are highly organized in spatial, functional and flow-mechanical dimension. This complexity aggravates investigating vessels in health and in cardiovascular disease. Thus, *in-vitro* human models reflecting this intricacy and resembling the *in-vivo* situation are in high demand. Especially, the creation of a physiologic environment reflecting extracellular matrix is in increasing focus and to be solved by three dimensionally growing cell cultures as advancement over conventional monolayer cultivated cells. Microfluidic organ-on-chips have recently emerged as promising platforms for creating endothelial lumen embedded in a three dimensional physiologic environment and set under blood perfusion flow. In this thesis, a perfused endothelial vessel-on-chip system was engineered showing enhanced endothelial function like sprouting capability, barrier integrity and nitric oxide synthesis in comparison to a static system. Single cell RNA sequencing analysis of the organotypic, flow-induced vessels revealed increased *in-vivo* transcriptomic resemblance. Cardiovascular disease is a subset of circulatory disorders strongly correlated with metabolic syndrome. Nutritional excess, low corporal activity and genetic traits lead to metabolic disturbances as in obesity and Type 2 Diabetes Mellitus with increasing incidence worldwide. Metabolic disbalance of the vessel system prominently manifests in atherosclerosis, a fibrotic-inflammatory process narrowing the luminal tube through accumulation of fat-storing and necrotizing cells in the vessel wall. During this thesis, the on-set of atherosclerosis was studied on the organotypic vessel platform through oxidative stress induction, a key initiation process in atherosclerosis. The system credibly reflected disease-related alterations in proteome and secretome but also on functional level through diminished endothelial nitric oxide production. In summary, the microfluidic vessel-on-chip evinced as versatile tool for highly scalable, cost- and time-effective production of *in-vitro* endothelial vessels with various downstream analysis options for studying cardiovascular disease.

Blood vessels are of interest to be studied not only singularly but in the context of organ function in metabolic disease, for example in adipose tissue. Adipose tissue is the main storage of energy containing fat depots in the body but its functional role has emerged increasing importance in metabolic and hormonal homeostasis of the whole body.

Whereas the white subtype mainly covers energy storing function, brown and beige fat has come into focus for metabolic syndrome intervention with their energy-burning thermogenic function. More and more evidence pronounces the interplay of adipocytes and their surrounding endothelium in health state but also during obesity. Thus, there is a high demand of three dimensional *in-vitro* models of vascularized adipose tissue allowing the examination of physiologic coherences in a controlled set-up. In this thesis, I engineered a vascularized model of adipose tissue in a three dimensional format with high reproducibility. The self-assembling co-culture of endothelial cells and adipocytes developed towards dense organoids when embedded in a physiologic matrix. The organoids displayed expanded endothelial network formation and increasing adipocyte lipid droplet size as a sign of *in-vivo* matured white, unilocular adipocytes. Both endothelium and adipocytes contributed to glucose uptake into adipose tissue and ß-adrenergic lipolysis was stimulated in the vascularized model in comparison to a non-vascularized control. The single-cell transcriptome of vascularized adipose tissue organoids showed similarities to progenitor cells from perivascular fat with beige differentiation potential *in vivo* whilst endothelial cells underwent increased maturation in the adipocyte environment. This study demonstrated a novelty status in the deeper transcriptional characterization of an *in-vitro* vascularized fat model. An endothelial-specific knockdown of *PDGFB* lead to dissociation of perivascular smooth muscle cells accompanied by impaired adipocyte lipolysis. Taken these results together, vascularized adipose tissue organoids proved as valuable tool to study vascularization of adipose tissue in context of health and metabolic syndrome-related complications as obesity in the future. One objective would be to combine the vessel-on-chip system with the vascularized adipose tissue organoids to create a comprehensive adipose tissue platform with relevant organ perfusion in follow-up studies.

Glossary

General abbreviations

Abbreviation	Definition
2D	Two dimensional
3D	Three dimensional
ADM	Adipocyte differentiation medium
AT	Adipose tissue
BAT	Brown adipose tissue
CI	Confidence interval
CLSM	Confocal laser scanning microscopy
CVD	Cardiovascular disease
DEG	Differentially expressed genes
DEP	Differentially expressed proteins
EC	Endothelial cells
ECGM	Endothelial cell growth medium (StemPro-34 based)
ECM	Extracellular matrix
EGM	Endothelial growth medium (Lonza)
ELISA	Enzyme-linked immunosorbent assay
FACS	Fluorescence activated cell sorting
FAP	Fibro-adipogenic progenitor
FC	Flow cytometry
FDR	False discovery rate
FFA	Free fatty acids
GO-term	Gene ontology term
hASC	Human adipose derived stem cells
hiPSC	Human induced pluripotent stem cells
HUVEC	Human umbilical vein endothelial cells
IF	Immunofluorescence
IHC-Frz	Immunohistochemistry on frozen sections
IHC-P	Immunohistochemistry on paraffin-embedded sections
IHC-Whmt	Immunohistochemistry on whole-mount samples
LC-MS/MS	Liquid chromatography-tandem mass spectrometry

Abbreviation	Definition
LDL	Low density lipoprotein
MHO	Metabolically healthy obesity
AO	Non-vascularized adipose tissue model (mono-culture)
mRNA	Messenger RNA
MUHO	Metabolically unhealthy obesity
NO	Nitric oxide
OoC	Organ-on-chip
oxLDL	Oxidized LDL
PA	Preadipocytes
PCR	Polyermase chain reaction
PVAT	Perivascular adipose tissue
ROS	Reactive oxygen species
RPM	Revolutions per minute
RT	Room temperature
SAT	Subcutaneous (white) adipose tissue
SC-EC	HiPSC-derived endothelial cells
scRNAseq	Single cell RNA sequencing
shRNA	Short hairpin RNA
SMC	Smooth muscle cells
snRNAseq	Single nuclei RNA sequencing
SVF	Stromal vascular fraction from AT
T2DM	Type 2 Diabetes Mellitus
UMAP	Uniform Manifold Approximation and Projection
UMI	Unique molecular identifier
vAO	Vascularized adipose tissue model (co-culture)
vSVFO	Vascularized stromal vascular fraction model (undifferentiated co-culture)
VAT	Visceral (white) adipose tissue
vWAT	Vascularized white adipose tissue model
WAT	White adipose tissue
WSS	Wall shear stress

Gene/Protein names

Abbreviation	Definition
ACTA2/αSMA	Alpha smooth muscle actin
ADIPOQ	Adiponectin
AEBP1	Adipocyte enhancer binding protein 1
ANGPT2	Angiopoietin 2
ANXA2	Annexin 2
APOA1	Apolipoprotein A1
APOC3	Apolipoprotein C3
APOD	Apolipoprotein D
ARP3	Actin related protein 3
BGN	Biglycan
BMP4	Bone morphogenic protein 4
C/EBPα/CEBPA	CCAAT/enhancer-binding protein alpha
C/EBPß/CEBPB	CCAAT/enhancer-binding protein beta
C/EBPδ/CEBPD	CCAAT/enhancer-binding protein delta
CADM	Cell adhesion molecule/nectin-like
CAMK2D	Ca-dependent protein kinase II delta
CAV1	Caveolin-1
CD81	CD81 surface molecule
CFD	Adipsin
CTSB	Cathepsin B
CTSL	Cathepsin L
CYCS	Cytochrom C, somatic
CYGB	Cytoglobin B
DCN	Decorin
DLL4	Delta like canonical notch ligand 4
ENO1	Enolase 1
FABP4	Fatty acid binding protein 4
FGF-2	Fibroblast growth factor 2
FLNA	Filamin A
GLUT	Glucose uptake transporter
HIF	Hypoxia-inducible factor

Abbreviation	Definition
HMOX1	Heme oxygenase 1
IGFBP7	Insulin-like growth factor-binding protein 7
IL6	Interleukin 6
KLF2	Krueppel-like factor 2
KLF4	Krueppel-like factor 4
LGALS1	Galectin-1
LMO4	LIM domain only 4
LPL	Lipoprotein lipase
LTBP1	Latent transforming growth factor beta binding protein 1
MECOM	MDS1 and EVI1 complex locus
MGP	Matix gla protein
MMP9	Matrix-metallopeptidase 9
NDUFB4	NADH:Ubiquinone oxidoreductase subunit B4
NOS3	Nitric oxide synthase
NOSIP	Nitric oxide synthase interacting protein
NOSTRIN	Nitric oxide synthase traffic inducer
NQO1	NAD(P)H Quinone dehydrogenase 1
PDGFB	Platelet derived growth factor subunit B
PDGFRα/PDGFRA	Platelet-derived growth factor receptor alpha
PDGFRβ/CD140b/PDGFRB	Platelet-derived growth factor receptor beta
PEAK1	Pseudopodium-enriched atypical kinase 1
PECAM1/CD31	Platelet/Endothelial cell adhesion molecule 1
POSTN	Periostin
PPARγ/PPARG	Peroxisome proliferator-activated receptor gamma
SCD	Fatty-acid desaturase
SORCS2	Sortilin related VPS10 domain containing receptor 2
TAGLN	Transgelin
TGFB1	Transforming growth factor beta 1
TLR 4	Toll-like receptor 4
UNC5B	Unc-5 netrin receptor B
VASH1	Vasohibin 1

Abbreviation	Definition
VCAN	Versican
VE-Cadherin/CDH5	Vascular endothelial cadherin
VEGF	Vascular endothelial growth factor
VEGFA	Vascular endothelial growth factor A
VEGFR	Vascular endothelial growth factor receptor

Chemicals

Abbreviation	Definition
2-DG	2-Deoxyglucose
BODIPY	4,4-difluoro-1,3,5,7,8- pentamethyl-4-bora-3a, 4a-diaza-s-indacene
BSA	Bovine serum albumin
DAPI	4',6-diamidino-2-phenylindole
DMSO	Dimethyl sulfoxide
KR-buffer	Krebs-Ringer buffer
DMEM	Dulbecco’s modified eagle medium
EDTA	Ethylenediaminetetraacetic acid
FBS	Fetal bovine serum
FITC	Fluorescein
HB buffer	Homogenization buffer
NaOH	Sodium hydroxide
P/S	Penicillin/Streptomycin
PBS	Phosphate buffered saline
PDMS	Polydimethylsiloxan
PE	Phycoerythrin
PFA	Paraformaldehyde
TBHP	Tert-Butylhydroperoxid
TY52156	Sortilin pathway inhibitor

List of figures

List of supplemental figures

1 Introduction

1.1 The endothelial blood vessel

1.1.1 Blood vessel structure and function

Endothelial vessels transport blood pumped from the heart towards peripheral organs and tissues providing life-sustaining oxygen and nutrient transport[4]. Vessels follow a hierarchical structure from large arteries near the heart to small arterioles ending into the capillary bed in organs where substrate exchange takes place[5]. Blood vessels (**Figure 1**) are of luminal shape and larger arteries typically consist of three layers, called tunica intima, media and adventitia[4]. Most prominent is the inner intima, formed by endothelial cells (ECs). This cell type is in direct blood contact and responsible for exchange between blood and the targeted tissue[4]. Endothelium forms a semi-selective barrier between blood and tissue due to dense cell-cell contacts called tight junctions[6]. Specialized transport mechanism allow selective exchange of substances through endothelium. Being exposed to shear stress, ECs show a polarity and their shape is elongated in flow direction[7]. On their basal side, ECs are anchored as a monolayer on a basement membrane which is aligned to an outer subendothelial connective tissue and the internal elastic lamina[4]. On the tunica media then follow smooth muscle cells (SMCs), which cause contraction or dilation of the vessels influencing the blood pressure[4]. This process is for example regulated by endothelial cells, which produce the gas nitric oxide (NO) acting as relaxant on smooth muscle cells leading to vasodilation[8]. The tunica media and adventitia are separated by the external elastic lamina. The tunica adventitia is mainly composed of connective tissue anchoring the vessel to the periphery[9]. Connective tissue gives structure, protection and support to other tissues and organs. The structure is given by the extracellular matrix (ECM), a densely organized network of proteins. The most abundant ECM protein family are the collagens[9]. Collagens type I,II,III form structural fibrils whereas collagen IV builds the network of endothelial basement membrane[10]. Laminins function as cross-linker of collagen IV.[10] Proteoglycans store water filling ECM space serving as mechanical buffer[10]. Fibronectin helps cells to attach and migrate through the ECM[10]. Coherently, cells express receptors to anchor to ECM proteins, majorly integrin ß1 binding to collagens, fibronectin or laminin[10]. The main cellular regulator of ECM homeostasis are the fibroblasts which not only produce ECM-proteins but also rearrange ECM structure,

called matrix remodeling[11]. Smaller vessels/capillary vessels do not show the classical three layer structure. In thin vessels, the endothelial intimal layer is covered by a cell type called pericyte, which regulates the vasculature tone comparable to SMCs in larger vessels[12]. Apart from that, pericytes are critical for vessel development, maturation and functional properties like barrier integrity[13].

Vessel development is a life-time ongoing physiologic but also pathophysiologic process for example during tumor growth to sustain the malignant expanded tissue. De-novo formation of new vessels from endothelial progenitor cells is called vasculogenesis, whereas the expansion of vessels from existing network is called angiogenesis[14]. Similar to fibroblasts, EC have potent capacity to remodel the surrounding extracellular matrix for protrusion of newly forming endothelial sprouts, called endothelial sprouting[5]. Being in tight contact with organs, tissue-specific endothelial cell types have adapted to the organ's specific structure and function. It is of increasing interest if and how ECs modulate organ function apart from simply being a transport system[15].

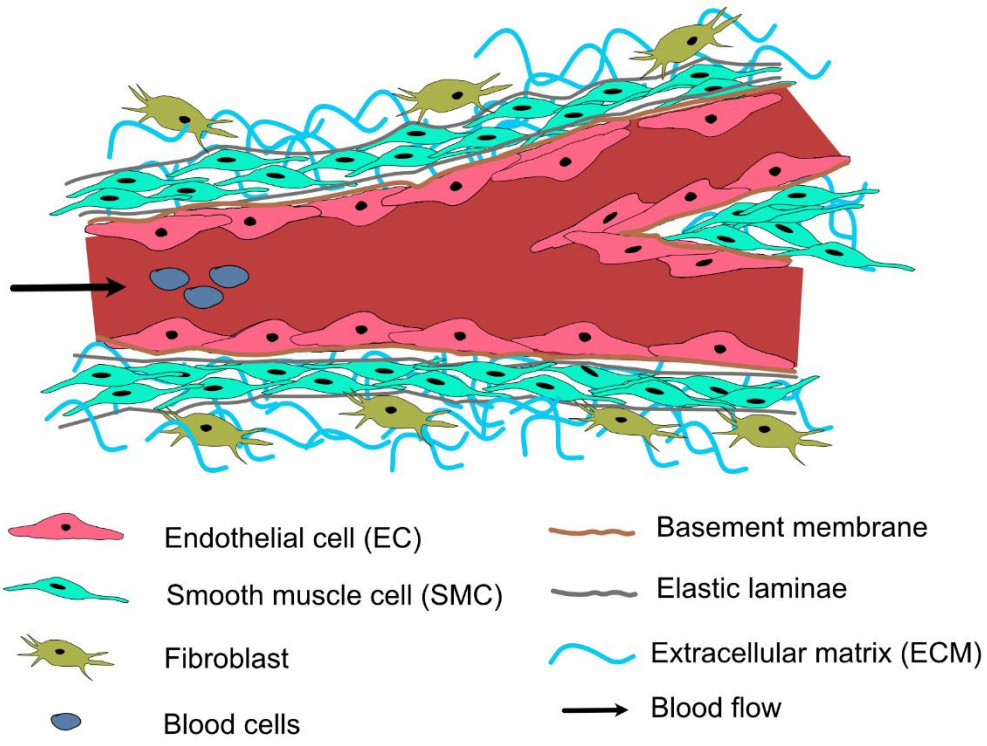

Figure 1 The endothelial blood vessel

Endothelial cells are densely aligned on the basement membrane and form cellular tight junctions to seal the endothelial blood flow from surrounding tissue in the media intima. Blood cells delivering oxygen, immune cells and soluble nutrients are transported along the blood

flow inside the vessel. On the outside of the basement membrane, vascular smooth muscle cells form the media layer and control vascular tone. The tunica adventitia forms connective tissue consisting of fibroblasts and proteins of the extracellular matrix.

1.1.2 Blood vessel alterations in metabolic syndrome and atherosclerosis

One of the major pathologic condition in the 21st century is the metabolic syndrome[16]. The term describes a cluster of impaired metabolic parameters as hyperlipidemia, hypertension, obesity and insulin resistance resulting in type 2 diabetes mellitus (T2DM) and cardiovascular disease (CVD)[16]. Post-industrial life style conditions as low sportive activity and a high-fat and high-sugar containing diet reinforce the condition[16]. Due to the generation of a high inflammatory profile and oxidative stress, metabolic syndrome is strongly associated with endothelial dysfunction and atherosclerotic lesions[17]. Especially, oxidative stress has crucial negative impact on metabolic diseases like obesity, T2DM and CVD. Under physiologic condition, cells permanently produce reactive oxygen species (ROS) as side product of cellular metabolism. Special antioxidant enzymes or other scavenging molecules render these cell-damaging radicals harmless. Under pathophysiologic condition, this homeostasis is shifted towards increased ROS production that harms various cellular structures and processes[18]. In endothelial cells, ROS impair NO synthesis and availability and thus disrupt vascular regulation of vasoconstriction and vasodilation, ending in endothelial dysfunction[19]. For example, elevated free fatty acids (FFA) in plasma, as often observed in obese individuals, are known to increase ROS production in endothelial cells[20].

Atherosclerosis (**Figure 2**) especially happens at specific arterial regions, like curvatures, where low or oscillatory shear stress occurs. Inflammation together with disturbed flow make endothelium vulnerable for lipoproteins accumulating into the intima where they are modified, for example the oxidation of the lipoprotein LDL (low-density-lipoprotein) to oxidized LDL (oxLDL) through ROS. This is the begin of a downstream cascade which activates EC to an inflammatory, activated phenotype recruiting monocytes and other immune cells into the intima. Recruited monocytes differentiate into macrophages and/or vessel-residential macrophages become activated and accumulate cholesterol crystals, a process called foam cell generation. The cholesterol content derives from the internalized and processed lipoproteins, as oxLDL, accompanied by several inflammatory processes. Later, foam cells become

apoptotic or necrotic leading to a necrotic core. Beginning with a fatty streak, a fibrous plaque grows narrowing the blood vessel and subsequent decrease in tissue blood supply. The fibrous plaque is stabilized by SMC migrating from the media to the intima layer and forming an ECM containing fibrous cap. Furthermore, SMC also contribute to foam cell population. In the worst case, an unstable plaque ruptures and floats into the blood stream as thrombus blocking other vessels[19,21]. Ischemic heart disease and stroke make up the largest part of CVD-caused deaths in Europe[22].

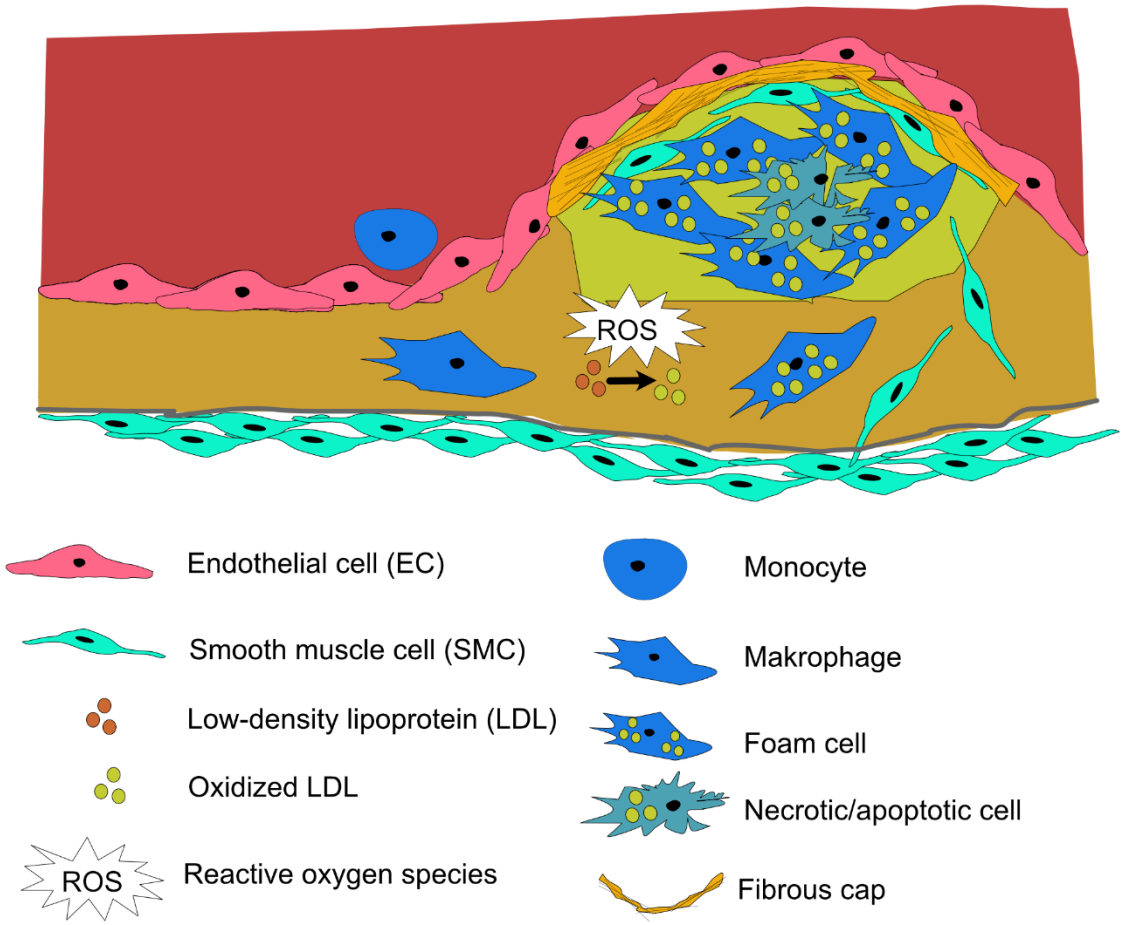

Figure 2 Pathogenesis of atherosclerosis

Initial event in atherosclerosis is the oxidization of LDL to oxLDL in the endothelial intima through ROS. Immune cells like monocytes infiltrate the intima, convert into macrophages and internalize pro-inflammatory oxLDL before further developing into cholesterol filled foam cells. Foam cells accumulate at sites localized under the endothelium forming a fatty streak which is stabilized by a fibrous cap produced by invading SMCs from the media layer. Finally, foam cells die through apoptosis/necrosis, the cell residues form a necrotic core inside the increasing atherosclerotic plaque.

1.2 Modelling blood vessels *in-vitro*

1.2.1 3D reconstruction approaches of blood vessels

The high prevalence of CVD has risen demand for understanding endothelial biology in state of health and disease. As rodent models reach limitations in fully reflecting human vessel biology and raise ethical concerns, alternatively *in-vitro* human cell culture models established as versatile research tool[23]. *In-vitro* models rebuild human EC biology in their complex environment in a simplified set-up but with strictly controllable parameters. Classically, 2D cell culture models growing EC as monolayer require low cell culture effort but do not recapitulate ECs embedded in a three-dimensional (3D) environment. Advanced 2D models may resemble EC luminal shape and polarity creating plastic channels lined with ECs[24]. 3D models are more advanced in reflecting EC sprouting and interaction in a physiologic ECM. Classical 3D models provide a scaffold of synthetic or natural hydrogel wherein EC either can self-assemble to vessels or being seeded into a pre-molded lumen structure[25,26].

Cellular resources for 3D vessel formation are various, primary ECs from the human umbilical vein (HUVEC) are commonly used due to their expandability and an *in-vitro* functionality[25]. In recent years, research sets increasing focus on human induced pluripotent stem cells (hiPSCs) for *in-vitro* vascularization[27]. HiPSCs were reprogrammed from adult human cells to regain pluripotency, the differentiation capacity to all somatic cell types[28]. hiPSC have the advantage over primary cells to proliferate unlimited and allow the upscaling of patient-specific cell material[28]. Efficient differentiation of hiPSC into ECs, here referred to as SC-ECs (stem-cell derived ECs), has been established with EC-specific marker expression and functionality resembling *in-vivo* ECs[29]. Interestingly, during this differentiation protocol, perivascular SMCs are generated as cellular side product, underlining the interdependence of endothelium and surrounding perivascular cells during vessel development and maintenance. Through cell sorting techniques, both cell types can be investigated separately[29].

1.2.2 Microfluidics for mimicking vascular perfusion

Next to the blood pressure, the endothelial luminal wall is exposed to a mechanical force called wall shear stress (WSS) caused by the blood flow[30]. In the field of blood vessel engineering, it is indispensable to implement flow dynamics as ECs highly react

to shear forces. WSS highly differs between vessel location throughout the body, ranging from 10 up to 70 dyn/cm² in some arteries and 1-6 dyn/cm² in veins[31].

Microfluidic chip systems are the method-of-choice when it comes to vessel engineering[32]. Microfluidics is a term for how fluids behave in small dimensions and the development of microfluidic devices adapted to specific applications[33]. Microfabricated vessels-on-chip systems come to application with flow perfusing a microchannel lined with endothelial cells in µm to mm dimension. These chips are mostly polymer-based bodies wherein microchannels are molded[34].

A widely used material for chip engineering is the soft and biocompatible PDMS. The liquid polymer solution is casted on a molding template and after curing process, hardened PDMS represents a replicate of the template with complex and easily customizable 3D structures[34]. The microchannels can either be formed by glueing pre-shaped channel in PDMS on a glass slide and/or by insertion of a needle before curing and removal of the needle after solidification of the polymer[35] (**Figure 3**). Although being very advantageous concerning biocompatibility and fast fabrication, PDMS is permeable for hydrophobic molecules and the soft material tends to defect when removing from the template[34]. Another technique to be presented here is the production of the chip body with integrated microfluidic channels through stereolithography. This technique allows rapid and precise 3D printing as a resin is polymerized with a bundled light source as UV light[34]. Printing resin has to be carefully selected for biocompatibility to avoid cytotoxic effects[34].

As disadvantage, cells growing on a polymer-based surface may not reflect physiologic growth behavior. For generating a more physiologic extracellular environment, recent attempts combined the polymer chip body with a physiologic hydrogel matrix[35]. The microchannel in the hydrogel was also patterned by the needle insertion technique[35].

For flow induction strategy, either active pump systems or passively-driven flow are applied. Pumps provide highly controllable flow parameters but their installation is accompanied by a more extensive effort counteracting high experimental throughput. In contrast, passively-driven flow systems are limited in flow control but their set-up is faster and simplified[36]. Platforms where gravity induces passive flow through a microchannel have recently been realized by rocking shaker solutions[37]. Not only an elaborate pump system but also the production pipeline including the amount of samples per chip may hinder upscaling of experimental throughput. Multi-well

approaches try to overcome this limitation but many of these systems include ECs growing on a lined channel with plastic surface[37]. These systems allow for self-organized sprouting of ECs from the plastic channel towards a centralized physiologic hydrogel[37]. Within this self-organized vessel architecture flow perfusion is less controllable than in pre-patterned endothelial vessels. In future perspective, it may be interesting to create multi-well, scalable platforms with ECs growing in a pre-patterned microlumen embedded in a physiologic matrix.

For deeper downstream analysis, it is essential to manipulate the *in-vitro* system during cell cultivation[38] or to remove the unscathed cellular lumen structure. Many vessel-on-chip systems are designed with a closed surface[35,38,39] alleviating easy manipulation opting for open surface systems as future perspective[38].

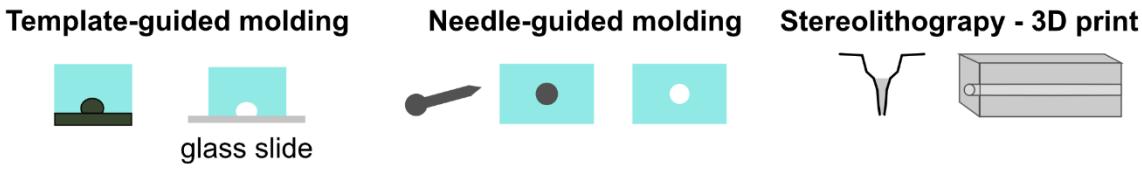

Figure 3 Techniques for channel patterning in microfluidic chip devices

A soft polymer like PDMS can be casted as liquid on a molding template. After solidification of the polymer, the PDMS with prepatterned channel structure can be glued on a glass slide. Another option to pattern PDMS with a microchannel is by implementing a needle before curing process. Needle removal leads to an empty luminal structure within the polymer. By stereolithography, defined 3D structures, like microchannels, can be printed within the chip body.

1.2.3 Cardiovascular disease models

Functionally relevant *in-vitro* vessel models can help to accelerate research in cardiovascular disease, like atherosclerosis. Mouse models may not fully recapitulate human pathophysiology as there is still genetic difference to humans and patho-mechanism between species may vary[40]. Microfluidic human 3D cell culture models are highly versatile to study especially early disease processes like the on-set of atherosclerotic lesions in a tightly controllable set-up[41]. CVD is mostly a life-time developing and worsening condition, whereas cell culture experiments are limited to days or weeks. Still, there have been applied a range of possibilities to mimic *in-vivo* pathogenic processes. OoC allow to study the impact of hemodynamic shear forces, the ECM composition or EC interaction with other cell types like pericytes/SMCs or

immune cells[38]. Treatment with reagents that induce oxidative stress or inflammation widen the range of experimental set-ups[42].

1.3 Adipose tissue in context with vascularization

1.3.1 Adipose tissue development and function

Endothelial vessels may not only be considered singularly as they are finally connected to and perfusing the respective organ and thus play an important role in organ function and homeostasis. The special interdependence of blood vessels and adipose tissue, an organ highly involved in metabolic syndrome, will be outlined in the following chapters.

Adipose tissue (AT) belongs to the connective tissues and is the main energy storage of the body. It also provides mechanic properties to serve as buffer for organs and skeleton. AT is a highly metabolically active organ which also contributes to hormone homeostasis and influences appetite sensing and digestion. There are different types of fat, whereof white fat (WAT) is the most abundant AT representative (**Figure 4**). WAT depots are called according to their location in the body either visceral or subcutaneous fat. Visceral WAT (VAT) lines the peritoneal cavity around organs. Subcutaneous WAT (SAT) is the most abundant fat mass (up to 80%) with high concentration in the gluteofemoral region[43,44].

The major cellular representative of WAT is the adipocyte which typically contains one large lipid droplet as energy storage (unilocular). In fasting state adipocytes degrade stored lipid content (triglycerides) and release fatty acids, a term called lipolysis, to fulfil the energy needs of other organs. The sympathetic nervous system-related ß-adrenergic pathway triggers adipocyte lipolysis, mainly via transmitter norepinephrine and epinephrine. The ß-adrenergic pathway is also activated during exercise or cold induction. Whereas in feeding state adipocytes take up energy-rich nutrients like glucose, amino acids, or free fatty acids (FFA) and metabolize and store them as fat, called lipogenesis. One aspect of sensing feeding state is that AT reacts to the pancreatic ß-islet-derived hormone insulin which is released in reaction to glucose excess in the blood. In reverse, AT influences insulin sensitivity of other organs by the secretion of hormones or paracrine signaling molecules, called adipokines[43,45].

Next to adipocytes, AT contains a variety of other cell types as adipose tissue-derived stem cells (ASC), adipocyte progenitors/pre-adipocytes (PA), fibroblasts, ECs, SMCs

and resident immune cells like macrophages (**Figure 4**). Due to their high lipid content adipocytes extracted from *in-vivo* tissue are floating and thus separated from other AT-derived cell types which are termed as stromal vascular fraction (SVF). In adult fat depots, adipogenesis, the process of differentiation of adipocytes from progenitor cells, happens for a lifetime as natural turnover of tissues. Human ASC (hASC) belong to the mesenchymal stem cells with multipotent differentiation capacity towards as for example the osteogenic, chondrogenic or adipogenic lineage. PAs have committed from hASC to further differentiate into adipocytes[44,46]. During early adipocyte differentiation, transcription factors from the CCAAT/enhancer-binding protein (C/EBP) family, C/EBPδ and C/EBPß induce the upregulation of the master regulator of adipocyte gene expression Peroxisome Proliferator-Activated Receptor γ (PPARγ) or C/EBPα. PPARγ and C/EBPα orchestrate the expression of mature adipocyte proteins during late differentiation stage. Mature adipocytes express lipid-droplet forming perilipin, adipocyte-specific hormones as leptin, adiponectin, lipolytic/lipogenic enzymes and fatty acid binding proteins (FABP)[43,47,48].

In contrast to the energy-storing character of white fat, brown and beige fat represent a dominantly burning alternative of AT through thermogenesis[43]. Brown fat (BAT) is represented in limited depots in human adults like at the clavicles or the pericarotid artery[49]. Beige fat is another form of thermogenic fat located in white fat depots. Beige adipocytes can form *de-novo* upon an external stimuli like cold. According to three different, yet to be confirmed hypotheses, beige adipocytes derive A) from perivascular progenitors cells in AT with αSMA or PDGFRα (platelet-derived growth factor receptor α) expression, B) from transdifferentiated white adipocytes or C) from dormant beige adipocytes[50]. Differently from white adipocytes, brown and beige adipocytes contain multiple lipid droplets (multilocular) and a high mitochondria content[43]. Cold activates the sympathetic nervous system and thus ß-adrenergic pathway mainly regulates thermogenic activity and gene programs in adipocytes[43]. Interestingly, ß-adrenergic induced lipolysis providing fuel for the thermogenesis also triggers browning gene expression[51].

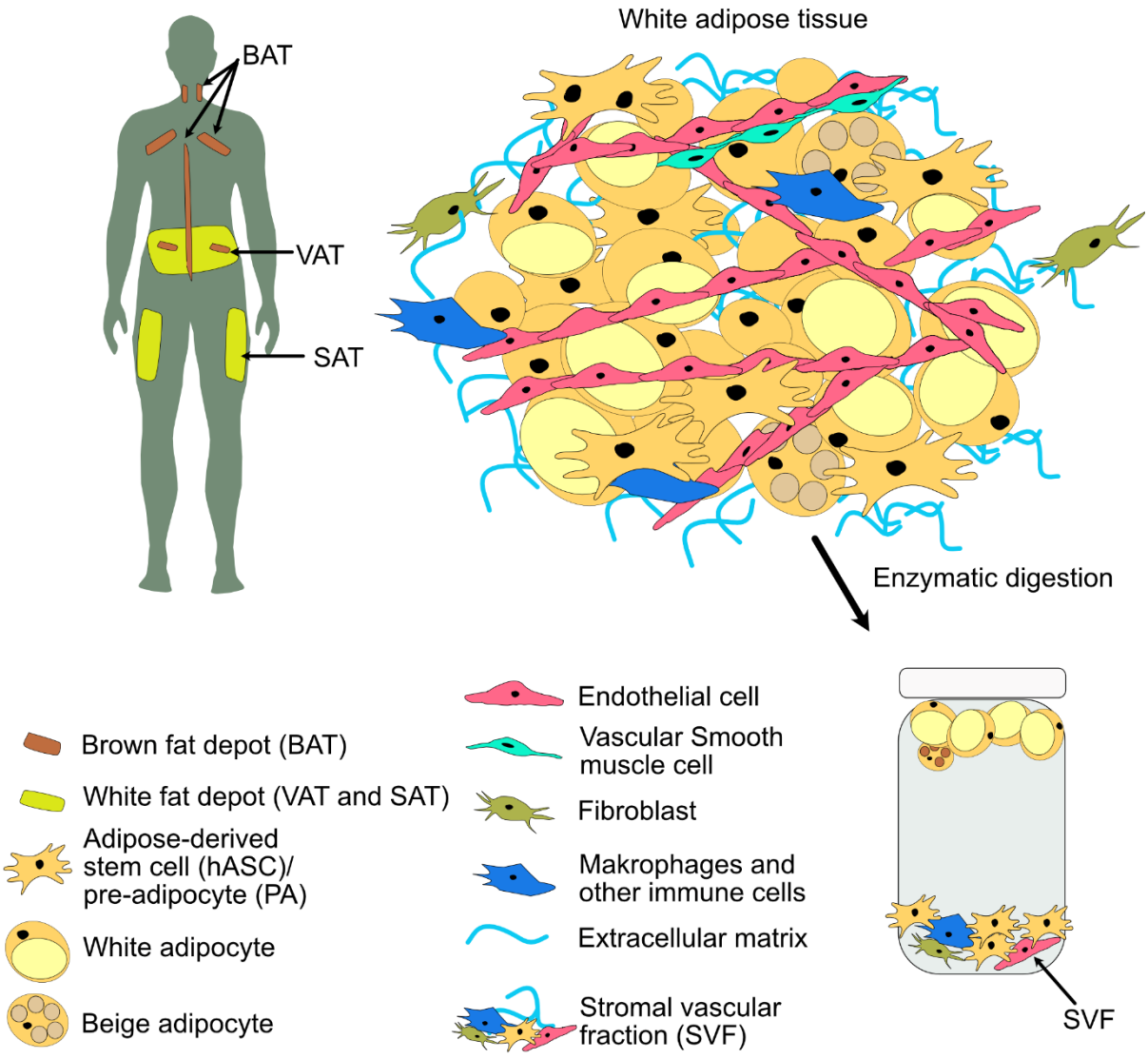

Figure 4 Overview of adipose tissue localization and composition

Residing brown fat depots (BAT) were found in adults in cervical, supraclavicular, paravertebral, periaortic, axillar and perirenal regions. White adipose tissue is abundant in visceral (VAT) and subcutaneous (SAT) fat depots. White fat is a connective tissue consisting of adipose-derived stem cells (hASC), pre-adipocytes (PA), beige and white adipocytes, fibroblast, immune cells as macrophages endothelial cells and vascular smooth muscle cells, embedded in a dense extracellular matrix. Through enzymatic digestion floating adipocytes can be separated from other adipose tissue cell types called stromal vascular fraction (SVF).

1.3.2 Endothelial blood vessels in adipose tissue

As any other organ, blood vessels are indispensable for AT sustenance with oxygen and nutrients and thus, AT is highly vascularized giving any adipocyte access to a vessel. Being in tight proximity, ECs and adipocytes interact functionally with each other exceeding simple nutrient and signal molecule exchange between tissue und

circulation. There is increasing evidence that adipocyte function should be inspected with regard to the surrounding vasculature which requires profound studies of EC-adipocyte crosstalk[52–54]. A well-studied interaction is the uptake and transport of fatty acids through the endothelium towards adipocytes[52]. Lipids as triglycerides are often transported through the blood bound in protein-lipid complexes, so called lipoproteins. Adipocytes express the enzyme lipoprotein lipase (LPL) that can hydrolyze fatty acids from the triglycerides stored in lipoproteins[52]. This process is facilitated by ECs which express an LPL-anchoring protein to locate adipocyte-derived LPL on the endothelium surface where it fulfils its role[52]. The released fatty acids are then transported through the endothelial layer by vesicle-mediated transport[52]. Apart from fatty acids, other molecules, like glucose or insulin also need to pass endothelial barrier towards adipocytes. Glucose is metabolized both in ECs and adipocytes and transported into the cell by glucose uptake transporters (GLUTs). In ECs dominates insulin-independent glucose uptake by GLUT1 whereas in adipocytes, glucose is internalized insulin-dependently by GLUT4, although ECs also express GLUT4[52]. Pathways how trans-endothelial fatty acid, glucose or insulin transport is regulated, remain to be fully understood[52]. Apart from trans-endothelial transportation, adipose vasculature is in increasing focus for impacting AT homeostasis through paracrine signaling[53,55]. A recent study has not only examined regulatory role of ECs in adipocyte lipid uptake but also the possible regulation of adipocyte function and maturation by secretion of PPARy ligands from microvascular endothelial cells of human AT[56]. Stringently, positive influence of ECs on adipocyte differentiation has been assumed for a long time[57,58].

During AT development, it is suggested that angiogenic network formation precedes adipogenic differentiation[59]. Interestingly, progenitor cells in the vascular niche potentially contribute to de-novo differentiated adipocytes although their actual role in *in-vivo* adipogenesis is controversially discussed[53]. From another point of perspective, not only AT is highly vascularized, but also large vessels are surrounded by conglomerations of fat called perivascular adipose tissue (PVAT). PVAT was characterized to be of brown or white AT type depending on the vessel location in the body. But all PVAT types have in common that they not only provide mechanical structure but interact with its corresponding vessel in an endocrine and paracrine manner. In health state, PVAT supports vessel function by secreting adipokines, chemokines and even vasoactive molecules, like NO[60].

1.3.3 Adipose tissue and vascularization in obesity and metabolic disease

In high correlation with metabolic syndrome, obesity is a major health concern worldwide. Mainly caused by a constant dietary calorie surplus and/or reduced energy expenditure through low corporal activity, the excess of energy rich nutrients is stored as fat in WAT. But also hormonal, genetic and epigenetic factors facilitate obesity[61]. It remains elusive why some obese individuals have a higher risk for T2DM and CVD (metabolically unhealthy obesity, MUHO) and others have less frequently accompanied complications, called metabolically healthy obesity (MHO)[62]. MUHO tend to have higher visceral obesity whereas increased subcutaneous fat distribution is a positive metabolic indicator in MHO[62]. Still, obese patients are generally at higher risk than lean individuals thus making weight-loss interventions medically sensible[62]. WAT expansion happens either through hyperplasia, an increase in adipocyte number by adipocyte differentiation or through hypertrophy, an increase in adipocyte size. Especially hypertrophic WAT expansion is accompanied by adipocyte death and inflammation leading to AT metabolic dysfunction. Hypertrophied adipocytes secrete chemokines recruiting immune cells, as monocytes, into AT and converting them to pro-inflammatory macrophages. But also fat tissue-residing immune cells convert into an activated state during obesity. Increased secretion of pro-inflammatory cytokines and adipokines produced in AT leads to a low-grade but chronic systemic inflammation. Chronic inflammation affects AT and other nutrient-metabolizing organs like the pancreas, liver or the muscle and is highly suggested to contribute to insulin resistance, a hallmark of T2DM. While WAT mass increases, BAT quantity but also BAT activity is decreased in individuals with obesity. As discussed earlier, BAT is an efficient metabolizer of excess blood glucose or fatty acids through thermogenesis and BAT loss and reduced activity may worsen insulin resistance and hyperlipidemia. Consequently, current obesity research focusses with high effort to increase BAT or beige fat activity[61–63].

WAT expansion also affects AT vascularization. Due to their increased size, oxygen supply to adipocytes is lowered through limited access to existing vessels. Hypoxia not only is a decisive trigger of adipocyte inflammation and death but increases the expression of hypoxia-inducible factors (HIFs) inducing angiogenesis in endothelial cells. Most prominently, activation of vascular endothelial growth factor and its

corresponding receptor pathway (VEGF/VEGFR) allows endothelial network expansion and perfusion of increasing WAT. Thus, research approaches try to interfere in VEGF signaling with the objective to limit obese WAT expansion and inflammation. Interestingly, intervention in VEGF pathway induced AT browning in several experimental set-ups bridging AT vascularization and browning in obesity intervention[54,64]. The initial understanding of the influence of adipose vasculature on adipocyte nutrient uptake, adipogenesis and metabolic homeostasis in health and obesity indicates the need for future studies to aid in the treatment of metabolic syndrome[53,55].

1.4 *In-vitro* modeling of human vascularized adipose tissue

Viewing the interdependence of adipocytes and ECs in health and obese state there is a high demand of *in-vitro* models of human vascularized adipose tissue[65–67]. Although mouse models provide various possibilities to induce and examine obesity in a whole body system, mice may not reflect human AT physiology fully and raise ethical concerns. Human *in-vitro* AT models allow for highly controllable and simplified set-up and parameters may be adjusted step-wise for specific questions (**Figure 5**). 2D models with conventional cultivation on a monolayer do not reflect the environment of connective AT tissue adequately, resulting in multilocular, small lipid droplets instead of unilocular adipocytes as *in-vivo*[68–70]. In contrast, 3D models provide the opportunity to embed adipocytes inside a physiologic structural matrix, optionally in co-culture with various cell types from the SVF[68]. Adipocytes, endothelial cells and ECM proteins can either be formed towards 3D vascularized AT by self-assembly as organoids or by bioprinting techniques[68]. Recently, AT models has been established on microfluidic chip platforms[71,72]. 3D cell cultures can also be constructed scaffold-free, for example in microwell formats or by the hanging drop method[68].

Adipogenesis and adipocyte maintenance are supported by the surrounding ECM and adipocytes highly contribute to matrix remodeling. Implementation of matrices in 3D models though increases *in-vivo* similarity[68]. Synthetic ECM material can be technically engineered to create certain mechanic properties[68,73]. Among the naive and physiologically more relevant ECM materials, collagens has been established for 3D modelling[68]. Especially collagen I is one of the most abundant ECM proteins in AT *in-vivo*[74]. Decellularized matrices extracted from in-vivo tissues where cells are removed

while maintaining ECM structure, were developed as a more complex variant of physiologic ECM[75].

Cellular components for 3D AT modelling can be extracted in efficient amount and ethically justifiable manner from patients fat depots through liposuction and thereafter enzymatic digestion of the tissue fragments[65,68]. Notably, both adipocyte/adipocyte progenitors and endothelial cells (HAMECs) could potentially be isolated and used for vascularized AT engineering from the identical patient. Donor-specific cell material with distinct metabolic and genetic background are interesting for studying disease related traits[76]. As mature adipocytes are difficult in handling through their fragility and floating behavior, SVF-derived hASC with adipogenic differentiation capability are favorable for 3D adipocyte culture[65,68]. hASC can be obtained cryo-preserved from biobanks and be expanded over several passages excelling high usability in cell culture experiments[65,68]. HiPSC-derived adipocyte (SC-adipocyte) models are not common until now, a vascularized adipose tissue model system based on hiPSC-derived thermogenic adipocytes combined with primary ECs was recently engineered[77]. Recent studies also implemented microvascular fragments from SVF to create vascularized AT[76,78]. These fragments offer the advantage that naive microvascular structures are still intact and they contain perivascular cells as well as adipocyte precursors. Conversely, the cell-mix may not allow defined cellular composition and interaction studies of specific cell types.

One of the most challenging aspects of vascularized AT engineering is to find a suitable media condition. Adipocyte differentiation medium (ADM) consists of a cocktail of adipogenic factors with strictly defined concentrations and the recipe usually changes over differentiation period. In contrast, endothelial network formation requires an endothelial cell growth medium (ECGM) containing growth factors that promote endothelial proliferation and maintenance. Different studies showed that both media have a negative impact on the respective other co-cultured cell type[78,79]. Therefore, both media types are partly contradicting each other and the media composition has to be evaluated carefully.

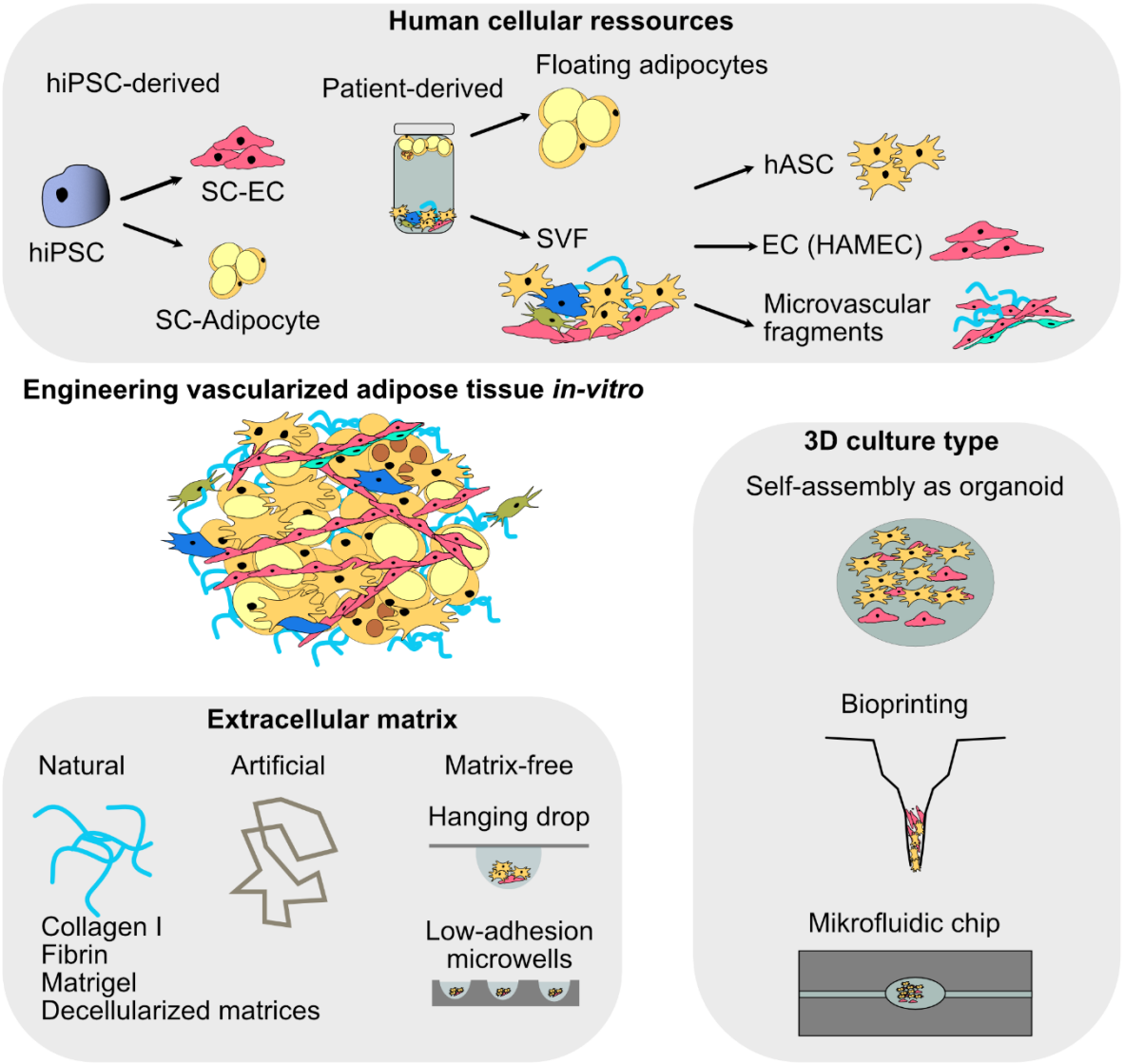

Figure 5 Engineering vascularized adipose tissue *in-vitro*

Human cellular resources can either be obtained from hiPSC that undergo differentiation towards adipocytes (SC-Adipocyte) or endothelial cells (SC-EC). The second option is cellular retrieval from human adipose tissue liposuction and enzymatic digestion to yield floating adipocytes and SVF. Outgoing from SVF, either hASC, adipose-derived EC (HAMEC) or natively structured microvascular fragments can be isolated. The cells can be embedded into artificially engineered matrix fibers, into naturally derived matrix components or cells are aggregated by matrix-free options. 3D tissue may be formed as organoids by self-assembly, by bioprinting or within microfluidic chip platforms.

1.5 State-of-the art methodical approaches for characterization of vascularized 3D tissue models

1.5.1 Single cell RNA sequencing for dissecting endothelial cell states

Within the last 10 years, next-generation sequencing approach has evolved towards platforms allowing fast and easy transcriptome (cellular RNA) sequencing on a single cell level, referred to as single cell RNA sequencing (scRNAseq), with user-friendly wet-lab and bioinformatic pipelines. ScRNAseq has the advantage over bulk sequencing approaches, that distinct cell type populations within a heterogeneous cell-mix, e.g. derived from a tissue, can be differentially regarded allowing deep analysis of each cell type.

ScRNAseq has helped to better understand the variety of endothelial cell types within the human body. These so called transcriptomic atlases explain how endothelial subtypes are adapted to specific vessel types (arterial, venous, lymphatic toning) but also in regards to organ-specific adaptions as for AT[80]. Concomitantly, also metabolic disease and obesity-related alterations in endothelial cells can be screened deeply with this technique[81]. Larger scientific cooperations, like the Tabula Sapiens consortium[82], aim to merge datasets from multiple single cell transcriptome organ atlases and enable to compare toning of endothelial cells between different organs. The amount of *in-vivo* scRNAseq datasets of human tissue is rapidly growing and thus could help interpreting how ECs undergo maturing effects in advanced *in-vitro* 3D cell culture models. ScRNAseq technology has already been successfully applied to endothelial-vessel-on-chip[83] applications to reveal transcriptomic changes in CVD models. To my knowledge, *in-vitro* vascularized AT organoid models have not been studied yet on single-cell RNA level but would be prone for deeper analysis of the co-developing cell types and their interactions.

A popular method for scRNAseq preparation of single cells is droplet-based. Each cell is partitioned into a water drop where a gel emulsion is added that contains a unique bar code per cell. This bar code labels mRNA (messenger RNA) molecules of the cell so that the genetic transcripts are distinguishable between each cell when they are pooled for sequencing downstream processes. After sequencing, the reads are mapped to the human reference genome and quality-filtered resulting in a cell-gene matrix. This matrix contains the information how many reads (mRNA molecules) per

gene each cell contained and can be further statistically analyzed for biologic questions. All these different parameters lead to high data dimensionality thus complicating a simplified two-dimensional graphical presentation. For this, data dimensionality is reduced by methods like UMAP[84] (Uniform Manifold Approximation and Projection) transforming variables into new, lower dimensional variables. As results, these new variables can be plotted on a graph but still contain information about the relationship between single data points from the high dimensionality data. Thus, UMAP can visualize the close relationship of single cells regarding a range of features (genes and counts) and represents those relationships as cell clusters[85,86]. Single cell transcriptomics also enables for techniques unveiling temporal dynamics of gene expression, called RNA velocity. For this, a new count matrix is generated containing information about the presence of unspliced, pre-mature mRNA or spliced, mature mRNA. In cells, the amount of unspliced and spliced mRNA reaches a steady state as newly transcribed unspliced mRNA is processed towards spliced mRNA which is followed by degradation of the mature mRNA. In case of induction or repression in gene expression the amount of unspliced mRNA changes and thus, the steady state is transiently deviated. These deviations are used to estimate future cell states of gene expression and are presented as vectors pointing gene expression changes between cells[87,88].

1.5.2 Secretome and transcriptome analysis by mass spectrometry

Liquid chromatography-tandem mass spectrometry (LC-MS/MS) is a powerful technique for identifying and quantifying proteins, metabolites or other molecules in a biologic sample. It finds its application not only in biologic research but also in clinical diagnostics or in pharmaceutical drug development. The technique benefits from the efficient separation of molecules by high performance liquid chromatography on the one hand and from the highly specific detection of substances by mass spectrometry. Being a fast technology with high-throughput made LC-MS/MS valuable for analyzing differences in intracellular (proteome) or secreted proteins (secretome) of biological cell samples.[89] Recent advances in protocol refinements allow for analysis of small sample volumes[90], which is crucial for analysis of *in-vitro* 3D cell culture systems with low amount of cells per sample. Thus, proteomic profiling of endothelial vessels-on-chip have already been performed successfully[91] and opens perspectives for further exploration of this technique for the analysis of advanced vascularized 3D models.

1.5.3 Targeted knockdown of genes of interest for deeper analysis

Mass-spectrometry and scRNAseq are potent tools to identify new candidates of genes/proteins expressed in cells that could be involved in pathogenic mechanisms. Stil, these techniques give an abstract picture of protein/gene expression. Depending on batch effects, statistical evaluation methods or also user-dependent biased interpretation different results may be achieved[86]. A reliable method to actually proof an impact of specific gene/protein expression of a target on cellular level is to change its gene and downstream protein expression by genetic modification.

Viruses have evolutionary developed a range of structures helping them to evade cellular barrier mechanism, to enter a cell and make use of the cellular gene/protein expression mechanism to produce virus specific proteins necessary for virus multiplication within its host body. Genetic engineering has made advantage of viral tools to modify cells for research but recently more and more emerging also for medical needs with application in patients called gene therapy[92,93]. When it comes to human cell culture systems one method to induce stable knockdown of mRNA is the transduction of target genes into cells by the help of modified lentiviral vectors. The objective here is to first engineer virus particles containing all modules to enter a cell and integrate the target gene into the host genome without containing the specific pathologic components. For knockdown strategy, the transduced target gene impairs cellular translation of the target mRNA in the cell, so called RNA interference. In this case, the transferred gene codes for a small hairpin RNA (shRNA) which degrades the target mRNA post-transcriptionally leading to reduced translation of the mRNA into its protein. Lentiviral vectors are advantageous for stem-cell applications as they stably integrate into the genome of dividing cells[93,94]. For targeted studying of endothelial signaling pathways, the engineered knockdown cell line is implemented into the established biological model. Impairments of functional or morphological parameters can then trace back directly to the genetic knockdown and prove a function of the target protein/gene.

2 Aim of the thesis

Metabolic alterations like T2DM, obesity and CVD are one of the major health concerns post-industrial societies are facing in the presence[16]. In order to understand these conditions, the endothelial vessel system came into focus either being directly affected by metabolic alterations as seen in atherosclerosis or impacting function of other organs as during the hypertrophic growth of AT in the course of obesity[95].

The primary aim of this thesis is to advance the understanding of vascular and metabolic interactions under both physiological and pathological conditions applying human stem cell-based *in-vitro* models. Utilizing insights and methodologies from recent studies, this research seeks to:

I) Develop and characterize advanced vascularized *in-vitro* models:

Vessel-on-chip to engineer a scalable and open microfluidic platform which enables the cultivation of stem cell-derived endothelial cells (SC-ECs) in luminal shape within a physiological hydrogel matrix. These platforms are designed to simulate vascular conditions, maturing SC-ECs upon shear stress, enabling the modeling of critical endothelial functions such as barrier formation, sprouting or nitric oxide synthesis.

Vascularized adipose organoids (vAOs) to co-culture SC-ECs with human adipose-derived stem cells (hASCs) within a 3D hydrogel matrix, establishing a system that supports simultaneous angiogenesis and adipogenesis. The vAOs aim to mimic native AT microenvironments, allowing for the functional study of adipocyte-endothelial interactions and their impact on metabolic pathways.

II) Apply advanced vascularized *in-vitro* models to investigate the cellular and molecular mechanisms underlying vascular and metabolic health:

Single-cell transcriptomics are aimed at exploring cellular heterogeneity, revealing specific endothelial and stromal cell subtypes and their roles in tissue function and dysfunction. For instance, the maturation of SC-ECs under shear stress conditions or their interaction with adipocytes in vAOs can elucidate key pathways governing vascular stability and metabolic activity.

III) Model disease-specific conditions for therapeutic insights:

Vascular disease onset, such as atherosclerosis, is pursued to be simulated by applying oxidative stress to vessels-on-chip and observing proteome and secretome changes in response to stimuli like oxidized LDL (oxLDL) and free fatty acids (FFAs).

vAOs are used to examine the impact of endothelial dysfunction on adipose tissue metabolism, especially under conditions simulating obesity and type 2 diabetes. In particular, dissection of signaling pathways critical for vascular and adipose tissue development, such as PDGFB signaling in endothelial-pericyte interactions is targeted. Endothelial-specific knockdown studies can provide insights into how endothelial tone and perivascular alignment contribute to metabolic processes in AT like lipolysis and glucose uptake in health and disease.

By achieving these aims, this thesis pursues to bridge critical gaps in understanding human vascular and metabolic interactions, offering novel platforms for exploring therapeutic strategies against vascular and metabolic diseases. Tailoring these models for patient-specific investigations, enable the study of genetic and epigenetic factors influencing vascular and adipose tissue health. Further, the need for integrated approaches promise to refine animal-free research methodologies while advancing personalized medicine.

The scientific results presented In thesis are structured as follows: Chapter 3 presents the engineering and design of the vessel-on-chip. The generated endothelial lumen were characterized on functional level as well as on single cell transcriptome level when set under dynamic flow in comparison to static conditions. Next, the endothelial model system was challenged by oxidative stress to mimic the on-set of atherosclerotic disease and alterations in cellular secretomic and proteomic changes were analyzed. Chapter 4 focuses on the engineering of a 3D vascularized AT model. vAO were first characterized for morphologic parameters as for vessel formation and adipogenesis as well as for adipocyte function. Exploiting sc/snRNA-seq technique, transcriptomic adaptions and possible cell-cell interactions were investigated in the co-developing adipocyte progenitor and endothelial cell populations of vAOs in comparison to non-vascularized/non-adipogenesis controls. An endothelial knockdown model was applied to study if disturbed vessel function impacted adipocyte functionality in vAO and thus underlines adipocyte-endothelial interdependence in AT.

3 Stem cell-derived vessels-on-chip for cardiovascular disease modelling

This chapter is cited from the publication: Marder, M.*, Remmert, C.*, Perschel, J. A., Otgonbayar, M., von Toerne, C., Hauck, S., Bushe, J., Feuchtinger, A., Sheikh, B., Moussus, M. and Meier, M. (2024). Stem Cell-Derived Vessels-on-Chip for Cardiovascular Disease Modeling. Cell Reports. Volume 43, Issue 4, 23 April 2024, 114008.

The human vascular system is a highly organized and dynamic cellular network responsible for maintaining homeostasis in all organs. Endothelial cells (EC) are the central cell type of the vascular system, which forms the inner wall layer of the blood and lymphatic vessels and thus regulates blood flow, immune cell trafficking, oxygen, and nutrient delivery[96]. To comply with the multiple functions in the different organs ECs are highly plastic and heterogeneous. Single-cell transcriptomics has confirmed the trans- and intra-tissue EC heterogeneity[97], but how the heterogeneity evolves and which microenvironmental factors shape EC states remain unclear. Understanding EC development, adaptation, and response to microenvironmental cues is of central importance for revealing dysfunctions in the vascular network, for example, in chronic metabolic syndromes such as obesity, diabetes, and aging[17].

Reliable human *in vitro* models for endothelial tissues and the vasculature are in urgent demand, given the complexity of the human vascular system and proven metabolic distance of rodent *in vivo* models to the human biology[98]. Cardio-vascular damage is an intrinsically slow process, particularly when caused by metabolic syndromes[95]. Engineered, stable cell types that carry genetic predispositions to vascular diseases are hence best suited to recapitulate human vessels *in vitro*. Human inducible pluripotent stem cells (hiPSCs) present an almost unlimited EC source with highly reproducible phenotypes[29]. Various differentiation protocols have been developed to engineer stem cell-derived ECs

(SC-EC).[27] Upon culturing SC-EC in a hydrogel environment, tubular microvessel structures were formed, and single-cell transcriptomic analysis resolved transcriptional changes during their formation, including sprouting, coalescence, and tubulogenic cell states[1]. However, SC-ECs within microvessels exhibited only immature and nonspecialized characters[99–101]. While mechanical properties of SC-ECs within

organoid and hydrogel cultures can be modulated, the shear flow cannot due to missing accessibility of the microvessel luminal site. Shear flow regulates, however various EC functions, such as proliferation and differentiation, through transcriptomic changes[7,102].

Attempts to expose ECs to flow shear forces have been limited to microfluidic cell culture systems in which ECs are either cultured on two-dimensional (2D) surfaces of a microchannel[103], allowed to self-assemble into microvasculature in hydrogel chambers[104], or formed upon assembly onto hydrogel-patterned microchannel walls[105]. The latter organotypic vessel-on-chip systems have the advantage of being reproducible and robust because microchannel geometry determines the form factor of the vessel size. Like all miniaturized organ-on-chip systems, relatively low cell-material challenges downstream analytics, whereas larger biochip footprints interfere with standard parallelization and automation. Vessel-on-chip approaches have, to date, mainly used primary or immortalized ECs[106]. Functionally, on-chip vascular disease models have been used to recapitulate the onset of atherosclerosis development, a process that involves the accumulation of lipids, mainly cholesterol-containing low-density lipoproteins (LDL), in arterial ECs. The subsequent generation of reactive oxygen species (ROS) leads to the formation of vessel lesions, EC dysfunction, impaired vasodilation through reduced nitric oxide (NO) synthesis, flow disturbances, and local inflammation[19].

We here report the development of a human stem cell-based blood vessel-on-chip model. The open design of the 3D-printed microfluidic chip platform enables multiomics downstream cell analysis with a low sample volume and cell number. Gravity-driven flow on-chip induced barrier function, sprouting, and arterial toning of SC-ECs as shown by single-cell transcriptomics and high-resolution imaging. Upon individual stimulation of SC-ECs with oxidized Low-density Lipoprotein (oxLDL) and free fatty acids (FFA), early-onset of atherosclerosis hallmarks were monitored. Proteomic and secretome changes in the vessel-on-chip system due to oxLDL or FFA stimulation under flow revealed distinctive ROS and NO synthesis responses. Taken together, we provide a fully integrated stem cell-based vessel model for multiomics cell analyses that can readily integrate with epithelial tissues of distinct origins.

3.1 Material and methods

3.1.1 Materials availability

This study did not generate new unique reagents.

3.1.2 Data and code availability

The code for scRNA-seq analysis has been deposited on GitHub (https://github.com/MeierLabMiBioEng/StemCell-derivedVessel-on-chip) and is publicly available. Raw data and processed data are publicly available on the Gene Expression Omnibus repository under accession code GSE253320. Any additional information required to reanalyze the data reported in this paper is available from the corresponding author upon request.

3.1.3 Experimental model and study participant details

Experiments were conducted using a hiPSC line, which was kindly provided by Prof. Lickert (Helmholtz Zentrum Munich) and is registered in the human pluripotent stem cell registry (https://hpscreg.eu) under the name HMGUi002-A. The cell line was derived from a Caucasian male donor.

3.1.4 Generation and cultivation of SC-ECs

Human iPSCs were cultured on hESC Matrigel-precoated 6-plates according to manufacturer's recommendations (Corning, Cat#354277) in mTeSR1 medium (StemCell Technologies, Cat#85850) at 5% CO2, 5% O2 and 37°C with daily medium change and passaged twice a week in a 1:6 ratio using 0.05% Trypsin-EDTA (Sigma Aldrich, Cat#T4174). The hiPSC culture was free of mycoplasma contamination as tested by the MycoSensor PCR assay kit (Agilent Technology, Cat#302109).

For the differentiation, the hiPSCs were transferred into a 3D cell culture format. Therefore, the medium was aspirated, cells were washed with 2 mL PBS -/-, and 500 µL Accutase (Sigma Aldrich, Cat#A6964) was added. During incubation at 37 °C for 5 minutes, cells detached. Addition of 2.5 mL mTeSR stopped the Accutase reaction. The well was washed with 1 mL mTeSR before centrifugation for 5 minutes at 200 x g and resuspended in 500 µL mTeSR with Rock inhibitor Y-27632 dihydrochloride 10µM (Abcam, Cat# HY-10583) and 1% Penicillin/Streptomycin (P/S) (Thermo Fisher Scientific, Cat#15140122). Cells were transferred in 6-well ultra-low attachment plates (Corning, Cat#3471) at a cell concentration of $5*10^5$ cells/ml and in

3 ml volume. The plate was placed on an orbital shaker in the cell incubator and rotated at a frequency of 100rpm.

The differentiation protocol was adopted from Rosowski et al.[6]. From day zero to day three of differentiation Neurobasal Medium with B27 supplement (Life Technologies, Cat# 21103049 and 12587010) supplemented with BMP4 (25 ng/mL) (PeproTech, Cat#120-05ET-10) and CHIR 99021 (7.5 µM) (Axon Medchem BV, Cat# 1385) was used without media change. Media was changed daily from day three to seven of differentiation using StemPro-34 (Life Technologies, Cat#10639011) with VEGFA (200 ng/mL) (PeproTech, Cat#10-20-100) and forskolin (2 µM) (Abcam, Cat#ab120058). Afterward, StemPro-34 with VEGFA (30 ng/mL) and FGF2 (30 ng/mL) (Miltenyi Biotech, Cat#130-093-838) was used with exchange after two days until use.

Successful differentiation was determined by flow cytometry analysis and staining for the EC marker CD31-FITC (BD, Cat#555445) and the smooth muscle cell marker CD140b-PE (BD, Cat#558821). For purification, SC-ECs were FACS sorted (MACSTyto Cell Sorter, Miltenyi Biotec, according to manufactures protocol) leading to a SC-EC population of >90%. Standard SC-EC culture was performed on fibronectin coated plates (Sigma, 5 µg/ml final concentration) in StemPro-34 medium supplemented with 15% FBS (Sigma, Cat#F7524), 100 ng/ml VEGFA and 100 ng/ml FGF2. Medium change was done every other day.

3.1.5 Cryopreservation and passaging of SC-ECs

SC-ECs could be passaged and were used until passage 6. For passaging, cells were washed with PBS-/- and detached with Accutase. The reaction was stopped with StemPro-34 medium followed by a centrifugation at 200g and 5 min. SC-ECs were resuspended in supplemented StemPro-34 medium and seeded in a 1:2 ratio in T75 flasks. For cryopreservation, detached SC-ECs were resuspended in FBS with 10% DMSO.

3.1.6 Chip manufacturing

For the OoC production, chips were printed using an Asiga Pico 2 HD UV 3D printer and Pro3dure GR-10 resin (clear, transparent, Litholabs, HX10031). Slice thickness was set to 50 µm. As described before, the anti-aliasing method[107] was used to compensate for errors in the 3D printed part by smoothening the chips channels to a round shape. After printing, channels were flushed with Isopropanol and chips were

washed and ultrasonicated for 15 min in Isopropanol. After removing all uncured resin, chips were dried at 80°C for 30 mins and UV-flashed in an N_2 atmosphere with 2000 flashes on each side using an Otoflash G171. For biocompatibility treatment, chips were incubated in 99% EtOH for 24 h and transferred to MilliQ water for 24 h. For the chip assembly, polyamide monofilaments (1005215; efco creative GmbH, Germany) were cut with a sharp scalpel and fed through the medium reservoirs and the gel chamber. The chip was bonded to a glass slide with a double-sided adhesive foil (ARcare 90445Q). To seal the chip, polydimethylsiloxan (PDMS) was into the outer chambers and cured for 15 min at 80°C. For sterilization, the chips were placed for 30 min under UV light prior to hydrogel filling.

3.1.7 Flow characterization

Microchannels were created in the OoC with a polypropylene filament of diameter 50 µm (CP05341A; SERAG-WIESSNER GmbH) and polyamide filament of diameter 150 µm and 250 µm (1005215, 1005225; efco creative GmbH). 80 µL PBS were placed on top of the gels. 100 µL PBS with 0.1% 2.55 µm polystyrene particles (PS-F-B237-1; microParticles GmbH) were added to both sides of the chip. Chips were placed on a Zeiss AxioObserver at angles of 7°, 13°, and 25° to induce gravity-driven flow. Particle flow rates were recorded with a frame rate of 700 fps and exposure time of 1/20000 s for 5 seconds at 5, 30, 60, 120, 180 and 240 seconds after tilting. Buffer was allowed to level out on both sides before subsequent recordings. For cyclic measurements, chips were rotated every 2 minutes and particles were recorded 5, 30, 60 and 120 seconds after the start of every cycle. Recorded videos were analyzed in Fiji (ImageJ[108]) using the TrackMate[109] plugin (v6.0.1) and flow rate measurements were exported to R (v4.2.0) for further analysis. Wall shear stress values (τ_w) were calculated using a derivation of the Hagen-Poiseuille equation, where μ is the dynamic viscosity of serum-free media (0.73 mPa.s; Poon et al., 2020), U is the mean flow velocity and R is the radius of the lumen.

$$\tau_w = \frac{4\mu U}{R}$$

3.1.8 Cell seeding on chip

For cell seeding on chip, a collagen type I hydrogel (Corning REF: 354236) was neutralized for pH=7.0 with the appropriate proportions of 10xPBS,1 mM NaOH and H20 to obtain 2.5 mg ml^{-1}, mixed thoroughly and placed for 1 h on ice. Meanwhile,

sterile chips were cooled down to -20°C. The collagen gel was filled into the gel chamber (40 µl/chamber) and polymerized for 40 min at 37°C. SC-ECs were detached with Accutase and concentrated to 4x 10^6 cells per ml for seeding. Cells were resuspended thoroughly and 30 µl were added to the inlet and outlet chambers. The filament was pulled out of the outlet chamber using forceps to introduce gravitation-driven flow of cell suspension into the generated lumen. Chips were placed on a rocking shaker (OrganoFlow L, Mimetas) at a 10° angle and 6 rpm for 15 min. After initial seeding, EGM-2 (Sigma Aldrich, C-22011) medium was added to all chambers (30 µl/chamber). Chips for the flow condition were placed back on the shaker at a 25° angle and 2 min intervals. Complete medium change was performed after 2 h and then every day (70 µl/chamber). The open microfluidic system allows for high throughput handling as the medium change takes less than 1 min per chip using a multistep pipette and using a cell culture pump for aspiration through a filter-less 10 µl tip.

3.1.9 Whole mount immunofluorescence staining

For whole mount staining on chip, cells were fixed with 4% PFA for 15 min at RT and washed with PBS afterwards. Samples were permeabilized with PBS + 0.1% Triton X-100 for 30 min at RT, washed with PBS-T and blocked for 2 h with blocking buffer (PBS-T, 10% FBS, 1% BSA, 0.1M glycine, 3% donkey serum). Chips were stained in blocking buffer without glycine for 2 days at 4°C. Primary antibodies were washed out thoroughly with PBS-T for 1 h before secondary antibodies were added in blocking buffer without glycine. Secondary antibodies were incubated overnight at 4°C. Next, samples were washed with PBS-T and mounted in Vectashield for imaging.

3.1.10 Histology of lumen sections

Cell-laden lumina could be retrieved from the chip body by breaking the connecting structures of the insert with a scalpel. The hydrogel block was transferred to a well plate with tweezers, washed with PBS and fixed with 4% PFA. Paraffin embedding was initiated the same day according to standard procedures. 3 µm thick sections were stained with primary antibodies. Nuclei were identified with Hoechst 33342. Fluorescence stainings were digitalized with an AxioImager 7 (Zeiss, Oberkochen, Germany) equipped with a 20x objective, and visualized with the Zeiss Zen Blue Software.

3.1.11 Confocal imaging

Wholemount stained lumens were imaged on a confocal microscope (Zeiss Axio Observer LSM 880, Zeiss Zen black software). Images of VE-Cadherin, DAPI staining and brightfield PMT of the whole lumen including outgrowing branches were taken (20x magnification, 0,26 µm per pixel, 10 µm z-stacks). For visualization of COL1 fibers, blank lumens were prepared, fixed and imaged profiting from label-free imaging via confocal reflection microscopy.

3.1.12 Lumen permeability analysis

To test the lumens for endothelial barrier function, the lumens were perfused with 50 µl FITC-Dextran (diluted 1:10 in PBS, 2000 and 40 kDa, Sigma Aldrich, FD2000S) in the inlet chamber. Images were taken every 3 min for 20 min with an epi-fluorescent microscope (Zeiss Axio Observer Z1) using an automated imaging template for the chip designed with the Zeiss Zen Blue software. For analysis, 3 lines transverse to the lumen were set through each captured image in distance of 50 µm (**Figure 2E**). Those lines were measured for signal intensity from left to right. Next, the signal intensities from left to right were plotted in a Jupyter notebook script. To consider for the lumen not being exactly centered in the middle of the image, the maximum of each curve was set as x=0. Then, all FITC-dextran intensities of all lumens from one condition could be mean-plotted into one curve.

3.1.13 Branching characterization and branch density analysis

For branch analysis, Z-stacks from VE-Cadherin-stained confocal images defined as “only covering lumen bottom” were converged to a 3D-projection in Fiji. 3D-stacked images were batch-filtered in Fiji (i.e. CLAHE, Otsudark auto-threshold, median filter, binarized). For branching characterization, Fiji’s “skeletonize 2D/3D” and “Analyze skeleton 2D/3D” tools were applied on filtered and binarized images (**Figure S2B**). For density analysis, filtered and binarized images were measured for signal density (as a percentage of black over white signal) using a MATLAB script. Signal intensities of longitudinal lines were measured which were directing with 1 µm from each other from the central lumen towards the periphery branches. For each parallel line a mean signal intensity was measured, and those mean intensities could then be plotted in dependence from their distance from the central lumen resulting in the signal density

plot. The output data of skeleton and density analysis were further processed in Python.

3.1.14 Live dead cell analysis

ECs cultivated under flow were stained on day 2 with Live/Dead Viability/Toxicity Kit (LIFE Technologies - L3224) as described in the manufacturer's protocol. Stained lumens were imaged on an epifluorescence microscope (Zeiss, Zen software). For image analysis, signal intensities were normalized to an auto-threshold and a StarDist segmentation FIJI plug-in[110] was applied to detect live and dead cells. The mean signal threshold for both markers were set to 3000 and the mean area threshold to 50 µm².

3.1.15 NO assay

For measuring the NO production in ECs, the fluorometric Nitric Oxide Assay Kit (Sigma) was used according to the manufacture protocol. The assay is based on the enzymatic conversion of nitrate to nitrite so that the total amount of nitric oxide in the supernatant can be analyzed. For each condition a respective background control was carried along and background fluorescence was substracted after measurement. For normalization, cells were extracted from the lumen and counted.

3.1.16 Sample preparation for scRNA-seq

For RNA single cell sequencing, chips were washed with PBS. To ensure that only cells growing in the hydrogel were collected, inlet and outlet ports were blocked with 3% agarose. After solidification of the agarose, cells were treated with a 1:1 mix of Collagenase P (18 U final concentration, Roche 11213857001) and Accutase and incubated for 30 min at 37°C. Pipette tips and tubes were washed with PBS + 2% BSA before usage to reduce cell loss. Successfully dissolved hydrogels and a single cell suspension was confirmed under the microscope before harvesting the cells in PBS + 10% FBS. The cells were centrifuged at 300 x g for 3 min, washed with PBS + 2% BSA and filtered with a 20 µm cell Pluristrainer (pluriSelect, 43-50020-023). Cells were counted with TrypanBlue (Sigma) and a cell vitality of over 70% was confirmed. RNA libraries were generated using Chromium Single Cell 3' library and gel bead kit v3.1 (10x Genomics). The amplified cDNA library was sequenced on a NovaSeq SP flow cell from Illumina.

3.1.17 Pre-processing of scRNA-seq data

Raw sequencing data files were demultiplexed, aligned (reference genome hg38_ensrel96), filtered, barcodes and UMIs counted, and subjected to a quality filter with CellRanger (10xGenomics). The pre-processing and downstream analysis were performed with the package 'Scanpy[111] API'88 in python with default parameters, if not stated differently. Cell-ranger processed data from static and flow condition were first concatenated. Next, dead or stressed cells, identified by a percentage of mitochondrial genes higher than 15%, were filtered out. Cells with less than 3000 or more than $6x10^4$ total counts or cells with less than 200 expressed genes were excluded. Also, genes expressed in less than 10 cells were rejected. Afterwards, gene counts were normalized to 10^4 per cell and log transformed. Additionally, cell cycle genes and mitochondrial genes were regressed out. Doublets were detected with the Scrublet package[112].

3.1.18 Clustering and cell type annotation

The single-cell neighborhoods were calculated with the first 30 principal components and 10 nearest neighbors and the cells were clustered with the Leiden algorithm[113] at a resolution of 0.5. For visualization, UMAP was used to reduce the dimensionality of the data. Cell types were annotated by ranking the top 25 marker genes of each of the 7 Leiden sub-cluster based on literature research. Correlation plots confirmed similarity of subclusters. Cell type proportions and gene expression analysis were performed based on the defined categorical clusters.

3.1.19 RNA velocity using basic modelling

To investigate developmental trajectories in the flow sample, we analyzed the RNA velocity by recovering directed dynamic gene information through splicing kinetics in basic mode following the scVelo[87] standard pipeline. Variables and observations, like cluster annotation and UMAP coordinates were accessed from the Scanpy analysis as described above. The splicing matrix was generated by default settings of the velocyto[88] pipeline. After concatenating splice matrix and scanpy information, splice variants and cells were filtered, normalized, and logarithmized with the function scv.pp.filter_and_normalize (shared_counts=20, n_top_genes=2000). In the next step, the moments, based on the connectivity, were calculated with 30 PCAs and 30

neighbors. Then, velocities and the based root cell were assessed by the sc.velo algorithm and represented in an UMAP embedding stream projection.

3.1.20 Cell treatment for oxidative stress induction

ECs were seeded and cultured under flow for 1 day as described above. For oxidative stress induction, either 50 µg ml^{-1} oxLDL (life technologies) or 800 µM FFA-BSA mixture was added to EGM2 medium from day 1 to day 2. A FFA stock was prepared in advance consisting of a mixture of different fatty acids dissolved in ethanol: c14:0 (1.05%), c16:0 (26.75%), c18:0 (8.04%), c18:2 (36.63%), c18:1 (21.09%) and c20:4 (6.44%; all from Sigma) as described in Bondareva, et al. [81]. These candidates are a selection of the most common free fatty acids in human serum and the chosen percentual combination was measured in human serum[114]. For FFA-BSA treatment solution, an 8 mM stock solution was generated by conjugating the fatty acids to fatty acid-free BSA (Sigma). Therefore, a mixture of BSA, FFA and high-grade Ethanol (9: 0.8: 0.2) was incubated for 2h at 37°C and 1500 rpm. When described, sortilin inhibitor TY52156 was added in a concentration of 100 nM from day 1 on together with oxidative stress induction. On day 2, the EGM2 was replaced by serum free medium (DMEM/F12 + Glutamax +1% P/S) and the treatment was continued until day 3. On day 3, supernatants were collected for secretome analysis and immediately frozen and stored at -80°C. Afterwards the chips were washed four times for 1h with PBS before hydrogels were digested in a 1:1 mix of Collagenase P and Accutase. Cells were collected, washed three times with PBS and pelleted. Lysates were stored at -80°C until mass spectrometry preparation. Medium and untreated cell samples were carried along as controls. As the FFA treated sample contained BSA, the control was treated with a BSA-Ethanol-vehicle control.

3.1.21 Sample preparation and mass spectrometry measurements

Lysate pellets were prepared for mass spectrometry measurement as described in Compera et al.[72]. Supernatants were digested enzymatically using the PreOmics' iST Kit (Preomics GmbH, Martinsried, Germany) including the SP3 add-on kit according to manufacturers' specifications with adjustment of volumes for the SP3-lyse and -binding buffers to fulfill 1x concentration of buffers. After drying, the peptides were resuspended in 2% acetonitrile (ACN) and 0.5% trifluoroacetic acid. The HRM Calibration Kit (Biognosys, Schlieren, Switzerland) was added to all samples according to the

manufacturer's instructions. MS data were acquired on a Q Exactive (QE) high field (HF) mass spectrometer (Thermo Fisher Scientific Inc.) as described in Hladik et al[115].

3.1.22 Data processing - protein identification

Proteome Discoverer 2.5 software (Thermo Fisher Scientific; version 2.5.0.400) was used for peptide and protein identification via a database search (Sequest HT search engine) against Swissprot human data base (Release 2020_02, 20432 sequences), considering full tryptic specificity, allowing for one missed tryptic cleavage sites, precursor mass tolerance 10 ppm, fragment mass tolerance 0.02 Da. Carbamidomethylation of Cys was set as a static modification. Dynamic modifications included deamidation of Asn, Gln, oxidation of Met; and a combination of Met loss with acetylation on protein N-terminus. Percolator was used for validating peptide spectrum matches and peptides, accepting only the top-scoring hit for each spectrum, and satisfying the cutoff values for FDR <1%, and posterior error probability <0.05. The Sequest HT Xcorr filter was set to 1.6 removing identifications below this threshold. The final list of proteins complied with the strict parsimony principle.

3.1.23 Data processing - label-free quantification

Proteins were quantified based on abundance values for unique peptides. Abundance values were first normalized to the total amount of peptides in each sample to account for sample loading errors. The protein abundances were calculated summing up the abundance values for admissible peptides. The final protein ratio between experimental groups was calculated using median values of single peptide ratios per comparison. The statistical significance of the ratio change was ascertained employing the t-test method described in Navarro et al[116]. Adjusted p-values are calculated according to Benjamini-Hochberg[117].

3.1.24 Data analysis

In the following downstream analysis, only proteins with more than one unique peptide hit were used. Differential protein expression (DEP) analysis was performed with customized Python (version 3.10) scripts using the adjusted p-values (p.adj < 0.05) and normalized abundance ratios (ratio > 1.5). Differently expressed proteins were only taken into account, when abundances were measured in at least 75% of the replicates within each group. In addition, the secretome data was filtered for actively secreted proteins matching the DEP against the refined human secretome[118]. Only proteins with

the labels “blood secretion” were used. Enrichment analysis and Go term identification was performed using the STRING gprofiler[119] and Enrichr[120] databases and customized Python scripts from GitHub repository DbitX (https://github.com/jwrth/xDBiT_toolbox).

3.1.25 Oxidative stress compound staining

For staining of FFA accumulation, lumens were fixed on day 3 as described above, washed with PBS and incubated with BODIPY (4,4-difluoro-1,3,5,7,8- pentamethyl-4-bora-3a, 4a-diaza-s-indacene, Thermo, D3922) in a final concentration of 10 µg ml^{-1} in PBS, together with DAPI (Thermo, D9542, 1:100) and Phalloidin-Atto-647(ab176759, 1:200). For staining of oxLDL accumulation, lumens were treated as described for the oxLDL treatment with DiI-labelled oxLDL (Thermo, L34358) for 3 days. After fixation, lumens were stained with DAPI and Phalloidin-Atto-647 as described above. For detection of oxidative stress in cells, lumens were stained with greenfluorescent CellROX (Sigma, C10444). Lumens were washed 3 times in PBS, before CellROX was added in a final concentration of 5 µM in PBS together with Hoechst33342 (Thermo, 10 µg ml^{-1}) and incubated for 1h at 37°C in an incubator. After staining has been completed, lumens were fixed as described above and imaged with a confocal microscope under the same settings for all conditions. For a positive control, lumens were treated with 100 µM TBHP (abcam, ab113851). For image analysis of CellROX signal, for each capture a z-stack consisting of 6 slices with distance of 6 µm was converted to one stack image by 3D projection in fiji. Then, Stardist segmentation program was applied comparable to the live-dead staining. The mean signal intensity was set to 5 and the mean area threshold were set to 5 $µm^2$ for both the DAPI and CellROX channel. For later analysis in a Python script, fragmented, apoptotic and highly bright nuclei were further filtered, setting an area threshold of 60 $µm^2$. Due to technical-related differences in DAPI and CellROX staining intensities, for each image the CellROX signal intensity was normalized to its corresponding DAPI signal intensity, resulting in a normalized CellROX/DAPI intensity ratio for each image.

3.1.26 Quantification and statistical analysis

Statistical analysis was performed using the scipy.stats function with custom-written python code. Statistical details of experiments and numbers of replicates can be found in the figure legends. Data was tested for normal distribution with the Shapiro test and for homogenous variances with the Levene or Bartlett test. Statistical significance

between groups was tested with a pairwise t-test for two conditions and with a one-way ANOVA for multiple sample groups followed by a Tukeys post-hoc test.

3.2 Results

This chapter is cited from the publication: Marder, M.*, Remmert, C.*, Perschel, J. A., Otgonbayar, M., von Toerne, C., Hauck, S., Bushe, J., Feuchtinger, A., Sheikh, B., Moussus, M. and Meier, M. (2024). Stem Cell-Derived Vessels-on-Chip for Cardiovascular Disease Modeling. Cell Reports. Volume 43, Issue 4, 23 April 2024, 114008.

3.2.1 Design and characterization of the open organ-on-chip platform

The main body of the open organ-on-chip (OoC) platform was produced using 3D stereolithography printing and bonded to an adhesive foil on a glass substrate (**Figure 6A**). Each chip exhibited 6 arrayed unit cells, where each unit cell contained a hydrogel chamber and two fluid reservoirs, each holding an adjustable volume between 30–150 µL. Relevant chip dimensions are shown in **Figure S1A.** The gel chamber was connected to the fluid reservoirs using short microfluidic channels with a diameter of 350 µm on each side. Through the connecting channel, a nylon filament with a diameter between 50 and 250 µm can be introduced. The hydrogel chamber was filled with hydrogel prepolymers to encapsulate the nylon filaments. Upon removing the nylon filament through one of the fluid reservoirs, the hydrogel was patterned with a straight microfluidic channel (**Figure 6B** and **C**). The resulting microchannel width in the hydrogel slightly differed from the nominal diameters of the nylon filaments. However, the microchannels were robustly patterned for nylon filaments with diameters of 50, 150, and 250 µm (**Figure S1B**). The gel chamber contained a scaffolding structure with four poles connected by a top ring to stabilize the hydrogel over longer culture times. The pole structure is connected to the main body of the chip using rated breakpoints. Upon detaching the pole structure from the main chip body, the hydrogel with the embedded tissue can be retrieved for downstream analytical sample preparation, such as histology. The two outer reservoirs fluidically communicate through the microchannel; thus, the addition of fluids within one reservoir leads to gravity-driven flow and fluid leveling through the communicating channel. However, the two outer fluid reservoirs not only equalize the hydrostatic pressure, but the hydrogel chamber also contributes to filling height homeostasis owing to the open microfluidic design. One consequence is that the hydrostatic pressure difference resulting from non-equalized

fluid volumes in the reservoirs and hydrogel chamber leads to the dilation of the microfluidic channel because the hydrostatic pressure acts on the gel phase (**Figure 6D-F**). The dilation of the microchannel depends on the mechanical properties of the hydrogel. Representatively, we show the dilation of a 150 µm microchannel used by default within a collagen-I (COL1) hydrogel with increasing COL1 concentration. While imbalances of fluid filling heights between the reservoir and the gel chamber have a strong effect on the microchannel width in the low concentrated COL1 hydrogel (1.25 mg ml^{-1}), imbalances of the fluid filling heights within the higher concentrated COL1 hydrogel (5 mg ml^{-1}) have lower effects on the microchannel width (**Figure 6G**). The chip can be placed on a rocking shaker to induce gravitational flow on it; thus, no active pump system is required to maintain the cell cultures under flow conditions (**Figure 6H**). To quantify the WSS, we assessed the flow velocity as a function of the tilt angle of the chip by tracking the motion of microbeads within video frames (**Figure 6I** and see Methods). The determined WSS for a nominal 150 µm channel within 2.5 mg ml^{-1} COL1 hydrogel with tilting angles of 7°/13°/25° are exemplarily shown in **Figure S1C**. As expected, the WSS increased with higher tilt angles and the flow rates decreased with time because of the leveling of the filling heights between the reservoirs. As the maximum flow rate of 15 µl min^{-1} on-chip was achieved at a tilting angle of 25°, this tilting angle was set as the default for all experiments. After tilt initiation, half of the maximum WSS was observed after 2 min (**Figure 6J**). This time was used as the frequency for changing the tilt direction and maintaining the bidirectional flow. Using three different nylon filaments with diameters of 50 µm, 150 µm, and 250 µm, the effect of the microchannel diameter on the flow rates and WSS was subsequently investigated (**Figure S1D, E**). A maximum volumetric discharge of 15 µL min^{-1} was calculated at 150 µm diameter in the center of the microchannel at a 25° tilt (**Figure S1D**). Increased microchannel diameters resulted in a greater maximum WSS but a faster reduction in WSS over time (**Figure S1E**). Microchannel diameters of 150 and 250 µm produced shear forces in the range of 1 to 3 dyn cm^{-2}, whereas a microchannel diameter of 50 µm produced negligible shear forces. In the following experiments, we use only chips with a 150 µm diameter and a maximum tilt of 25° inducing a shear force of 3 dyn cm^{-2}, which is at the lower end of the shear force microvessel experience *in vivo*[30].

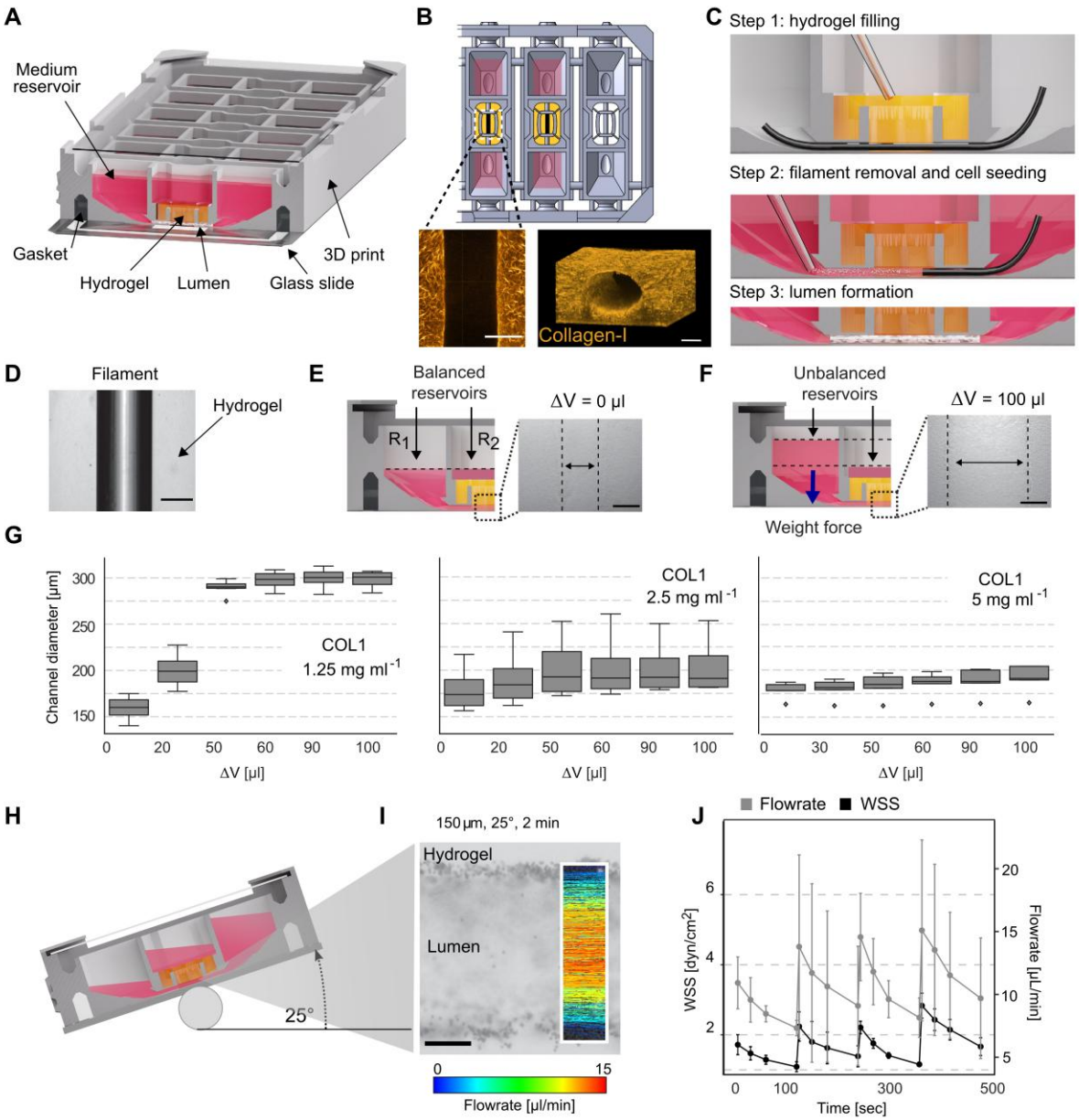

Figure 6 The open microfluidic chip platform for organotypic cell cultures.

(A) Cross-sectional view of the 3D-printed chip. The chip holds six identical unit cells, where each unit cell has two reservoirs connected by a hydrogel chamber for tissue culture formation. (B) Top view of the chip. Zoom-in images show confocal laser reflection images (488 nm) of the Collagen I (COL1) hydrogel chamber (5 mg ml-1) with the patterned microfluidic channel. The microchannel runs 100 ± 10 µm above the glass substrate and connects the two fluid reservoirs. Scale bar, 150 µm. (C) Manufacturing steps of the microchannel. Step 1: A nylon filament is introduced to the chip before filling and polymerization of the hydrogel solution in the middle chamber. Step 2: A cell suspension is pipetted into the reservoirs. Upon mechanical removal of the filament through the reservoir, cells are dragged into the microchannel. Step 3: Cells are cultivated and allowed to form tight endothelial structures. (D) Image of a nylon filament with a diameter of 150 µm in a 2.5 mg ml-1 COL1 hydrogel. Scale bar, 100 µm. (E) and (F) images of reservoirs and hydrogel chamber with balanced and unbalanced fluid volume. Within the open microfluidic chip design, the microfluidic channel in the hydrogel widens depending on the hydrostatic pressure acting on the microchannel. Scale bar, 100 µm.

(G) Box plots show the dilation of the microfluidic channel depending on the COL-1 concentration and volume differences in the reservoirs and hydrogel chamber. Error bars indicate confidence intervals of 95%. (H) Gravity-driven flow is enabled by tilting the chip platform. (I) Flow rates within a microchannel with a nominal diameter of 150 µm were determined by video tracking the microbeads. The representative velocity profile within the microchannel is provided for the maximum tilting angle of 25°. Scale bar, 50 µm. (J) Flow rates on the chip are not constant due to fluid leveling over the reservoirs. The graph shows the time-dependent changes in the flow rates and mean wall shear stress (WSS) inside the microchannel at tilt angles of 25°. The tilting angle was reversed every 2 minutes to maintain a bidirectional gravity-driven flow. Error bars indicate standard deviation.

3.2.2 Formation of the functional perfused endothelial vessel on chip

Next, we applied the chip for the formation of SC-EC *in vitro* vessel structures. Using a two-step induction protocol for ECs, hiPSCs were differentiated in 3D shaking culture[1]. SC-ECs were expanded and seeded at high density (4 Mio. cells ml^{-1}) into the chip with a pre-formed microchannel in a 2.5 mg ml^{-1} COL1 hydrogel (**Figure 7A**). The cells began to adhere to the channel walls within the first hour. Within the following two days, cells were cultivated under either static or bidirectional flow conditions. In both cases, SC-ECs formed a luminal vessel structure adopting the shape of the microchannel, with sprouts developing towards the hydrogel periphery after 2 days of cultivation (**Figure 7B** and **Figure S2A**).

We analyzed the sprouting network parameters within 3D-stacked confocal images in which VE-cadherin was immunohistochemically stained to quantify the differences in endothelial sprouting capability under static or flow conditions (**Figure S2B**). Notably, SC-ECs under flow conditions formed more branches protruding from the lumen in terms of the total number, junctions per branch, and total network length (**Figure 7C-E**) than under static conditions. This higher sprouting behavior was further confirmed by fluorescence signal analysis using VE-cadherin staining (**Figure 7F**). The VE-cadherin signal along the perpendicular axis of the microchannel showed a higher amplitude and length, which represented a higher number and longer sprouts within the samples cultured under flow conditions.

Sprouting analysis indicated that ECs interacted with the extracellular matrix (ECM) and started to remodel the surrounding hydrogel via sprouting angiogenesis. COL1 is one of the most abundant ECM proteins and is a favorable hydrogel for constructing *in vitro* blood vessels[121]. We demonstrated the extent to which the hydrogel formula influenced cellular hydrogel remodeling and sprouting by seeding SC-ECs on a chip at

different COL1 concentrations. At the lowest COL1 concentration (1.25 mg ml^{-1}), the cells visibly remodeled the microchannel by sprouting out of the lumen towards the ECM periphery, leading to significant lumen enlargement. By contrast, at higher concentrations (2.5 and 5 mg ml^{-1}) the lumen diameter was less impaired (**Figure S2C**). At a collagen concentration of 5 mg ml^{-1}, only a few sprout tips were observed. This suggests that denser collagen networks promote lumen stability while impeding the growth of the SC-EC branches. Hereafter, all experiments were performed with a COL1 concentration of 2.5 mg ml^{-1} to maintain the lumen structure and sprouting capability of the SC-ECs. A FITC-dextran assay was performed to test the barrier function of the endothelial lumen. The SC-EC lumen engineered under flow conditions showed higher resistance to FITC-dextran diffusion (40 and 2000 kDa) over the endothelial barrier into the COL1 hydrogel matrix than the SC-EC lumen engineered under static conditions over three days (**Figure 7G** and **H** and **Figure S2D, E**).

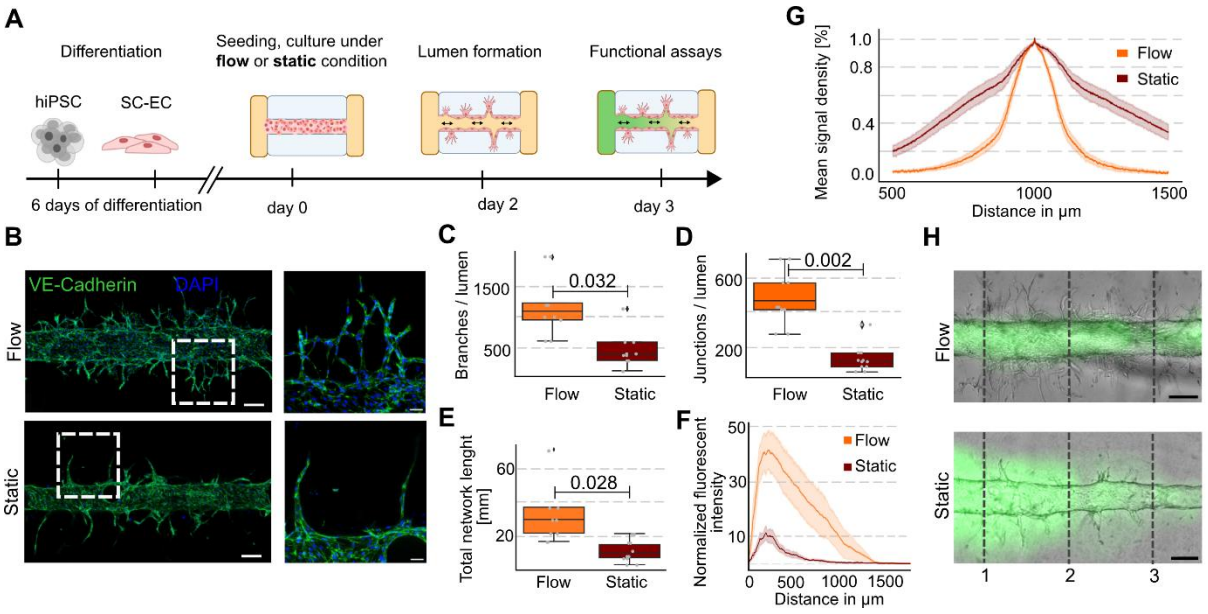

Figure 7 Formation of a functional perfused endothelial vessel on-chip displaying barrier integrity and sprouting angiogenesis.

(A) Experimental outline: stem cell-derived endothelial cells (SC-ECs) are differentiated from human induced pluripotent stem cells (hiPSCs) and seeded in the chip. Functional tests such as *in vitro* vessel integrity test by infusing the lumen with fluorescently labeled fluorescein isothiocyanate (FITC)-dextran are performed after 2 d. (B) Immunofluorescence images of vascular endothelial (VE)-cadherin (EC contact integrity) of 2 d cultured SC-EC under bidirectional flow or static conditions on-chip. Scale bar, 200 µm left and 100 µm right. (C-E) Sprouting network analysis of the SC-EC under bidirectional flow and static conditions showing branches (C) and junctions (D) per lumen and total vascular network length (E); n = 6 from 2 independent experiments; *p* values are calculated using a two-sided t-test and indicated in the figure; error bars indicate a confidence interval (CI) of 95%. (F) Sprout density was measured

using the mean intensity of the VE-cadherin signal on multiple longitudinal axes directing from the outer wall of the microchannel towards the hydrogel area (n=6 of 2 independent experiments, CI=68%). (G) FITC-Dextran assay to evaluate the barrier function of SC-EC vessels. The mean fluorescence intensity signal of FITC-dextran was measured on 3 traverse lines scans per lumen (dotted lines in (H); n=8 of 3 independent experiments, CI: 68%). (H) Images are fluorescence and brightfield overlays, where green denotes the FITC-Dextran signal. Scale bar, 200 µm.

3.2.3 Single-cell transcriptomic and functional analysis of the SC-EC on-chip

Next, we performed single-cell transcriptomic analysis (scRNA-seq) of SC-EC cultured on-chip under shear flow and static conditions to reveal the heterogeneity of cell stages associated with possible maturation, sprouting, or barrier function (**Figure 8A**). We obtained sufficient SC-EC for the scRNA-seq protocol by pooling the SC-EC from one chip, which are 6 functional lumens with approximately 3000 cells each. The live cell recovery rates from the chip were >70% for SC-ECs cultured under flow conditions, demonstrating that the retrieval process was robust. For SC-ECs cultured under static conditions, the live cell recovery rates were lower, indicating a lower viability or higher stress state of these cells (**Figure S3A, B**). Cells retrieved from the chip were used as inputs for sc-RNA-seq. The quality parameters of the sequencing run are shown in **Figure S3C-G**. After high-quality scRNA-seq data filtering, we obtained single-cell transcriptomes of >17k genes from approximately 2000 cells (**Figure S3D**) under both conditions. Seven cell clusters were identified using Leiden[113] clustering (resolution = 0.5) and two-dimensional data reduction (UMAP[84]) of the single-cell transcriptome data (**Figure S4A**). The Leiden clusters were annotated as flow, static, intermediate, barrier, filopodia-like 1/2, and mural cell-like transcriptomic states based on the marker genes (**Figure 8B**, **C,** and **E**; **Figure S4B, C**). Notably, only the mural cell-like cell cluster did not express the EC markers and showed typical vascular smooth muscle cell marker expression, including that of *PDGFRB*, *CSPG4*, *TAGLN*, and *ACTA2*[122]. Others and we have previously shown that ECs and mural-like cells co-evolve during the applied stem cell differentiation protocol[1,123] and that progenitors are still present on day 6 of differentiation. A low fraction of mural-like cells may have resulted from incomplete sorting. The differentially expressed genes (DEGs) for SC-EC cultured under static conditions included the EC markers, such as *EDN1* or *ANGPT2*, which are specific for static SC-EC culture conditions since shear flow stress leads to their

downregulation.[102,124] Furthermore, cells from the static cell cluster shared the expression of stress marker genes, including *ROMO1* and *NQO1*, indicating oxidative stress and cell death[125]. Contrastingly, only 19% of the single-cell reads found in the SC-ECs exposed to wall shear stress were allocated to the static cluster, whereas 39% of the statically cultured SC-ECs were allocated to the static cluster (**Figure 8D**). SC-EC distribution cultured under flow and static conditions within annotated cell clusters is shown in **Figure 8D**. Under flow culture conditions, half the SC-EC population exhibited transcriptomic states of either intermediate (23%) or flow (25%) cell clusters. Furthermore, cells from the flow cluster showed upregulated expression of shear stress markers, including *KLF2*, *KLF4*[102], or *VWF*[126]. Notably, *GJA4* is a shear stress-upregulated gene and enables arterial specification together with the downstream cell cycle inhibitor *CDKN1B*[127], which is also specifically upregulated in the flow cell cluster. This aligns with *MECOM* upregulation in the flow cluster, a regulator of human arterial gene expression[123].

Intermediate clustered cells upregulated the expression of *MMP9,* which is a shear stress-sensitive gene[128] and central for the initiation of angiogenesis in the endothelial progenitors[129]. Cells of the intermediate cluster also express the pro-oncogene *JUN*, which is upregulated in the ECs as an immediate response to shear stress[130]. Approximately 7% of the SC-EC in both static and flow culture conditions were assigned to one of two filopodia-like transcriptomic cell states. Filopodia cluster 1 was positive for VEGF/calcium signaling, and filopodia cluster 2 was correlated with NOTCH and ECM-receptor interaction as revealed by a Kyoto Encyclopedia of Genes (KEGG) pathway analysis (**Figure S4C)**. A representative selected DEG for filopodia cluster 1 was transforming growth factor beta 1 (*TGFB1*), which is known to induce angiogenesis[33]. In addition, *PEAK1* was chosen as unique marker for filopodia-like 2[34]. SC-EC within the barrier cluster upregulated the expression of cell–cell interaction genes (*CLDN5* and *ENG*) as well as gap and tight junction genes (*GJA1* or *JAM3*), which indicated the formation of a cell–cell interaction required for intact lumens[131,132]. Cells from static and flow culture conditions were found in the barrier cluster, suggesting that the prepatterned luminal shape of the hydrogel alone was sufficient for the formation of the transcriptomic cell state. KEGG pathway analysis and Pearson correlation plots supported the annotation and differences in all transcriptomic states, respectively (**Figure 8F**, **Figure S4C**).

RNA velocity[87] was calculated using the sc-RNA-seq flow data to resolve the dynamic changes and interconnectivity of cell clusters (**Figure 8G**). The flow velocity lines point from the static cluster towards the intermediate, barrier, flow, and filopodia-like clusters. Next, we investigated whether the velocity lines indicated SC-EC maturation under flow culture conditions. To this end, we calculated the gene enrichment scores for DEGs obtained from embryonal and adult human endothelial single-cell datasets within the SC-EC single-cell transcriptome data. Strikingly, the DEGs of the embryonic early arterial (Carnegie stage 10 and 11)[133] and the adult artery ECs (human sc-RNA atlas)[82] considerably increased along the velocity lines (**Figure 8H**), thus supporting the maturation effect of SC-ECs under shear flow culture conditions. The gene enrichment score for DEGs of adult lymphatic ECs also increased within SC-EC cultured under shear flow conditions, however, to a lower degree arguing that the on-chip conditions drive cell type maturation towards an arterial-like cell type. Similarly, cells of the mural cell cluster correlated with the transcriptomes assigned to the adult smooth muscle cells. Contrarily, the enrichment analysis showed that SC-EC on-chip did not resemble embryonic cardiac ECs.

Moreover, in the flow, intermediate, barrier, or filopodia clusters the expression profile of ECM proteins changed compared to cells cultured under static conditions (**Figure S4D)**. For example, barrier cells increased the expression of the basal membrane protein Collagen IV, also found by IF stained lumen sections (**Figure S4E).**

Shear stress is known to be a positive regulator of endothelial NO-synthesis[124]. Genes involved in NO signaling belonged to the DEG of the single-cell flow clusters. Vascular cells synthesize NO to maintain healthy tissue function and to control vasodilation[134]. Nitric oxide synthase (*NOS3*) and the NOS3 activating Ca-dependent protein kinase (*CAMK2D*) are upregulated in ECs cultured under flow conditions[135]. Contrastingly, under static cell culture conditions, ECs upregulated genes, such as eNOS interacting proteins (*NOSIP*), eNOS traffic inducer (*NOSTRIN*), and Caveolin-1 (*CAV1*), which form a ternary complex inhibiting NOS3 activity[134] (**Figure 8I**). We determined NO concentrations in the supernatants of the perfused lumens cultured under flow and static conditions using a fluorometric assay to validate the gene expression changes at the functional level. Indeed, NO production was significantly increased in the ECs cultured under flow conditions, whereas NO concentrations in the EC cultured under static conditions were comparable to those in cells grown in a 2D monolayer (**Figure 8J**).

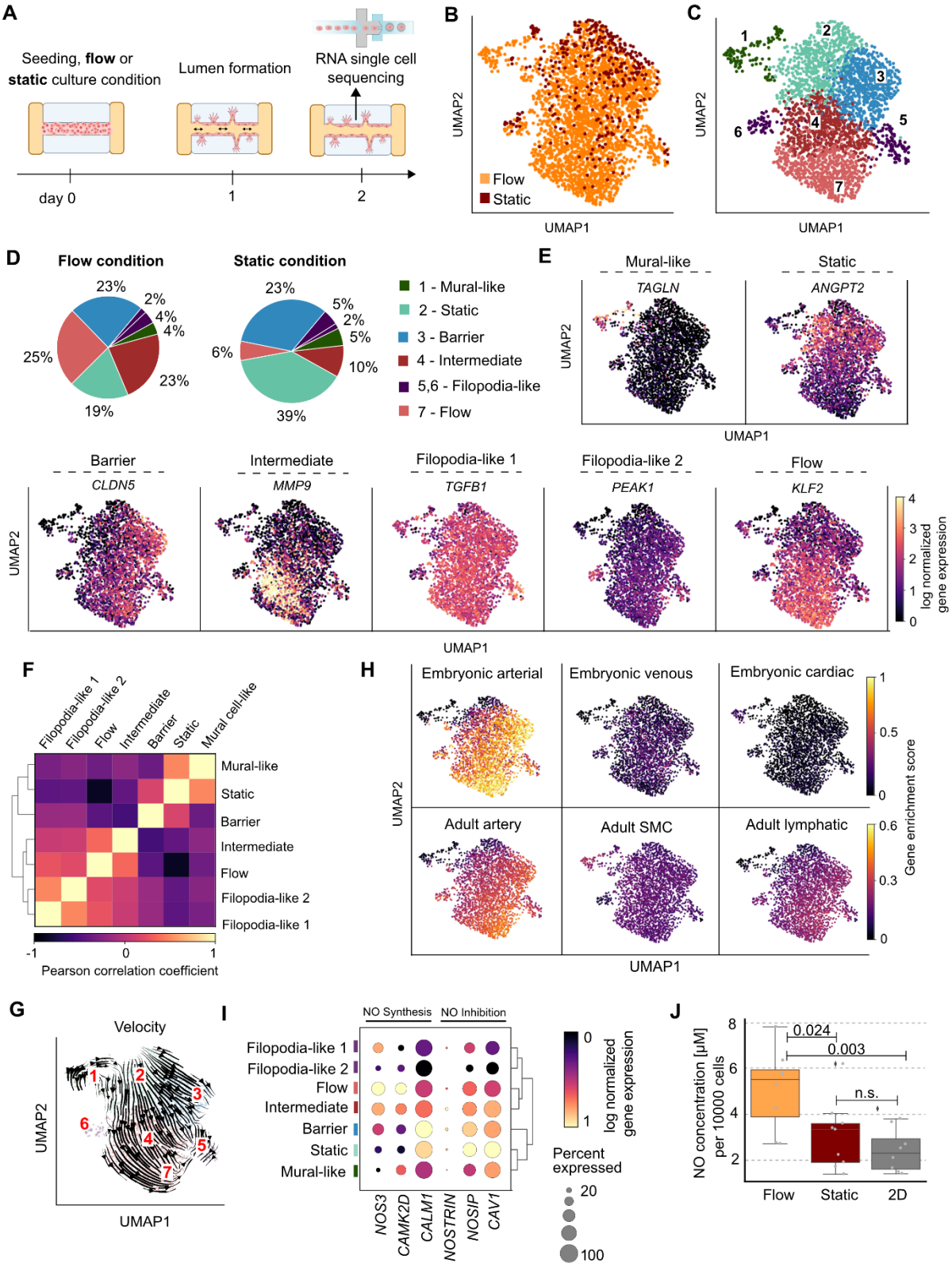

Figure 8 Single-cell transcriptomics reveal specified flow-induced cell clusters reflected by enhanced nitric oxide synthesis in *in vitro* conditions.

Experimental outline: stem cell-derived endothelial cells (SC-ECs) cultured for 2d under bidirectional flow or static culture conditions on-chip. Cells were retrieved from the chip and used for 10x genomics single-cell RNA sequencing. (B) Uniform manifold approximation and projection (UMAP) plot of the two acquired single-cell transcriptomic data sets. (C) UMAP plot

illustrating the seven unique found transcriptomic cell clusters for the SC-EC cultured on-chip. (D) Cell distribution according to the identified cell clusters. (E) Gene expression patterns of the selected cell marker genes used for cell cluster assignments. (F) Pearson correlation plot of the annotated cell clusters. (G) Single-cell transcriptomic velocity analysis. Velocity streamlines showed the transcriptomic state progression of SC-ECs cultured for 2d under bidirectional flow on-chip. (H) Enrichment score of DEGs from embryonic arterial, venous, and cardiac ECs (human embryonic dataset at Carnegie stage 10 and 11) and of adult artery ECs, smooth muscle cells, and adult lymphatic ECs (Tabula Sapiens organ type vasculature dataset) within the on-chip scRNA dataset. (I) Dot plots show expression levels of genes required for endothelial nitric oxide (NO) synthesis and inhibition of the NO synthesis. (J) NO concentrations within the luminal cell culture media of the chip from cells cultured under flow or static conditions. NO concentrations are compared to supernatants of cells grown on a 2D monolayer (N=3; n=8-9 repeats; error bars indicate confidence interval of 95%). NO concentrations were normalized to the total cell count per sample. *P* values were calculated with a one-way ANOVA and Tukeys post-hoc test and are indicated in the Figure

3.2.4 Interfacing the vessel-on-chip platform for downstream analysis

The open OoC platform was designed to enable high-resolution imaging. A working distance of 100 µm between the microchannel and the glass substrate allowed whole-mount imaging of the SC-EC vessel structure (**Figure 9A**). Therefore, immunofluorescence staining can be performed with a low antibody consumption. A z-projection of fluorescence confocal images depicting SC-EC lumen stained for the endothelial marker CD31 is shown (**Figure 9B)** and a 3D reconstruction of the image stack visualizes the distribution of SC-ECs in the lumen (**Supplementary video 1**)**.** Additionally, we stained for the sprouting marker DLL4 and lamellipodia marker ARP3. Lamellipodia appeared at plasma membrane sites free of VE-cadherin as reported before[136] and ARP3 expression was observed in the cell membrane regions next to newly found sprouts. Alternatively to the whole mounts staining, sample sections can be prepared for multiple protein detections in a single lumen. For this, the COL1 hydrogel was retrieved in an unscathed manner by lifting the hydrogel-embedded 3D printed support structures (**Figure 9C**). Hydrogel blocks with intact lumens were then subsequently used for downstream histological analyses. Representative immunofluorescence-stained sections are shown in **Figure 9D**, where we stained selected DEGs, such as Angiopoietin-2, Claudin 5, and KLF4, found in the scRNA sequencing dataset. Approximately 25 sections were obtained from each lumen.

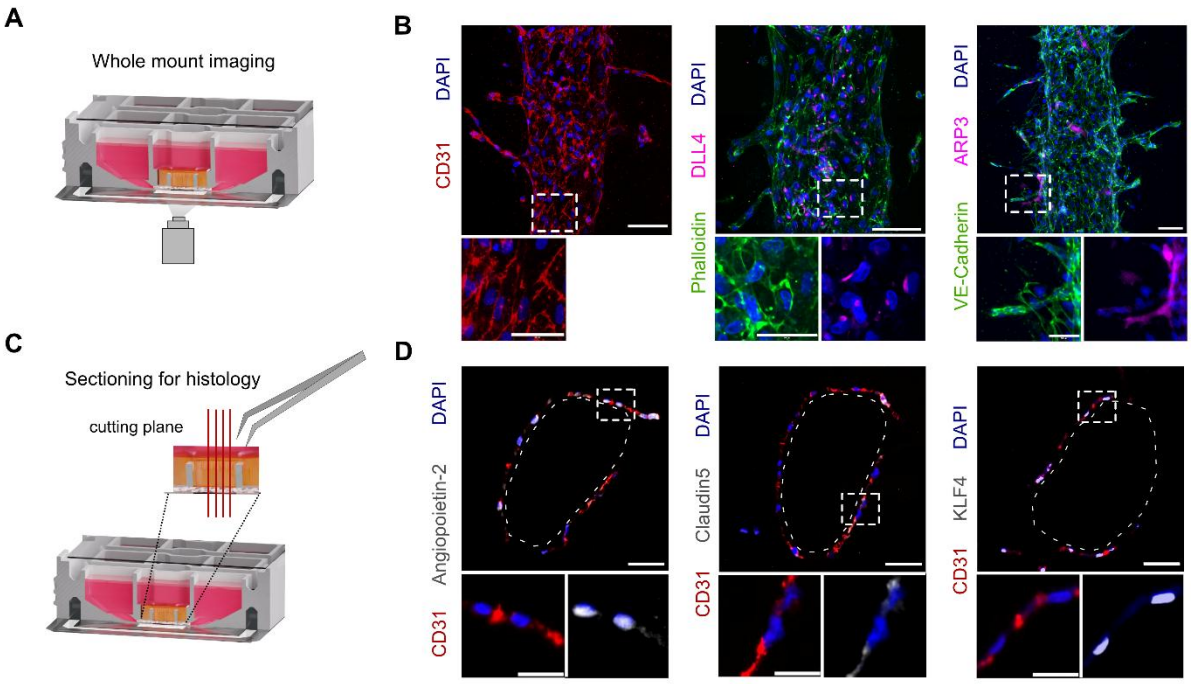

Figure 9 Whole mount and paraffin-section immunofluorescence staining allow for detailed morphological analysis of endothelial tissue.

(A) On-chip whole mount immunofluorescence staining can be directly performed, where concomitantly, the 100 µm distance of the lumen to the glass bottom allows high-resolution imaging. (B) Whole-mount staining of differentially expressed genes (DEGs) expressed in stem cell-derived endothelial cells (SC-ECs) cultivated under bidirectional flow on-chip. EC marker CD31 (scale bar 100 µm), flow-induced marker DLL4 (scale bar 50 µm), endothelial adherence junction marker CDH5, and branching marker ACTR3 (scale bar 50 µm) with zoom-in images (scale bar 20 µm). (C) For performing multiple IF staining from a single sample, the printed scaffold with the hydrogel-embedded vessels is removed using a tweezer. (D) Stainings of static cell marker ANPT2, barrier marker CLDN5, and flow-induced marker KLF4. The scale bar denotes 50 µm and 20 µm for the zoom-in images.

3.2.5 Modeling the early-onset of atherosclerosis by oxidative stress under in vitro conditions on-chip

Elevated blood levels of oxLDL and FFA are crucial drivers of atherosclerosis plaque formation[18,20]. To model the early onset of atherosclerosis on-chip, we treated SC-EC vessels under flow conditions with either FFA or oxLDL (**Figure 10A**) for 48 h. Both FFAs and oxLDL accumulated within the SC-ECs, which was verified using BODIPY staining for all cytoplasmic lipids or using fluorescently labeled Dil-oxLDL (**Figure 10C** and **D**). A FITC-dextran membrane permeability assay was performed to assess the barrier function of the vessels-on-chip after 24h and 48h oxLDL and FFA treatment. While vessels treated with FFA showed no difference in barrier function, vessels treated longer than 24h with oxLDL indicated a small increase in FITC-dextran leakage

(**Figure S5A, B)**. Further, IF stainings showed that the expression pattern of ZO1 changed from a plasma membrane to a cytoplasmic location in SC-EC after 2 days of oxLDL treatment but not after FFA treatment or control samples (**Figure S5C**). A cytoplasmatic location of ZO-1 has been reported upon hypoxia stress induction in ECs[137].

The stimulation responses of SC-ECs were quantified by measuring the proteomic changes using mass spectrometry (LC-MS/MS). Cells from the three lumens were retrieved and pooled to obtain approximately 9000 cells. Protein counts and the dynamic range of proteomic data were comparable for all samples (**Figure S6A-C**). FFA formulation required BSA in the medium and thus the buffer conditions between the samples differed. Principal component analysis and heatmaps showed differences in protein expression between the treatments and respective media controls, as well as coherence between repeats (**Figure 10B, Figure S6D, E**). Differentially expressed proteins (DEPs) from both stimulation experiments were resolved using volcano plots (**Figure S6F, G**). Gene Ontology (GO) term analysis of the DEPs from both treatments showed enrichment of oxidative stress terms and included terms indicating the activation of protective oxidative reagents via the heme-oxygenase system[138] (**Figure 10E, F**). GO terms for the FFA-treated samples included additional terms related to shunting overload of fatty acid activity or obesity-related inflammation, e.g. by the upregulation of toll-like receptor 4 (TLR4) signaling[139]. DEPs found within both treatments and unique to a treatment are shown in the Venn diagram in **Figure 10G**. Both treatments led to the upregulation of heme oxygenase 1 (HMOX1), which is expressed as a protective response to ROS stress[140]. We live-stained the SC-ECs on-chip with a fluorescence indicator (CellROX) for ROS species to test whether oxidative stress was induced by FFA and oxLDL treatment. The normalized mean intensity signal of the CellROX fluorophore (**Figure 10H**) increased in oxLDL-treated SC-ECs with a signal intensity comparable to that of the positive control treatment of the cells with tert-butyl hydroperoxide (TBHP). For FFA treatment, we did not detect an increase in the CellROX signal compared with the respective medium control.

Next, we investigated whether adding the sortilin inhibitor TY52156 could lower oxidative stress in SC-EC. Proteomic analysis showed that a sortilin family member (SORCS2) was upregulated in SC-EC upon FFA (1.56-fold; *p*-adj=0.03) and oxLDL (1.40-fold; *p*-val=0.02) treatment. Sortilin was previously found to be positively correlated with atherosclerosis and cardiovascular disease[141] TY52156 co-treatment

did not lead to a visibly altered FFA or oxLDL accumulation (**Figure S6H**). Notably, in the oxLDL + TY52156 treated samples, the CellROX signal was significantly lower than that in the samples treated with oxLDL alone (**Figure 10H**). In the FFA-treated SC-EC, TY52156 had no significant influence on CellROX signaling.

Considering the enrichment of proteins related to eNOS function (ENG, CYBG, and HMOX1) in the proteome analysis of both conditions we quantitatively measured NO production by SC-ECs on a OoC after oxLDL and FFA treatments. Indeed, NO concentrations in the oxLDL-treated SC-EC vessels were significantly reduced compared to those in the respective medium controls (**Figure 10I**). Here, the sortilin inhibitor TY52156, applied to oxLDL-treated SC-ECs, did not rescue the NO production. The NO assay on the FFA-treated samples did not show any difference compared to the medium control, which aligns with the non-significant CellROX staining. Thus, when compared to oxLDL, SC-EC treatment with FFA leads to different molecular response mechanisms.

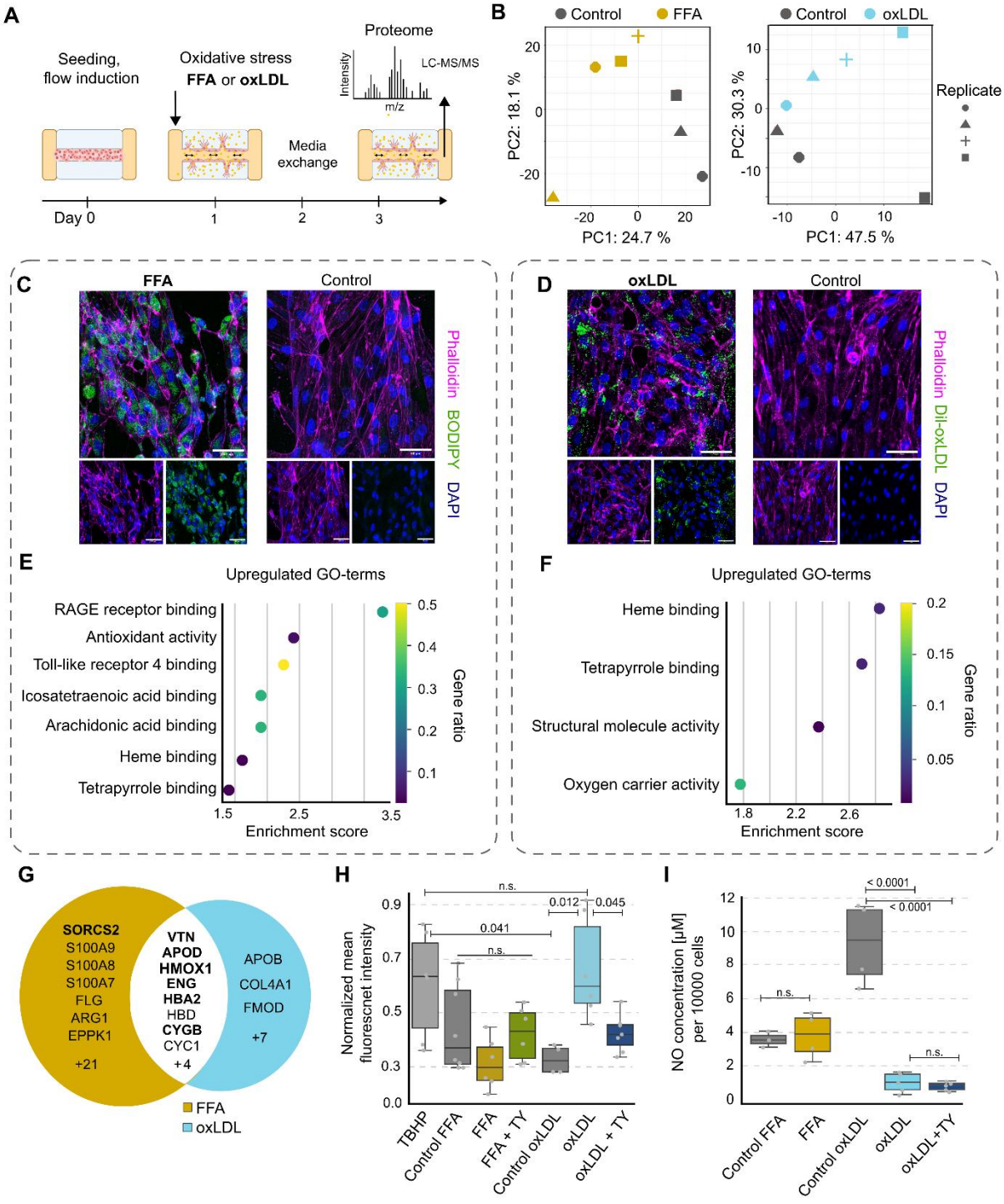

Figure 10 Oxidative stress induction of vessel formed on-chip.

(A) Experimental outline. On day 1, stem cell-derived endothelial cells (SC-ECs) were treated with free fatty acids (FFA) or oxidized low-density lipoproteins (oxLDL). On day 3, proteome and secretome data were acquired using mass spectrometry. (B) Principal component analysis of the proteome data after FFA (n=4) or oxLDL (n=4) treatment and their respective medium controls (n=3). (C) Immunofluorescent images of fatty acids with BODIPY in FFA treated samples vs control. Scale bar, 50 µm. (D) Immunofluorescent images of fluorescence labeled Dil-ox-LDL treated samples vs control. Scale bar, 50 µm. (E) Top 8 upregulated GO terms in the FFA condition compared to the untreated control. (F) Top 4 upregulated GO terms in the

ox-LDL condition compared to the untreated control. (G) The Venn diagram highlights the selected proteins upregulated in the FFA and oxLDL conditions and their overlap. (H) Analysis of the reactive oxygen species in the treated samples versus control. Samples were live-stained for Hoechst and CellROX reagent (Thermo) and imaged, and the CellRox signal intensity was normalized to the Hoechst intensity. ECs were treated with TBHP as a positive control. Data are presented with a confidence interval (CI) of 95% for the error bars, and n ≥ 12, except for TBHP with n = 3. Boxplot outliers were removed when indicated in the python package seaborn. (I) Cell count-normalized NO concentration (µM) in supernatants of treated samples vs their respective control on day 3. Error bars indicate a CI of 95%, and n = 3–5. *p* values of (H) and (I) were calculated with a one-way ANOVA and Tukeys post-hoc test and are indicated in the figures.

To further investigate the oxidative stress response of the SC-EC, we measured the secretome of the cells. For this purpose, we used the flow-through volume in the reservoirs of the chip for LC-MS/MS analysis (**Figure 11A**). 1,939 secreted proteins with high confidence level, retrieved over a time interval of 24h from SC-EC treated with oxLDL, were identified by mass spectrometry. 152 proteins of the secretome were up- or downregulated by a 1.5-fold change in comparison to the control, from which 45 contained a signal peptide for active secretion into the blood[118]. A GO term analysis of DEPs of the secretome with active secretion signals showed enrichment of proteins for HDL and chylomicron remodeling (**Figure 11B**). Among the upregulated proteins in the secretome were members of the apolipoprotein family (**Figure 11C**). For example, the secreted APOC3 and APOA1 are known to change NO synthesis of ECs and linked to pathophysiological processes leading to cardiovascular disease (CVD).

Within the secretome of SC-EC treated with FFA 693 proteins were determined, where only 18 were differentially regulated in comparison to the control sample (**Figure 11B)**. SC-EC secretomes in response to FFA and oxLDL treatment have no overlap showing once more the differently induced stress. Notably, in agreement with the proteome measurements the FFA treatment led to an increased secretion of the SORCS2 (**Figure 11D**).

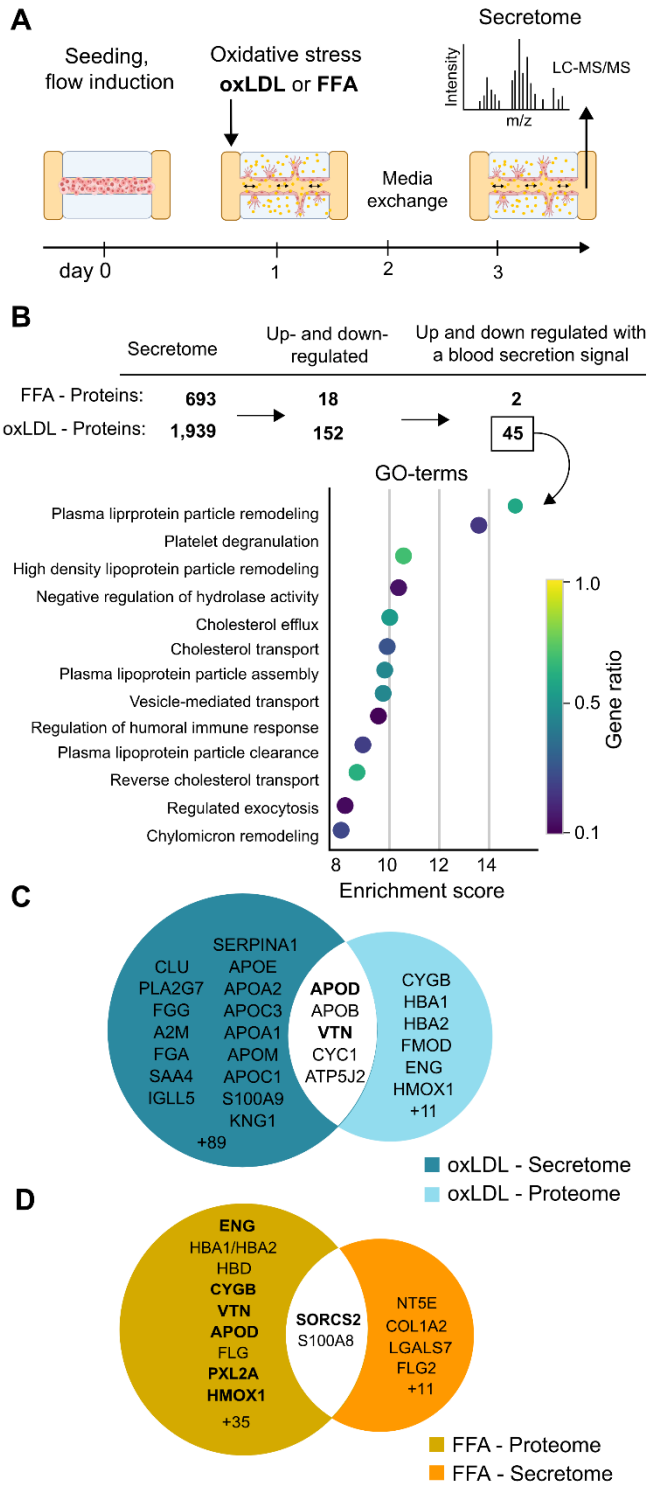

Figure 11 Secretome analysis of oxLDL and FFA treated SC-ECs on-chip.

(A) Experimental outline: SC-ECs were treated with oxLDL and FFA on day 1. Supernatants were collected from the chip reservoirs on day 3 for a LC-MS/MS analysis. (B) oxLDL treatment resulted in up- and downregulation of secreted proteins with and without export signal compared to a control sample without cells. GO term analysis of the differentially secreted proteins with blood secretion signal revealed a response of the cholesterol metabolism to the oxLDL treatment. (C) and (D) Venn diagram highlights proteins upregulated in the secretome and matched proteome of SC-EC treated by oxLDL and FFA.

3.3 Discussion

In this study, we manufactured an open microfluidic platform for engineering organotypic endothelial vessel structures. The open microfluidic design enables the platform to interface with all state-of-the-art analytical technologies, including single-cell RNA sequencing, proteomics by LC-MS, and high-resolution imaging. Concomitantly, engineered endothelial tissues can be functionally assessed under mechanical- and fluid-controlled culture conditions. The manufacturing of the chip platform was robust, as validated by more than 500 lumens in the presented dataset. Although we only functionally analyzed lumens using COL1 hydrogels, microchannel formation was also positively confirmed for Matrigel or fibrin hydrogels (data not shown), in support of general applicability of our organ-on-chip platform for all commonly used tissue microenvironments.

Upon on-chip adjustment, our gravity-driven flow-culture microenvironment revealed wall shear stress of up to 3 dyn cm^{-2}. This value correlates with physiological flow in microcapillaries but unsurprisingly remains lower compared to flow in larger vessels[30]. Generated on a rock shaker and hence bidirectional, the functional validation that our SC-derived EC vessel structures recapitulate vascular barrier integrity or physiological process as sprouting.

We previously resolved the transcriptomic trajectory of SC-ECs during microvessel formation in a hydrogel microenvironment[1]. In this study, we used the same SC-EC for the luminal vessel structure. Single-cell transcriptomic data, particularly velocity analysis, revealed dynamic cell state changes of SC-EC from static to flow culture conditions. Live/dead staining of SC-ECs on the chip under flow and static conditions revealed no differences (**Figure S3A**), however, SC-EC retrieval from the on-chip static culture condition resulted in a higher dead cell count, suggesting generally lower cell stress of SC-ECs under flow culture conditions. This is probably related to the expression of stress-related genes like *NQO1* or *ROMO1*[125], especially in the “static” cluster. Notably, the resolved SC-EC cell states were in accordance with the morphological and functional phenotypes of the chip, including sprouting, barrier-forming, and flow-exposed ECs. SC-EC under shear flow upregulated the shear stress-responsive genes essential for vascular function, including *KLF2/KLF4* under flow conditions[143]. Most strikingly, the higher transcriptomic correlation of the SC-EC cultured under flow culture conditions with adult arterial ECs demonstrated the flow

maturing effect on the SC-ECs. Staining for endothelial markers (CD31), sprouting markers (DLL4 and ARP3[136]), static marker (ANGPT2[102]), barrier marker (CLDN5[132]), and flow induction marker (KLF4[102]) substantiated the single-cell transcriptomic data at the protein level, and hence to translate into biological function.

Another central finding derived from our vessel-on-chip model is the identified transcriptomic upregulation of NO synthesis, respective signaling genes, such as eNOS (*NOS3*), and *CAMK2D,* under flow culture conditions. In stark contrast, SC-EC cultured under static conditions revealed increased expression of genes known to downregulate eNOS function, e.g. *NOSTRIN*, *NOSIP*, and *CAV1*[134]. An on-chip quantitative assay (**Figure 8J**) indeed verified the opposing effects of shear versus static culture conditions on NO synthesis, and by extension, on the *in vivo* endothelial cell behavior[144]

Beyond the characterization of the organotypic endothelial cell culture on-chip, we validated the general functional relevance of the chip platform by modeling the pathogenesis of atherosclerosis. Given that oxLDL particles are involved in the induction of the early characteristic events of atherosclerosis[145] and excess FFA are present in patients with atherosclerosis, we treated our SC-ECs with FFA or oxLDL to potentially address FFA pathomechanisms[20]. One hallmark of oxLDL is the uncoupling of NO production in the ECs via eNOS inactivation[18]. Functional changes, high ROS production, and reduced NO synthesis were indeed observed in the SC-EC vessels on-chip. The proteome of SC-ECs under oxLDL treatment reflected the ROS-induction, ER stress, and antioxidant stress responses. Particularly, the DEPs ENG[142], CYBG[146], and HMOX1[140] are known regulators of endothelial NO synthesis and mechanistically link induced ROS with the functional phenotype of reduced NO synthesis. Notably, the increased ROS occurrence upon oxLDL treatment was ameliorated in SC-ECs by adding the sortilin inhibitor TY52156. However, TY52156 did not rescue NO production, indicating that either the ROS-reducing effect of TY52156 could not compensate for NO-synthesis or both responses not being directly interlinked.

Additionally, FFA treatment induced a proteomic stress signature in SC-ECs with overlapping DEPs in response to oxLDL stress. In contrast to the oxLDL treatment and to *in vivo* experimental data, NO production and ROS concentrations were not altered compared to the controls. One explanation for this finding can be the relatively short treatment of 48 h. FFAs are stored in the SC-ECs in small lipid droplets as shown by

the BODIPY staining (**Figure 10C**). Comparably to *in vivo* conditions, endothelium initially buffers excessive FFA loads by storing them in lipid vesicles and degrading those lipids by lipolysis[147]. Therefore, long-term *in vitro* studies are required to answer this question. Notably, an immediate ROS-protective response was initiated through the upregulation of the heme-oxygenase system for both treatments. Vitronectin was an additional upregulated DEP after oxLDL and FFA treatments. Evidently, vitronectin is central to atherosclerosis progression[148]. Elevated vitronectin levels have been suggested as a potent biomarker of coronary artery disease[149]. Vitronectin detection within the secretome after oxLDL treatment underpins the relevance and applicability of the chip for biomarker discovery.

In summary, we developed a robust and easy to use open organ-on-chip platform for screening parallel endothelial functions using standard laboratory equipment. The reported integration of stem cell-derived endothelial cells offers the opportunity to study *in vitro* endothelial development, tissue-specific toning, and immune interactions at high resolution and at single-cell levels. Beyond the increasing number of vessel-on-chip platforms, our open and general design of the chip allows it to 'host' seamlessly any epithelial cell type. Combined with the open hydrogel design, our setup facilitates the engineering of more complex and particularly vascularized tissues in a 'plug and play' manner. More broadly, our platform opens avenues for universal use to engineer larger and complex tissue/organs considering the integration of gene editing tools or patient-specific stem cell lines. Our approach thus serves the urgent need to replace animal models/reduce animal use by developing a functionally reliable and easily customizable vascularized human organ-on-chip platform.

Limitation of the study

One limitation of our study is the bidirectional laminar flow profile at a lower wall shear stress regime of up to 3 dyn/cm^2 on the vessel-on-chip platform. Under physiological conditions, blood flow occurs unidirectional, where the wall shear stresses vary largely depending on organ function, vessel size, or viscoelastic parameters of the blood. For example, shear rates in capillaries or lymphatic vessel range are in the order of 2 dyn/cm^2, whereas in larger arteries the shear stress ranges from 10 as high as 70 dyn/cm^2 [31]. Engineering *in vitro* tissue models on chip is a balance between simplicity in terms of cost-effective handling and screening versus the complexity of the *in vivo* tissue. The presented vessel-on-chip platform provided a dynamic microenvironment, in which the SC-

ECs established a complete endothelial barrier function, matured to arterial-like ECs, showed NO-secretion comparable to *in vivo* vessels, and enabled higher throughput screening. On the other hand, perturbed flow, which is defined as turbulent flow at low shear stress arteriosclerosis is promoted under *in vivo* conditions. To which extent the bidirectional flow on-chip, but also long-term treatments with oxLDL or FFA contribute to the atherosclerosis model remains to be resolved. From a future perspective, unidirectional flow and higher wall shear stress can be established on our chip by adopting gravity flow concepts developed for closed[150] microfluidic channel networks, increasing the hydrodynamic flow pressure by increasing the volume of the fluid reservoirs, or the tilt angle of the chip.

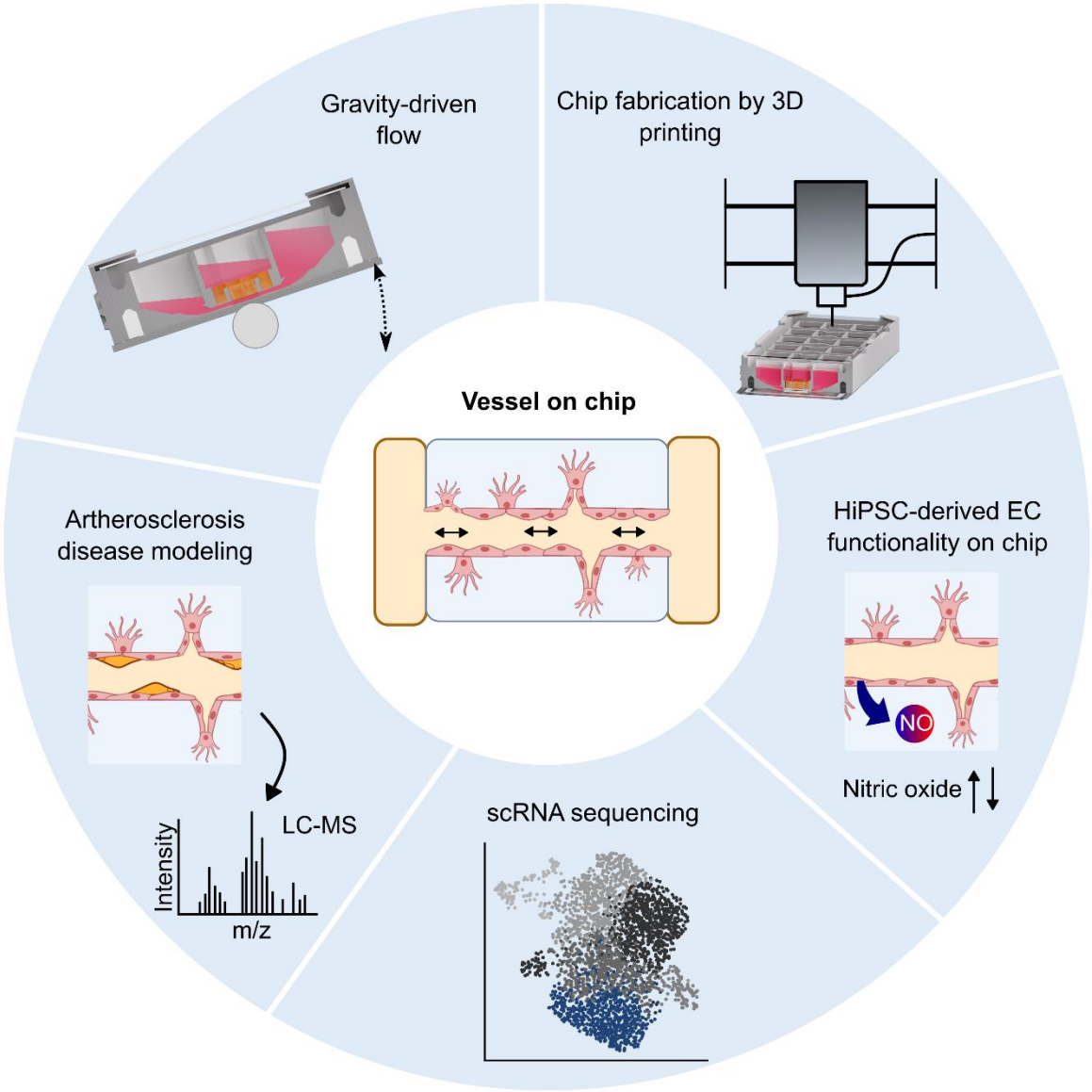

Figure 12 Graphical abstract summarizing vessel-on-chip achievements.

The microfluidic platform was based on a polymer scaffold printed by 3D stereolithography. HiPSC-derived endothelial cells were seeded into a prepatterned lumen inside a physiologic hydrogel matrix on-chip, before exposing to gravity-driven flow on shaker. Endothelial cells

organized towards functional endothelial vessel with protruding angiogenesis and matured vascular function, e.g. NO-synthesis. The platform was exploited for various downstream analysis as scRNAseq or LC-MS/MS for modelling healthy and diseased vascular biology.

3.4 Declaration of contributions

The experiments, analyses, and results described in the recent chapter were carried out equally by Caroline Remmert and me. These included the differentiation of hiPSCs into endothelial cells, their sorting and culture, seeding and maintenance of the chip, as well as the functional analyses such as the FITC-dextran assay, NO assay, ROS analysis, and whole-mount immunofluorescence staining. Additionally, we performed the scRNAseq experiment and prepared samples for proteome and secretome analysis. Together, we also conducted the analysis of sequencing and mass spectrometry data. The chip depicted in Figure 6 was prepared by Julius Perschel, Munkhtur Otgonbayar, and Michel Moussus, with design elements refined through feedback iterations based on experimental results obtained by Caroline Remmert and me. The mass spectrometry measurements were performed by Christine von Toerne. The study design was developed equally by Caroline Remmert, Matthias Meier, and me, with Bilal Sheikh providing guidance on the FFA treatment approach. The manuscript was jointly written by Caroline Remmert, Matthias Meier, and me. Details of author contributions are also outlined in the Cell Reports publication.

Acknowledgments

This work was supported by the Helmholtz Pioneer Campus, the eIslet project of the BMBF (grant number 031L0251), and ERC Consolidator Grant (number 772646). We thank Daniel Kokotek, Ioannis Deligiannis, Celia Martinez, Inti I.A. de la Rosa Velazquez and G. Eckstein for helping with the sample preparation and performing the NovaSeq sequencing. We thank Stefan Veit, Revanth Coimbatore Varadarajan, and Che-Wei Chang for manufacturing of the chips. Further we thank Thomas Schwarz-Romond for critically reading the manuscript.

3.5 Extended data

Supplemental figures can be found in the publication: Marder, M.*, Remmert, C.*, Perschel, J. A., Otgonbayar, M., von Toerne, C., Hauck, S., Bushe, J., Feuchtinger, A., Sheikh, B., Moussus, M. and Meier, M. (2024). Stem Cell-Derived Vessels-on-Chip for Cardiovascular Disease Modeling. Cell Reports. doi: 10.1016/j.celrep.2024.114008.

4 Human vascularized adipose tissue organoids reveal endothelial-adipocyte interactions at single-cell resolution

This chapter is cited from the submitted manuscript: Marder Maren*, Wiedenmann Sandra, Oliveira Fabiana, Kentischer Zoë E., Remmert Caroline, Zheng Yiran, Sheikh Bilal, Meier Matthias. Human vascularized adipose tissue organoids reveal endothelial-adipocyte interactions at single-cell resolution.

Adipose tissue (AT) serves as the body's primary energy reservoir, with white adipose tissue (WAT) as its predominant form. Beyond energy storage, WAT plays a crucial role in maintaining systemic metabolic and hormonal homeostasis[43]. The expansion of WAT during obesity has been linked to metabolic syndrome-related complications such as Type 2 Diabetes Mellitus[151]. In mammals, WAT is distributed across various anatomical sites, with major depots broadly classified as subcutaneous (beneath the skin) and visceral (surrounding abdominal organs). Additionally, smaller WAT depots are found in diverse regions, including bone marrow, perivascular, epicardial, or peri- and intermuscular areas[152]. While the mesodermal development of WAT has been extensively studied,[153] recent advances in single-cell RNA sequencing (scRNA-seq) have revealed heterogeneity of adipocyte subtypes within these discrete WAT depots[82,154]. Moreover, scRNA-seq studies showed that adipocytes exhibit remarkable plasticity, adopting cell states dynamically to metabolic demands and physiological conditions[155]. However, the regulatory mechanisms underlying this plasticity remain unclear.

To rapidly adapt to metabolic changes, AT is highly vascularized, with each adipocyte located adjacent to at least one microvessel in the lean state[5]. Blood vessels within AT facilitate the transport of oxygen and nutrients to adipocytes. Additionally, the stromal vascular bed serves as a microenvironment that regulates adipogenesis by hosting adipocyte precursors and a diverse group of mesenchymal cells alongside the endothelial cells of the vessels[156]. As WAT expands, its vascular network must also grow to support healthy fat storage and prevent hypoxia-related dysfunction[53,54,157]. In mice, microvascular growth precedes the maturation of fat cells during fat pad development, with new adipocytes subsequently differentiating and growing alongside the newly formed vascular branches[158]. Furthermore, the presence of vasculature enhances adipocyte differentiation and maturation[70]. Conversely, inhibition of angiogenesis in WAT of mice prevents the expansion of adipose tissue[53,54,159].

Thus, angiogenesis is considered a requirement for adipogenesis and promotes the expansion of the WAT during the progression of obesity[160]. In this regard, it is not surprising that obese individuals exhibit vascular abnormalities that correlate with their metabolic health state[81]. These differences may manifest as a loss of vessel density due to the increased spacing of adipocytes during hypertrophy or as local endothelial dysfunction triggered by the release of fatty acids and cytokines from adipocytes[57]. Therefore, a close spatial relationship between blood vessels and adipocytes is mutually dependent on development and health state. Importantly, the underlying signaling pathways that pattern the local tissue-specific functional endothelial cell types, and dynamically control the metabolic state of endothelial cells referred to as cell tone remain largely unknown[81].

One major challenge in resolving the heterogeneity and diversity of WAT-endothelial cell (EC) interactions at the cellular level stems from the difficulties associated with conducting longitudinal or cross-sectional human cohort studies. These studies require extended observation periods and are affected by substantial variations in personal lifestyle, nutritional patterns, and genetic or metabolomic profiles. Additionally, cross-species transfer of transcriptomic data as an alternative is limited by significant evolutionary differences between commonly used model organisms such as mice and humans[161]. To address this knowledge gap, we aimed to develop and functionally characterize a human-centered, controllable *in vitro* vascularized WAT model.

WAT only organoid models exist[162–164] but miss hallmarks of the complex *in vivo* perivascular niche. Co-cultures of adipocytes and immortalized ECs embedded in a 3D extracellular matrix form vascular networks with improved adipocyte differentiation and function[66,67]. However, achieving *in vivo* like WAT maturation in the presence of ECs remains challenging. The known reciprocal effects of media inducing adipogenesis versus angiogenesis limit simultaneous adipocyte development and vascularization, highlighting the need for balanced media and growth conditions[78,79]. Currently, cell culture models predominantly use human adipose-derived stem cells (hASC) due to their scalability[67], since primary adipocytes have shown buoyancy effects. For ECs, primary cells or AT-derived microvascular fragments most closely resemble the *in vivo* counterparts but present with rather undefined cellular composition, are potentially primed for the organ of origin[165], and exhibit limited expansion capacity. Recently, we characterized hiPSC-derived ECs (SC-EC) for their

scalability and maturation potential in a perfused vessel-on-chip system[2], highlighting their utility for tissue engineering.

In this study, we engineered stem cell-based *in vitro* vascularized adipose organoids (vAO) using hASC and SC-ECs. Our adipocyte organoids were morphologically and functionally characterized across different cell culture media, assessing endothelial vessel formation, adipocyte differentiation, β-adrenergic-induced lipolysis, and insulin-induced glucose uptake. Subsequently, we performed single-cell transcriptome analysis to uncover the co-developing cell types, -states, and crucially, were able to interrogate the signaling networks at play during adipogenesis and angiogenesis within the vAOs, e.g. at close to physiological conditions. Finally, we confirm by functional abrogation of PDGF signaling that vessel maturation controls lipolysis of WAT.

4.1 Material and methods

4.1.1 Statistical analysis

For statistical analysis, a custom-written Python code with the scipy.stats function was used. Details about replicates of experiments and samples are stated in figure legends. Data were tested for normal distribution and variance homogeneity before the statistical test decision as described in figure legends.

4.1.2 Materials availability

This study did not generate new unique reagents.

4.1.3 Data and code availability

The code for scRNA-seq analysis has been deposited on GitHub (https://github.com/MeierLabMiBioEng/Vascularized-adipose-tissue-organoids) and is publicly available. Raw data and processed data are publicly available on the Gene Expression Omnibus repository under accession code GSEXXXX. Any additional information required to reanalyze the data reported in this paper is available from the corresponding author upon request.

4.1.4 Experimental model and study participant details

Experiments were conducted using a hiPSC line, which was kindly provided by Prof. Lickert (Helmoltz Zentrum Munich) and is registered in the human pluripotent stem cell registry (https://hpscreg.eu) under the name HMGUi002-A. The cell line was derived from a Caucasian male donor.

4.1.5 Generation and cultivation of SC-ECs

For SC-EC generation a hiPSC line was used, kindly provided by Prof. Lickert, which is registered in the human pluripotent stem cell registry (https://hpscreg.eu) under the name HMGUi002-A. For hiPSC to SC-EC differentiation and purification, we applied an established protocol[29] as described in our recent publications[1,2]. For SC-EC cultivation in 2D, plates were precoated with 5 ng/mL fibronectin (Life Technologies, 33010018) for 30 min at RT before seeding cells in StemPro-34 complete (Sigma Aldrich, 10639011) supplemented with 15% FBS (Sigma Aldrich, F0804), 100 ng/mL VEGFA (PeproTech, 10-20-100) and 100 ng/mL FGF-2 (Miltenyi Biotech,130-093-838), from now on referred to as ECGM (endothelial cell growth medium). Media was changed every other day. For SC-ECs passaging, cells were washed once in DPBS, and detached with Accutase (Sigma Aldrich, A6964) for 3 min at 37°C. Accutase reaction was stopped with DPBS + 10% FBS and cells were centrifuged at 200g for 5 min before reseeding in ECGM at a 1:2 ratio on 5 ng/mL fibronectin- precoated (bovine, Life Technologies 33010018) plates. SC-ECs were used for experiments until passage 6. For cryo-preservation SC-ECs were detached and the pellet was resuspended in FBS with 10% DMSO (APP A3672,0250, Th. Geyer).

4.1.6 Cultivation of human adipose-derived stem cells in 2D

Isolated hASCs from subcutaneous adipose tissue of a female, lean patient with no Type 2 Diabetes Mellitus diagnostics were purchased from Zen-Bio (ASC-F, Lot: ASC062118A, BMI<27) and expanded according to the manufacturer's protocol in PM-1 medium (Zen-Bio, 088PM-1). hASCs were cryo-preserved once for expansion of cells from the manufacturer’s stock vial using the same procedure as for SC-ECs. hASCs were expanded until passage 7 and passed once a week. For passaging, cells were split 1:2 with Trypsin/EDTA (0.25%, Sigma Aldrich, 25200056), and the reaction was stopped with PM-1 medium. Cell media was changed every other day.

4.1.7 Seeding and cultivation of 3D vascularized adipose tissue organoids

For the formation of 3D hydrogel cultures, 2.5 mg/mL collagen I hydrogel was prepared. For this, collagen I (4.63 mg/mL, Corning, 354236, LOT 2124001) was mixed with a batch-specific neutralization solution (100 µL PBS (10x) (Thermo Fisher Scientific AM9624), 8 µL NaOH, 352 µL distilled, pure H2Odd) to titrate the

hydrogel at a pH of 7 in the targeted collagen concentration. In between, SC-ECs and hASCs were detached, counted, and mixed in their corresponding ratio as explained in the text. AOs consisted of 18.000 hASCs per organoid, vAOs, and vSVFOs of 22.500 cells in total per organoid (e.g. for the 80:20 condition 18.000 hASCs and 4.500 SC-ECs). After a centrifugation step (300g, 3 min), the supernatant was removed cautiously and 7.5 µL collagen I per organoid was added to the pellet on ice. Cell-hydrogel suspension for 15-30 organoids was prepared into one 1.5 mL tube simultaneously. Cell-hydrogel mix was mixed vigorously by pipetting up and down 10 times. Cell-hydrogel mix remained on the ice during seeding, Then, 7.5 µL cell-hydrogel mix per well was placed as a drop into a µ-Slide 15 Well 3D (ibid, 81501, untreated) at RT. Between each pipetting step, the cell-mix was pipetted up and down once more. Cell-hydrogel mix was allowed to harden in the incubator for 30 min before 50 µL medium per well was added for further cultivation. On the next day, hydrogel-cell aggregates are flushed gently away from the plastic bottom by pipetting up and down next to the hydrogel allowing contraction and rounding up to organoid shape. AOs and vSVFO were cultivated only in ADM or ECGM respectively, whereas vAOs, ADM, and ECGM (as described above for SC-EC culture) were mixed in the described ratios. ADM consisted of DM-2 (Zen-Bio, 088DM-2) from day 1 to 7 and of AM-1 (Zen-Bio, 088AM-1) from day 7 to 14 according to the manufacturer's protocol for hASC differentiation. Media change was performed every 2 to 3 days until day 14 while releasing spheroids from plastic during each media change. Additionally, from day 10 on, the release of organoids from plastic was repeated every day.

4.1.8 Genetic knockdown of endothelial cells by lentiviral transduction

3.33 µg of shRNA mission vectors (Sigma, CSTVRS, scrambled, PDGFB), and packaging plasmids pMD2.G (1 µg) and psPAX2 (2.5 µg) (Addgene vectors #12259 and #12260, deposited by Didier Trono), were transfected lipid-based (Lipofectamine 2000, Thermo Fisher Scientific, 11668019) into 60% confluent 293T cells to produce viral particles. Viruses were harvested 48 and 96 hours after transfection. hiPSCs (HMGUi001-A) were transduced with lentiviruses, and selected with puromycin (0.4 µg/mL, Santa Cruz, sc-108071). The minimal concentration required to kill hiPSC was titrated to determine the Puromycin concentration for the selection of vector-treated cells with Puromycin resistance. Transduced hiPSCs were cultivated in a standard cell medium with continued Puromycin treatment (0.2 µg/mL) as described for standard hiPSC cultivation. Transduced hiPSCs were cryo-frozen, thawed, and passaged three

times with Trypsin-EDTA to remove residing viral particles. Viral-free cell culture was confirmed by Lenti-X™ p24 Rapid Titer Kit (Takara, 631476). Knockdown of *PDGFB* was confirmed by qRT-PCR. hiPSCs were differentiated into SC-ECs. Successful differentiation was confirmed by flow cytometry analysis as described before[1,2]. For stress reduction, SC-EC were not FACS sorted, but expression of CD31 and CD140b was checked again after passage 2 by flow cytometry. SC-EC cultivating on fibronectin leads to selection of CD31 positive cells with a proportion of >90% after 5 passages as we showed recently[1]. SC-ECs with specific knockdowns were implemented into vAOs with 75-25 ADM-ECGM media mix conditions and cultivated as described above.

4.1.9 Wholemount staining and imaging

For whole-mount immunohistochemistry (IHC-Whmt) staining of organoids, cells were fixed with Histofix (4% PFA, Carl Roth, P087.4) for 30 min at RT and washed with DPBS afterward. After a 30 min permeabilization step at RT with DPBS + 0.1% Triton X-100 (Sigma Aldrich, 93443), samples were blocked in blocking buffer (DPBS, 0.1% tween 20 (BioRad, 1610781), 1% BSA (Sigma Aldrich, A8806), 0.1M glycine (Sigma Aldrich, G5417) for 2h at RT on shaker with 45 rpm. For staining, antibodies were mixed with blocking buffer without glycine (staining buffer) and incubated for 2 days at 4°C on a shaker (45 rpm) protected from evaporation. Primary antibodies were washed out with washing buffer (DPBS + 0.1% tween 20) three times à 10 min on a shaker (45 rpm) before incubation with secondary antibodies in staining buffer overnight as for primary antibody incubation. Where implemented, DAPI (Sigma, 1:100, 62248), BODIPY (4,4-difluoro-1,3,5,7,8- pentamethyl-4-bora-3a, 4a-diaza-s-indacene, Life Technologies, D3922, 1:100 from stock of 1mg/mL) or Phalloidin (Phalloidin-Atto-647, Abcam, ab176759,1:200) were added to secondary antibody solution. Then, samples were washed three times (10 min, on a shaker with 45 rpm) in washing buffer before mounting in Vectashield plus (Biozol, VEC-H-1900-10). For confocal imaging, organoids were imaged for lipid droplet (BODIPY), endothelial (CD31, Thermo Fisher Scientific, AB_10981955, 1:100), and DAPI signal in 5 µm z-stacks in a depth of 100 µm. Z-stack was converged to a 3D projection in Fiji/ImageJ[108]. All IF stainings were imaged on a confocal microscope (Zeiss Axio Observer LSM 880, Zeiss Zen black software). Brightfield imaging was performed on an epi-fluorescent microscope (Zeiss Axio Observer Z1, Zeiss Zen Blue software).

4.1.10 Sprouting network analysis

For sprouting network analysis, 3D-stacked images of CD31 staining were batch-filtered in Fiji (i.e. CLAHE, Otsudark auto-threshold, median filter). For acquiring branching parameters, Fiji's "skeletonize 2D/3D" and "Analyze skeleton 2D/3D" tools[166] were applied on filtered and binarized images as in our previous publication[2].

4.1.11 Lipid droplet size analysis

In analogy to the vessel analysis, a 3D projection of the BODIPY signal was created by confocal imaging. The ImageJ plugin StarDist[110] was used to segment lipid droplet shapes and quantify lipid droplet size and amount. In a Python script, segmented lipids were first filtered for a mean intensity threshold (mean gray value >20) and a minimum size threshold (>70 µm²) before categorizing each passed droplet into lipid droplet size categories.

4.1.12 Spheroid size analysis

On day 14, spheroids were imaged in the brightfield channel with an epi-fluorescent microscope (Zeiss Axio Observer Z1), and spheroid size was assessed manually with the freehand section tool in Fiji.

4.1.13 Cryosection staining and imaging

For cryo-embedding (IHC-Frz) of *in-vitro* vascularized AT, PFA-fixed organoids were exposed to sucrose gradients of first 10% and then 30% sucrose (Sigma Aldrich, S0389) in DPBS whereof each sucrose concentration incubated for 2h at RT on a shaker with 45 rpm. Then spheroids were stored in a 1:1 mix of cryo-embedding medium (OCT, Carl Roth, 6478.2) and 30% sucrose overnight at 4°C on a shaker with 45 rpm. After that, spheroids were embedded into OCT filled cryomolds on dry ice and stored until used at -80°C. Embedded organoids were sectioned on a cryotome (Leica) into 20 µm slices. The staining buffer and procedure were similar as for wholemount staining, except that first antibody incubation was reduced to overnight and secondary antibody incubation to 2h. Vectashield plus-mounted slides were sealed with a glass slide and nail polish before imaging at a confocal microscope with similar parameters as for whole-mount IF imaging.

4.1.14 Assessment of lipolysis and glucose uptake in vAOs and AOs

For parallel assessment of metabolic activity of organoids, lipolysis, and glucose uptake assay were combined into one set-up. For this, mature co-culture organoids from day 14 were washed once with Krebs-Ringer (KR)-buffer (Thermo Fisher Scientific, J67795.AP) and then incubated in 30 µL KR-buffer in an incubator at 37°C for 3h. Supernatants were removed and replaced by 30 µL KR-buffer supplemented with either insulin (0.2 mg/mL, Sigma, human-recombinant, I9278-5ML) or forskolin (10 µM, Abcam, ab120058) or left without treatment for untreated organoid controls as well as empty wells with media background controls and incubated at 37°C in an incubator for another 3h. Supernatants were removed and stored at 4°C until lipolysis. For glucose uptake assay, spheroids were fed with 1mM 2-Deoxyglucose (2-DG, from Promega Glucose Uptake-Glo Assay) for 10 min at RT. For negative/background control, 2-DG was omitted in duplicates. 2-DG was removed and 25 µL of Collagenase P-Accutase solution (1:1 mix, Collagenase P from Roche, 11213857001, prediluted at 18 UI/mL in DPBS) was added. After placing in the incubator for 30 min, spheroids were dissolved to single cell suspension by pipetting vigorously, first with a 100 µL tip, and later with a 10 µL tip. The cell suspension was transferred into white 96-well plates and the assay was performed according to the manufacturer's protocol (Glucose Uptake-Glo Assay, Promega, J1342). The assay volumes were adapted to lower volumes of single organoid format: standards, stop and neutralization buffer were used in a volume of only 25 µL. After an incubation time of 60 min at RT, luminescence was read with by a plate reader (Thermo Fisher) and internalized 2-DG concentration could be determined by a standard curve and was background-normalized to organoids without 2-DG uptake. In between, supernatants were used to assess secreted glycerol concentrations through lipolysis by a standardized glycerol assay kit (Sigma, MAK117-1KT) measuring a fluorometric signal. Also here, volumes were adapted, using 5 µL sample volume and 50 µL assay buffer per replicate. Dealing with small concentrations and volumes, exact volume distribution was achieved using multistep pipettes during all steps when medium or buffer was added to wells.

4.1.15 Sample preparation of cells from organoids

For RNA single-cell sequencing, cells were extracted incubating for 30 min in Accutase/Collagenase P mix at 37°C after two preceding washing steps in DPBS. Digestion reaction was stopped with DPBS + 10% FBS. Cells were centrifuged with

300 g for 3 min before resuspension in DPBS + 2% BSA. Cells were filtered with a 20 µm cell Pluristrainer (pluriSelect, 43-50020-023) and checked for viability of over 70% by TrypanBlue (0.4%, Sigma Aldrich 15250061) staining. For RNA single nuclei sequencing, a nuclei extraction protocol from Strzelecki M et al.[167] was adopted. The AG Martinez also kindly provided help and buffer for nuclei extraction protocol establishment. Organoids were distributed into portions of 25 organoids and transferred into 500 µL HB (homogenization buffer) in a glass cylinder. Organoids were ground 5 times with a Dounce tissue grinder (Th. Geyer, 9651617) of pestle size A and 20 times with pestle size B. As soon as organoids were disassembled, DPBS + 10% BSA was quickly added in the same volume. Nuclei suspension was filtered with a Flowmi filter (40 µm, Th. Geyer, 1183242) and centrifuged for 5 min, 200g. The pellet was resuspended in DPBS + 10% BSA and nuclei were counted with TrypanBlue. RNA libraries were generated according to the manufacturer's instructions for the Chromium Single Cell 3 library and gel bead kit v3.1 (10x Genomics, 1000269). The amplified cDNA libraries were sequenced on a NovaSeq SP flow cell from Illumina.

4.1.16 Pre-processing of scRNA-seq data

Raw sequencing data files were demultiplexed, aligned (reference genome hg38_ensrel96), filtered, barcodes and UMIs counted, and subjected to a quality filter with CellRanger (10xGenomics). After concatenation of the compared scRNAseq datasets (**Figure S2A and B**), cells with mitochondrial gene count of more than 15% were sorted out as well as cells expressing less than 1500 genes. Each considered gene had to be expressed in at least 3 cells. Gene counts were normalized to 10^4 per cell and the log was transformed. Due to high ribosomal count, next to cell cycle and mitochondrial also ribosomal genes were regressed out. Doublets were filtered out by DoubletDetection[168] tool. For single nuclei, RNA sequencing datasets of vascularized AT model quality parameters after the CellRanger procedure were adapted as follows considering lower counts of nuclei transcriptome (**Figure S2C and D**). Cells with high mitochondrial (above 5%) and high ribosomal (above 10%) counts were sorted out. Furthermore, only cells with maximum counts of $3*10^4$ and minimum gene count of 200 were filtered. Each gene had to be expressed in at least 3 cells. Also in this dataset, cell cycle, mitochondrial, and ribosomal genes were regressed out. Harmony[169] batch correction was applied to account for the vAO (50-50) condition being generated in another sequencing run.

4.1.17 Dimensionality reduction, cell clustering, and cell-type annotation

For the scRNA-seq dataset, the first 10 principal components with 10 neighbors were calculated for single-cell neighborhoods. Leiden resolution was set to 0.4, leading to 9 distinct clusters. For the snRNA-seq dataset, neighborhoods were assessed using the first 10 principal components with 8 neighbors. Leiden algorithm was set at resolution of 0.8 leading to 8 cell clusters. For both analysis, top ranked genes as assessed by t-test method were considered for cluster-to-cell type annotation according to literature research.

4.1.18 RNA velocity assessment

For velocity analysis, first, a splicing matrix was generated using velocyto[88]. After concatenating the splicing matrix with preprocessed scRNAseq datasets, cells were filtered (shared_counts=20, n_top_genes=2000) normalized, and logarithmized. Then, moments resulting from connectivity were calculated with 30 PCAs and 30 neighbors, and velocities presented as UMAP embedding streamlines according to the scVelo[87] standard pipeline.

4.1.19 Gene ontology enrichment, CellChat analysis, and donor identification

For enrichment analysis of GO (Gene ontology) terms, the Python implementation GSEAPy[170] was used, orientated on the author's example code for scRNAseq data analysis. Briefly, genes were ranked in their expression strength between two conditions. Then, only genes with a significance value of 0.05 (p-*val* adjusted) were considered for screening databases, like "WikiPathway_2023_Human"[171]. GSEAPy uses the enrichr[120] toolset for database screening. For querying gene/protein interaction database stringDB[172], a code for plotting GO-term results was used based on previously published xDBit_toolbox[173]. The cell-cell cumonication analysis was performed with CellChat[174]. Souporcell[175] tool was applied for donor identification of scRNAseq data.

4.2 Results

4.2.1 Engineering of vascularized adipose organoids

To bioengineer a 3D *in vitro* model of vWAT, patient-derived hASCs, and SC-ECs were co-cultured in a self-organizing collagen I hydrogel suspension at a concentration of 2,5 mg/mL. We used media conditions that favoured both adipogenesis and angiogenesis to differentiate adipocytes and promote vessel formation in the hydrogel culture. This was achieved by combining equal parts of each commonly used cell medium (**Figure 13A**). After 14 days, the cells caused the hydrogel cultures to contract, resulting in the formation of a spherical organoid with a diameter of approximately 500 µm, representing a 15-fold reduction from the organoid's initial diameter. Immunofluorescence imaging revealed an arborized vessel network and lipid droplet-containing adipocytes co-developed within the organoids (**Figure 13B**).

In the next step, we systematically screened the influence of media conditions and cell type ratios on the balance between vessel network formation and adipogenesis within vAOs. First, the cell type ratios between hASCs and SC-ECs at seeding were adjusted, while maintaining a constant 1:1 ratio of adipocyte differentiation medium (ADM) to endothelial cell growth medium (ECGM) (**Figure S1A**). As expected, increasing the percentage of SC-ECs within the vAOs from 10% to 50% led to an increase in total vessel network length, as evaluated from counterstained immunofluorescence images (**Figure 13C**).

To assess adipogenesis within the vAOs, we prepared reference organoids containing only hASCs and measured lipid droplet accumulation in ADM without SC-ECs. This control culture is referred to as adipocyte organoids (AOs). The degree of adipocyte maturation in all organoids was assessed by analysing the size distribution of lipid droplets. Lipid droplets within counterstained fluorescence images of each organoid type were categorized as small (<100 µm²), medium (<250 µm²), or large (>250 µm²). The number of large lipid droplets increased in vAOs with a higher SC-EC fraction (**Figure 13D**), indicating a positive microenvironmental effect of vascular structures on adipocyte maturation.

Next, vAOs with 20% SC-EC fraction were used as the preferred condition to test media composition by varying the ratio of ADM to ECGM (**Figure S1B**). As expected, the addition of only ADM led to adipocyte formation with the highest absolute lipid

accumulation in AOs (**Figure 13E**), but no vessel structures (**Figure 13F**). In vAOs the fluorescence image showed that an increasing ECGM ratio led to an increase in total vessel network length (**Figure 13F**), while the total number of lipid droplets decreased (**Figure 13E**). However, the proportion of larger lipid droplets increased with a higher ECGM ratio, which correlated with a more extensive vessel network structure (**Figure S1C**). In contrast, using only ECGM resulted in a high number of vessel structures but no adipocytes. This condition was termed vascularized stromal vascular fraction organoids (vSVFO). Both vessel architecture and adipocyte differentiation required their respective growth factor environments.

Interestingly, a higher vessel density resulted in stronger compression of the organoids in vAO (**Figure 13G**). Therefore, we tested also whether the collagen 1 concentration has an impact on organoid formation. Higher (5 mg/ml) and lower (1 mg/ml) collagen I hydrogel concentrations for the formation of the organoids resulted in either low cell survival rates or instability of the suspension organoid culture, respectively. The formation of vAOs in Matrigel was not possible, most likely due to the lack of matrix remodelling and compression of the hydrogel by the SC-ECs (**Figure S1D**). Representative immunofluorescent stained cryosections of vAOs and AOs are presented (**Figure 13H and I**). In summary, while the cell ratio for the formation of vAOs could be optimized at 20% SC-ECs and the ECM conditions at 2.5 mg/mL collagen I, the media composition requires further functional and transcriptional characterization of adipocytes and ECs.”

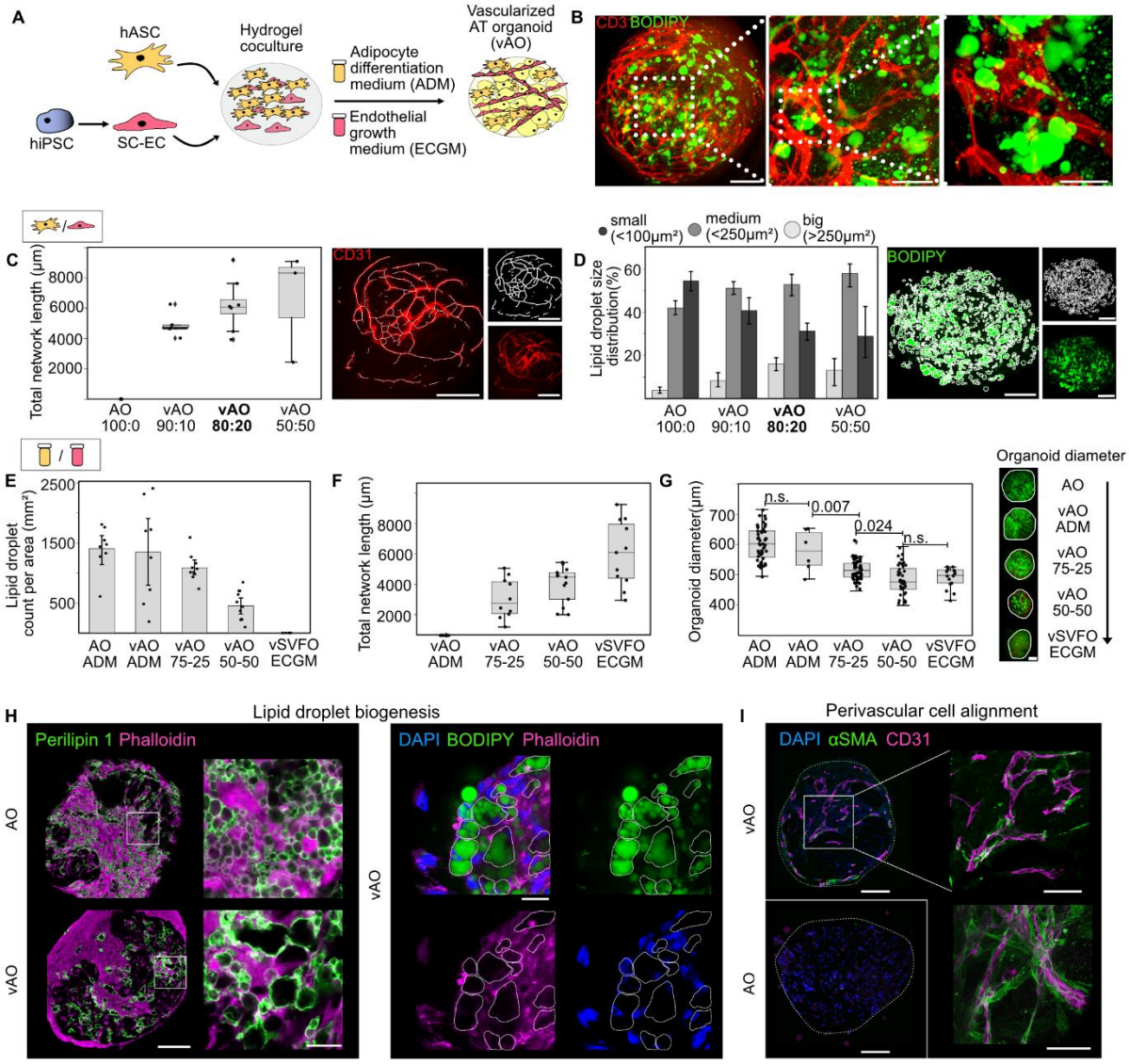

Figure 13 Engineered vascularized adipose organoids.

(A) Schematic of the in vitro cell culture model setup. (B) Representative confocal 3D projections of whole-mount vascularized adipose tissue organoids (vAOs) on day 14, stained for lipid droplets (BODIPY) and endothelial marker (CD31) (scale bars: 100 µm, 30 µm, 10 µm). (C) Sprouting network analysis based on CD31-stained confocal 3D image projections. Adipose organoids (AO) composed of 100% hASCs, whereas vAOs composed of hASCs and 10% (90:10), 20% (80:20), or 50% (50:50) SC-ECs. Images display 3D projections of CD31 staining, overlaid with segmented vessels (n>=3-8 from 1-3 independent experiments). (D) Lipid droplet size distribution across different cell ratios, categorized as small (<100 µm²), medium (<250 µm²), or large (>250 µm²) droplets (n ≥ 3–9 from 1–4 independent experiments). Images represent 3D projections of BODIPY-stained confocal images of a vAO (50% ADM/50% ECGM), overlaid with segmented lipid droplet outlines (n ≥ 4–12 from 2–5 independent experiments). (E) Bar graph shows the number of lipid droplets per organoid cross sectional area in different media conditions with either 100 % adipocyte differentiation medium ADM (ADM) or increasing proportions of endothelial growth medium (ECGM) as 25% (vAO 75-25) or 50% (vAOs 50-50). Undifferentiated vSVFOs was treated with 100% ECGM (n>=6-20 from 2-5 independent experiments). (F) Boxplot shows total vascular network length across different media conditions. (n>=8-15 from 3-5 independent experiments). (G) Organoid

size analysis under different media and cell conditions (n ≥ 6–20 from 2–4 independent experiments). Representative confocal 3D projections of BODIPY and CD31-stained images are shown. Boxplots shows the organoid diameters. P-values were calculated using one-way ANOVA followed by Tukey's multiple comparison test. All error bars represent 95% confidence intervals (scale bar: 100 µm). (H) Immunofluorescence image of cryosectioned AOs and vAOs stained for the lipid-droplet protein Perilipin 1 and the actin cytoskeleton. (scale bar left 100 µm, right 25 µm). (I) Perivascular cell alignment around endothelial cells. Immunofluorescence images show endothelial cell marker CD31 and pericyte marker αSMA in AOs and vAOs, respectively. Upper images: vAOs (scale bars: 100 µm, 50 µm). Lower left: AO (scale bar: 100 µm). Lower right: Whole-mount z-projection of a vAOs (scale bar: 50 µm).

4.2.2 Functional characterization of vascularized adipose organoids

One hallmark of adipose tissue is the induction of lipolysis under fasting conditions and glucose uptake upon insulin stimulation[43]. *In vitro* catecholamines can trigger lipolysis via the b-adrenergic receptor pathway or be indirectly activated downstream by forskolin. In the feeding state, insulin-mediated pathways dominate adipocyte function leading to increased translocation of insulin-sensitive glucose transporter GLUT4 to the cell membrane followed by glucose uptake and lipogenesis while inhibiting lipolysis[43]. In this respect, we tested the lipolysis response of AOs, vSFOs, and vAOs upon forskolin stimulation. Forskolin treatment was performed over a time frame of 3h. To account for the different sizes, architectures, and cell compositions of the organoids, the accumulation of free glycerol was normalized to the group mean of untreated organoids per condition. All organoids, except for vSVFOs, showed a significant increase in free glycerol secretion after forskolin stimulation (**Figure 14A**), arguing for a functional lipolysis response. vAO cultured in 75/25 ADM/ECGM media ratio showed a stronger response than AOs. The vSVFOs with undifferentiated hASC showed no significant increase in free glycerol secretion after forskolin stimulation.

Next, we tested if the glucose uptake after insulin treatment is altered in vAOs compared to AOs. For this, we used a bioluminescent 2-Deoxy-D-glucose-uptake assay. All organoid cultures showed an increase of 2-Deoxy-D-glucose uptake after insulin stimulation compared to their untreated control condition (**Figure 14B**). Baseline glucose as well as post-insulin treatment concentrations were significantly higher in vAOs with 25% ECGM fraction compared to vSVFOs but also higher than in AOs. To interrogate this finding, we immunofluorescent stained for GLUT4 transporter (**Figure 14C**). Here, αSMA-positive perivascular mural cells in vAOs exhibited strong GLUT4 expression, suggesting that vessel formation induces transcriptional changes

in cells within the stromal vascular niche cells. Thus stromal vascular niche changed but potentially also the adipocyte function through a signaling axis [176]. In summary, vAOs and AOs both depicted adipocyte-specific metabolic function, but vAOs at a media ratio of 75/25 (ADM/ECGM) were more prone to react to ß-adrenergic lipolysis stimulation and were upregulated in basal and insulin-induced glucose uptake.

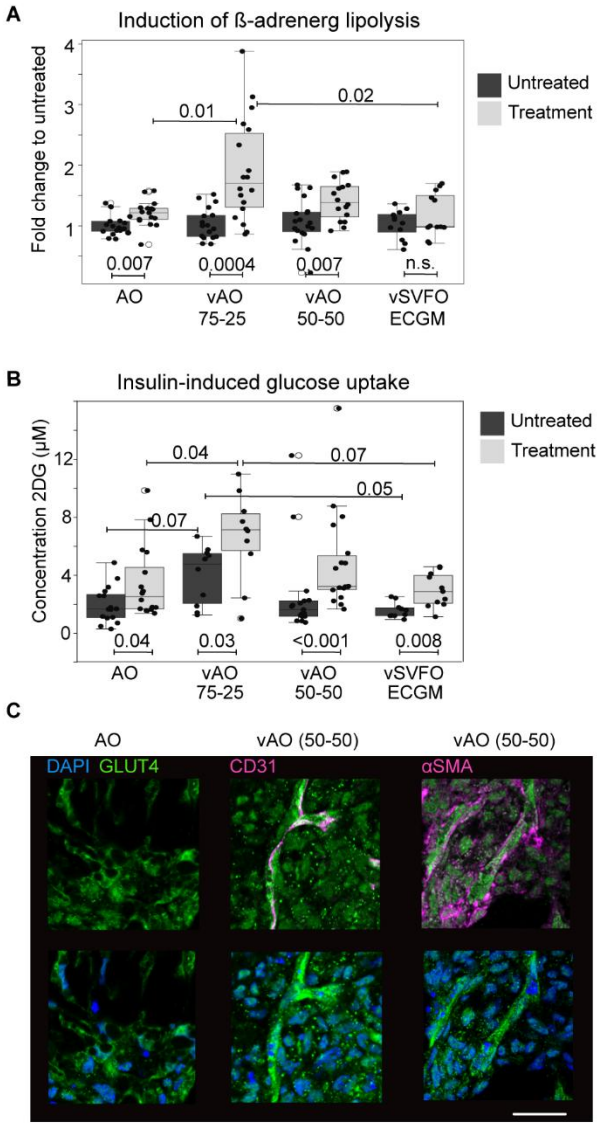

Figure 14 Functional characterization of vascularized adipose organoids

(A) Forskolin-induced lipolysis assay. Organoids were treated with 10 µM forskolin for 3h. Glycerol concentrations were assessed from supernatants and normalized treated to untreated controls (n=12-17 from 3-5 independent experiments). Pairwise Welch tests (for comparisons within individual groups) and groupwise Welch-ANOVA test (to assess overall group differences) were performed for statistical analysis. (B) Insulin-stimulated glucose uptake. Box plots show internalized 2DG (2-desoxy-glucose) concentrations of untreated and insulin (3h, 0.2 mg/mL insulin) treated organoids. n=10-17 from 3-5 independent experiments. Wilcoxon rank sum test (for pairwise comparisons) and Wilcoxon-ANOVA with Dunn's post-hoc test (for multiple group comparisons) were performed for statistical analysis. (C) Cryosections of AOs

and vAOs (50-50 model) stained for nucleus (DAPI), glucose uptake transporter GLUT4, endothelial (CD31) and SMC marker (αSMA). Scale bar: 50 µm.

4.2.3 Charting adipocytes within vAO by single-nucleus RNA sequencing

To assess the adipocyte subtypes and maturation under adipogenic conditions within different organoids, we employed single-nucleus RNA sequencing (snRNA-seq) on AOs and vAOs cultured under 75/25 and 50/50 ADM/ECGM media ratio. The snRNA-seq method was selected to ensure an unbiased representation of all cell populations, particularly to prevent the exclusion of buoyant pre-adipocytes and mature adipocytes during cell preparation. After stringent quality filtering (**Figure S2C and D**), 6,585 nuclei were analysed, with expression data spanning 22k genes. The resulting data were visualized using UMAP (**Figure 15A, B**).

Leiden clustering identified eight distinct clusters (**Figure 15C, D**). Annotation of these clusters was performed based on differential gene expression profiles and known marker genes (**Figure 15D**). Two adipocyte clusters (AD1 and AD2) were detected in the snRNA-seq data, characterized by the expression of late-stage adipogenesis markers, including *ADIPOQ*[43], *FABP4*[43], and *SCD*[177]. Additionally, three preadipocyte (PA) clusters were identified. These clusters expressed perivascular adipocyte-associated genes, such as *MGP*[178] and *DCN*[179]. Among PA subtypes, PA1 exhibited higher expression of *CD81* and *PPARγ*, markers associated with committed beige preadipocytes[180]. These markers exhibited a progressive decline in expression level as cells matured. The fraction of thermogenic PA1 cells increased with vessel density, suggesting an interaction between angiogenesis and preadipocyte thermogenic programming that was also reported in mice[181]. However, mature adipocytes in all organoid culture conditions lost CD81 expression. In line with the PA transcriptional cell profile we found a mural cell (mural) cluster expressing *TAGLN*[182], *ACTA2*[182], and the thermogenic gene *CYCS*[181]. This is consistent with a recently characterized mural cell population in perivascular adipose tissue (PVAT) that exhibits thermogenic adipocyte differentiation potential in mice[19] (**Figure 15D**). Considering overlapping gene expression of ASC-related genes for lipid handling (*ENO1*[183] *and FLNA*[184,183]*, ANXA2*[185]) in mural cells argues for SMC development from the ASC cluster. Velocity pseudotime[88] analysis (**Figure 15E**) confirmed the development of premature PA towards adipocytes. Although the PA3 cluster lacked preadipocyte- or adipocyte-

specific gene expression, pseudotime analysis suggested that all assigned PA cluster represent a precursor stage to the more mature AD stage.

As expected, AOs cultured in an adipogenic medium only exhibited the highest proportion of adipocytes (**Figure 15F**), consistent with our findings from fluorescence imaging. In contrast, increasing the fraction of endothelial cells, along with culturing in angiogenic media in vAOs, resulted in a gradual reduction in adipocyte content. This was accompanied by an increase in PA clusters, characterized by high *CD81*[180] expression, indicating the beige and thermogenic properties of vAOs in the context of enhanced vascularization. Gene Ontology (GO) term analysis[171] (**Figure 15G**) and KEGG[186] pathway analysis (**Figure 15H**), based on gene expression profiles of these clusters, supported the maturation observed in the pseudotime projection. During vAO maturation, and as expected, PPARγ signaling, and fatty acid biosynthesis pathways were enriched along the pseudotime toward adipocytes. Interestingly, this was coupled to the downregulation of the PI3K-Akt signaling pathway. The most enriched GO term in vAOs was related to extracellular matrix organization, aligning with the observed reduction in vAO diameter as vessel structures formed, and depicted in **Figure 13G**.

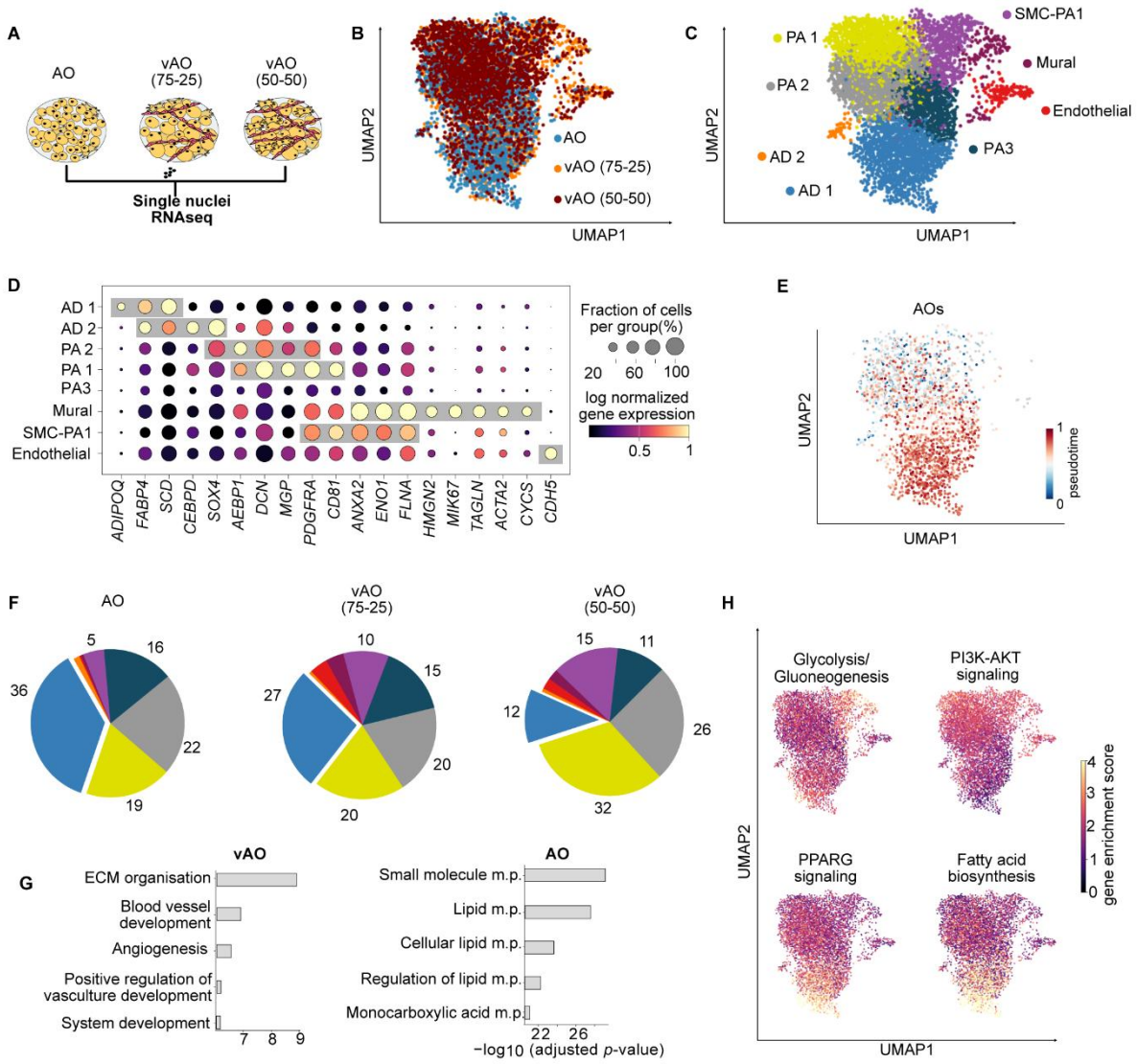

Figure 15 Single nuclei RNA-sequencing to chart adipocytes in vAOs.

(A) Experimental overview: Single nuclei of extracted from AOs and vAOs with a SC-EC ratio of 25 and 50% were subjected to single nuclei RNA-sequencing (snRNA-seq).(B) UMAP representation of single nuclei transcriptomes from the combined dataset of the three organoid types. (C) Clusters were annotated to the corresponding cell types through marker gene profiling. (D) Dot plot shows the gene expression levels of representative markers for each cell cluster. (E) Velocity pseudotime analysis[88] indicating the transient development of the found cell states. (F) Cell type distribution within the different organoids. (G) GO-term analysis[120] for top differentially expressed genes in each cell cluster. Adjusted p-values (-log10 transformed) are presented as a bar plot for each GO-term. (H) KEGG pathway[186] gene enrichment plotted as UMAP.

4.2.4 Charting cell types of the stromal vascular bed in vAOs

To characterize the cell type composition and transcriptional states of preadipocytes, stromal cells (ASC), and endothelial cells during vessel formation and adipocyte

maturation, we performed single-cell transcriptome (scRNAseq) analysis of vAO cultured under a media ratio of 50% ADM/ECGM media ratio and used for comparison vSVFOs cultured in ECGM medium (**Figure 16A**). After stringent filtering (**Figure S2A and B**), 15,000 cells with 23k genes were analyzed and visualized using UMAP (**Figure 16B**). Leiden[113] clustering of the whole data sets identified 10 distinct cell clusters (**Figure 16C**). Again, the annotation of these clusters was performed based on differential gene expression profiles and known marker genes (**Figure 16D**). Mural cell, PA and EC cluster were consistent with those found in the above snRNA-seq analysis. All clusters, except for ECs and ASC1 were positive for *PDGFRA* (PGDFRα). PDGFRα-positive progenitors are known to be located in the perivascular niche in adipose tissue having the potential to develop into mural cells and into the osteogenic or adipogenic cell lineages[187]. In the undifferentiated vAOs, we identified two fibro-adipogenic progenitor (FAP) clusters, a mural cell cluster, fibroblasts, mesenchymal stromal cells (MSCs), and an EC cluster. Both FAP clusters were distinguished by the expression of transcription factors such as *SOX4*[188] and adipocyte enhancer-binding protein 1 (*AEBP1*)[189]. FAP cells were still uncommitted toward the adipogenic or the osteogenic lineage but expressed some osteogenic differentiation genes *AEBP1*[189], *CTSB*[190], and *CTSL*[191], *LTBP1*[192], or early adipocyte-differentiation marker *LMO4*[193]. Fibroblasts were marked by expression of *POSTN*[194], *VCAN*[195], and *BGN*[195].

ASC, mural cells and ECs were overlapping in both conditions. Mural cells expressed the marker genes ACTA2[182] and PDGFRβ[182], and the hASC-to-mural cell trans-differentiation marker *IFGFBP7*[196]. The mural cell fraction combines smooth muscle but also pericytes (see marker expression panel in **Figure S3**). While ASCs predominantly expressed the stemness marker *HMGN2*[197] and galectin *LGALS1*[198], ECs uniquely expressed *CDH5*. Additionally, ASC possessed an expression profile consistent with lipid processing, e.g. expression of *ANXA2*[185], involved in trans-endothelial fatty acid transport in AT. *ENO1* and *FLNA* had been indicated in weight gain[184] and adipocyte hypertrophy[183].

In the vAOs, we found predominantly three cell clusters with gene expression profiles PA clusters of the snRNA-seq data. PA clusters were defined by the expression of committed preadipocyte markers *APOD*[199], *CFD*[199], and *CEBPD* (C/EBPδ)[43].The higher gene depth of the scRNA-seq technology revealed in accordance to the snRNA-seq data that, PA1 cells highly expressed CD81. Furthermore, PA2 cells revealed a high

MGP expression, a marker for brown adipogenesis in mice[200], while also being expressed significantly higher in perivascular than in subcutaneous ASC in mice[178]. Additionally, PA2 and PA1 cells showed high decorin (*DCN*) expression, a collagen assembly protein. *DCN* was shown to be abundantly expressed in stromal or vascular cells in AT *in-vivo*, especially those near vessels[179].

ECs within vessel in all organoids developed only from the stem-cell derived ECs and not from cells of the stromal vascular fraction as the genotype analysis[175] could show (**Figure 16E**). Next, we resolved cell state trajectories using velocity analysis for each organoid type. As expected, within the vSVFOs the velocity lines pointed from ASC2 cells towards FAPs and mural cells. Similarly, in vAOs, the velocity vector lines directed ASCs towards the PAs (**Figure 16F**). To further corroborate these annotations, a combined GO-term[171] analysis was performed using the differentially expressed genes (DEGs) for comparing the two organoid types (**Figure 16G**). While the obtained GO terms for cell clusters of the vAOs related to adipo- and angiogenesis and included focal adhesions, GO terms for cell clusters of vSVFOs related rather to fibrotic tissue. Gene expression levels, which defined the most pronounced GO terms are summarized in **Figure 16H**.

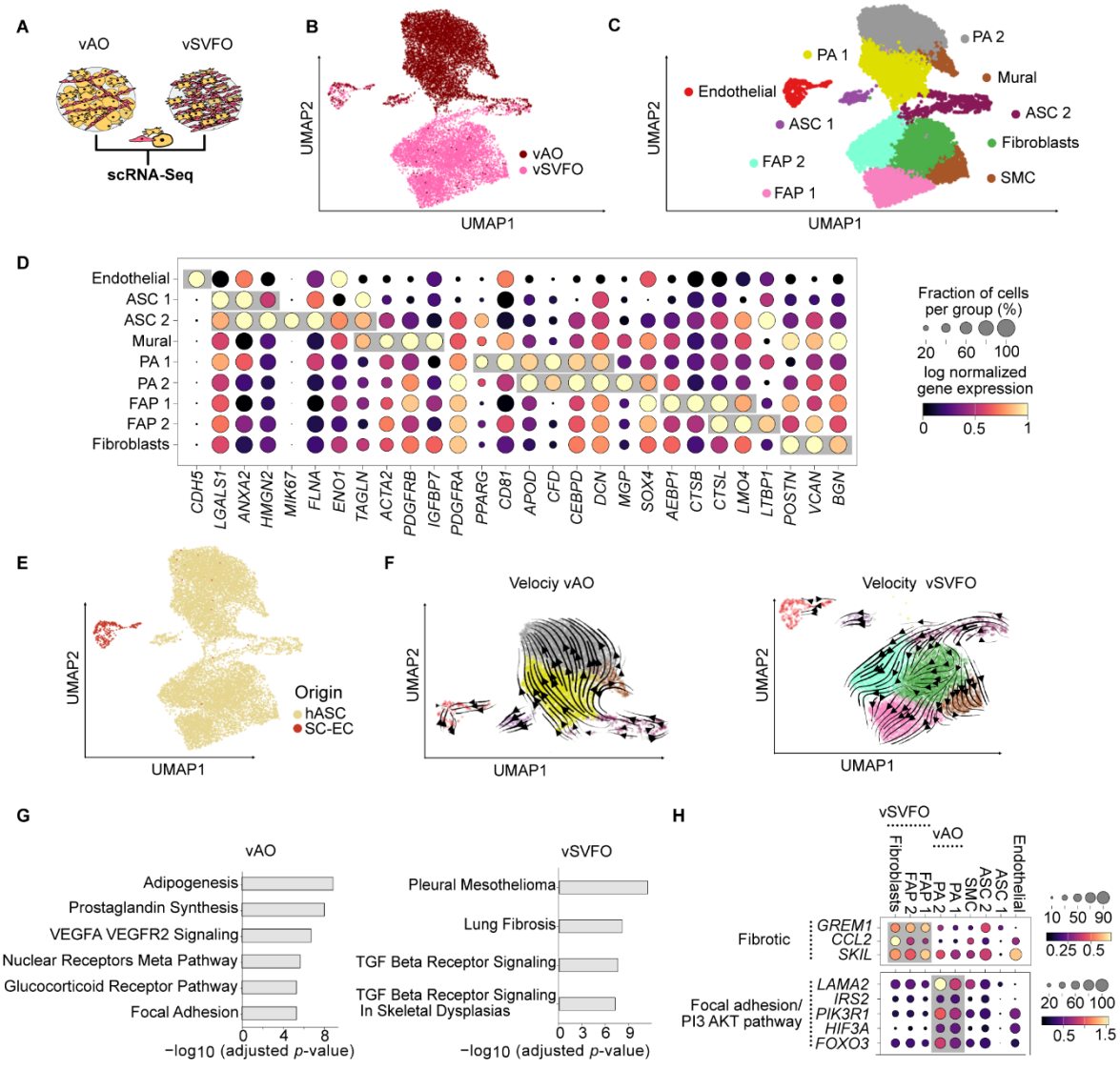

Figure 16 Single cell RNA-sequencing reveals distinct cell states during adipogenesis in vascularized adipose organoids.

(A) Experimental overview: Single cells extracted from vAOs and vSVFOs with a SC-EC ratio of 50% were subjected to scRNA sequencing (scRNAseq). (B) UMAP representation of sc-transcriptomes from the combined dataset of both conditions. (C) Leiden-defined clusters were annotated to the corresponding cell types through marker gene profiling. (D) Dot plot shows the gene expression levels of representative markers for each cell cluster. (E) UMAP depicts the genotypic origin of the hASC and SC-EC seeded in organoids. (F) Velocity vectors indicating the transient development of the found cell states. (G) GO-term analysis for top differentially expressed genes in each cell cluster. Adjusted p-values (-log10 transformed) are presented as a bar plot for each GO-term. (H) Dot plot showing gene expression levels of selected genes from the GO-term analysis.

4.2.5 Maturing of stem cell-derived ECs in vAO

As a next step, we explored the transcriptional state of SC-ECs within vAOs and vSVFOs. Endothelial cells from the scRNAseq dataset (**Figure 16**) were isolated and clustered separately (**Figure 17A**). Using the Leiden[113] algorithm, the scRNAseq data was grouped into two clusters, designated maturing and respirating SC-ECs. Both organoid types contained SC-ECs from each cluster but with differing proportions. In the vAOs, the fraction of matured SC-ECs increased markedly compared to the vSVFOs. Among the top DEGs in the matured SC-ECs cluster were genes associated with vessel maturation, such as *MECOM*[123], and *VASH1*[201] (**Figure 17B**). GO term analysis of the differentially expressed genes in this cluster revealed enrichments related to blood vessel and tube morphogenesis (**Figure 17F**). In contrast, the respirating SC-EC cluster was enriched for GO terms related to mitochondrial respiratory chain pathways, with high expression of genes like *NDUFB4*[202], a component of the respiratory chain, and *NQO1*[203], which is involved in oxidative stress response (**Figure 17C**). Given the increased energy demands during angiogenesis to support endothelial cell proliferation and migration, these findings suggest that these ECs are more metabolically active in terms of oxidative phosphorylation. Next, we explored whether the maturation of SC-ECs in vAOs mirrored a transcriptomic phenotype observed in humans *in vivo*. To address this, we calculated gene enrichment scores of the DEGs obtained from single-cell datasets of adult human adipose tissue[199], and compared them with our single-cell transcriptomic data (**Figure 17E**). Notably, the gene enrichment score for microvasculature within adipose tissue increased significantly compared to venous and arteries, which is supported by the images depicted in **Fig 13**. Further, ECs in both vAOs and vSVFOs showed the expression of marker genes known to be enriched in adipose tissue, including *FABP5* and *TCF15* (**Figure 17D**), indicating that the SVF is sufficient to tone ECs towards adipose tissue.[204]

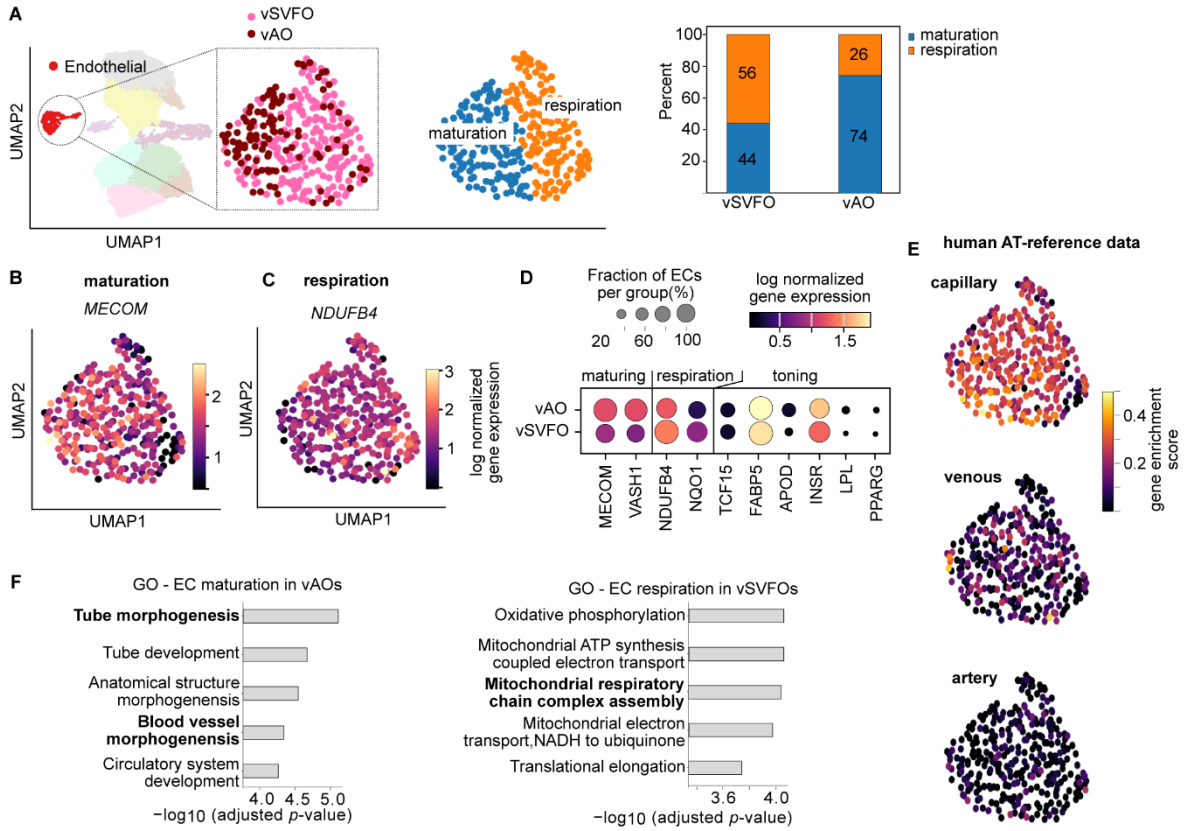

Figure 17 Maturing of SC-EC in vascularized adipose organoids.

(A) Single-cell transcriptomes of stem cell-derived endothelial cells within vAO and vSVFO were analyzed, revealing two subclusters with distinct gene profiles: one representing maturing cells and the other representing respiring cells, each with unique distributions between the two models. (B and C) UMAP plots showing representative marker expression levels for the two endothelial cell clusters. (D) Dot plot of representative maturing, respirating and adipose tissue toning markers for the EC in vAOs and vSVFOs.[204] (E) Enrichment score of differentially expressed genes (DEGs) from mature human adipose tissue capillaries, veins, and arteries within the vAOs[199]. (F) GO-term analysis based on the top-ranked genes for endothelial cell cluster in vAOs and vSVFOs.

To investigate the cell-cell communication leading to the maturation of SC-ECs in differentiated vAOs, we performed a receptor-ligand interaction[174] analysis on the scRNAseq dataset. This analysis showed that the strongest bidirectional signalling network within the vAOs occurred between endothelial cells and the cells of the stromal bed, as represented by the size of the sending and receiving signalling vectors in **Figure 18A**. A comparative analysis of the signalling pathways in SC-ECs from vAOs and vSVFO showed distinct interaction profiles (**Figure 18B**). In vAOs, ECs expressed key genes known from interactions with stromal bed cells involved in vascular development, including nectins and nectin-like (CADM) proteins[205], UNC5[206] signalling for vessel maturation, and PDGF[207,208] signalling between pericytes from the mural cell

cluster and EC. In contrast, ECs in vSVFOs exhibited stronger gene expression profiles for paracrine signals related to fibro-remodelling pathways, such as TGFβ[209] and Periostin[194] signalling. Thus, the dominant changes in cell-cell communication between vSVFOs and vAOs are centered around the pericyte-EC signaling axis, with vAOs emphasizing vascular development and stabilization processes through pericyte recruitment mediated by PDGF signaling, while vSVFOs interactions reflect a fibro-remodeling signature driven by TGF-β[209] signaling. These findings suggest that the maturation and specialization of SC-ECs are driven by distinct stromal microenvironments.

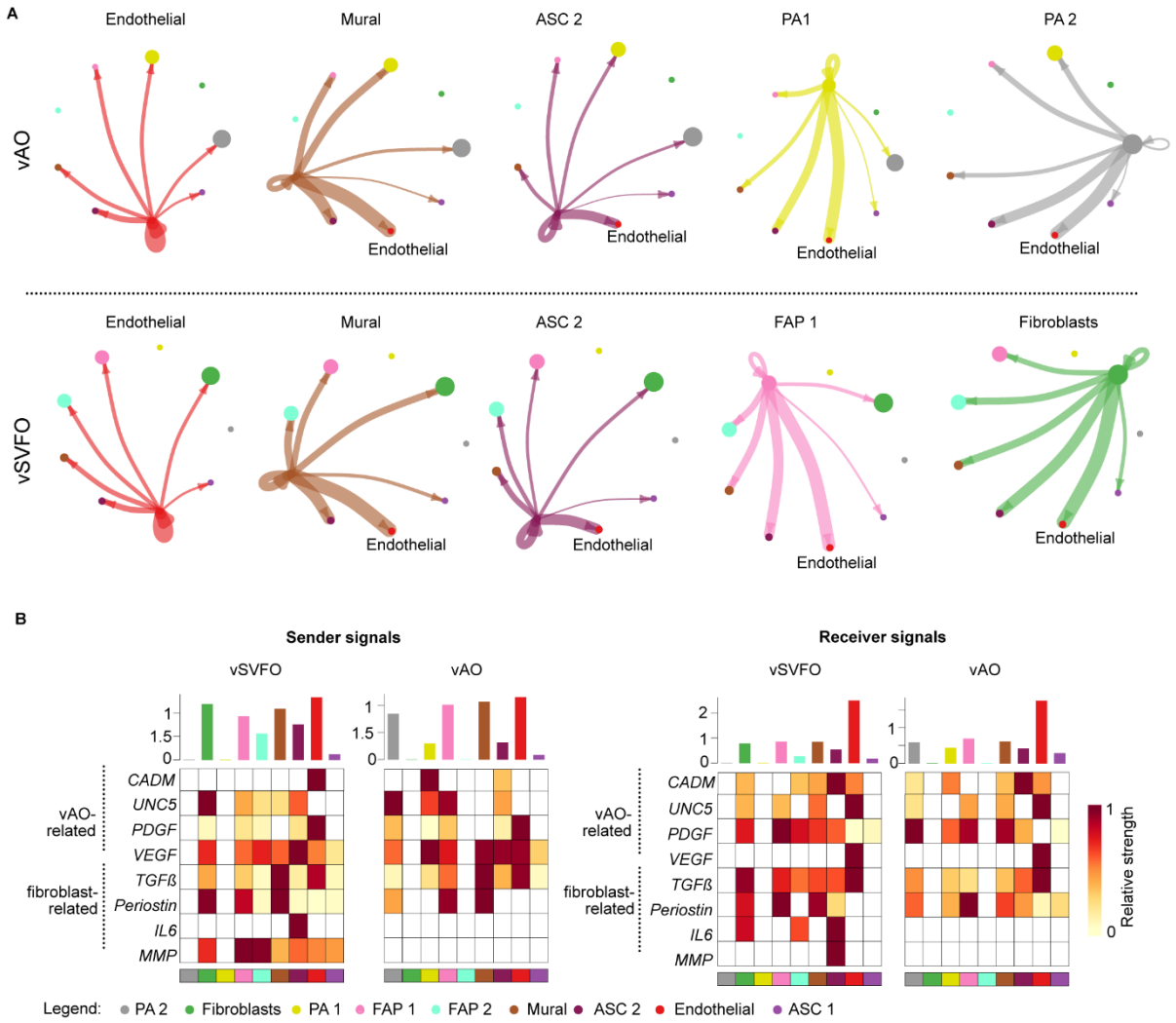

Figure 18 Cell-cell communication analysis within vAO based on receptor-ligand expression.

(A) Signaling patterns in vAOs and vSVFO were analyzed by profiling receptor-ligand interactions within the single-cell RNA datasets. The first plot on the left shows endothelial cells (ECs) sending signaling activity to all other cell types. The subsequent plots show ECs receiving signaling activity from the respective cell types in vAOs and vSVFO. (B) Heatmaps depicting the relative signaling activity of sending and receiving patterns for selected signaling

pathways. Both vAOs and vSVFO exhibited paracrine signaling between cell types, particularly related to fibroblast/ECM remodeling and angiogenesis.

4.2.6 Endothelial-Specific Knockdown of PDGFB Leads to Impaired Lipolysis in Adipocytes and Reduced Perivascular Cell Alignment

In the final step, we tested the hypothesis that only mature vessel structures with recruited pericytes within the vAOs contribute to the increased metabolic responsiveness of the adipocytes. To investigate this, we generated a lentiviral-mediated knockdown model for the *PDGFB* gene in the hiPSCs used to differentiate SC-ECs (**Figure 19A**). PDGFB is essential for recruiting pericytes from the stromal vascular fraction to vessels and establishing tight barrier function[207,208]. Therefore, hiPSCs were transduced with lentiviruses to induce a targeted knockdown of *PDGFB*, or a scrambled control vector for comparison. The successful knockdown was confirmed by quantitative PCR (**Figure S4A-D**). These hiPSCs were then differentiated into SC-ECs (PDFGB-KD) and sorted by flow cytometry based on CD31 expression (**Figure S4B-D**). Knockdown SC-ECs were subsequently used to form vAOs with a 25% ratio of SC-ECs (PDGF-KD) to hASCs.

Despite the *PDGFB* knockdown, the vessel density and branching network within the vAOs remained unaffected as well as the lipid droplet content (**Figure S4E**). However, the number of αSMA-positive cells surrounding CD31-positive cells in vessel structure areas was markedly reduced in the vAOs with the knockdown, as shown by immunofluorescence staining (**Figure 19B**). Strikingly, the lipolysis assay performed on vAOs containing SC-ECs with *PDGFB* knockdown revealed a significantly reduced sensitivity to forskolin treatment, compared to the scrambled control (**Figure 19C)**. These findings suggest that mature vessel structures with intact EC-pericyte interactions are an essential prerequisite for effective metabolic responses in the adjacent adipocyte tissue.

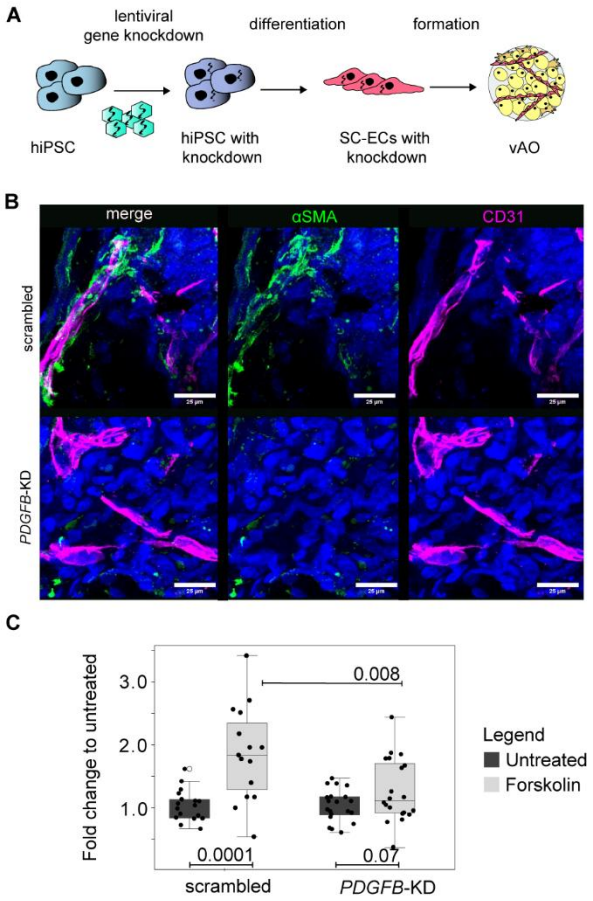

Figure 19 Knockdown of PDGFB expression in SC-EC impairs lipolysis in vascularized adipose organoids.

(A) Schematic of the knockdown strategy in vAO. hiPSC were transduced with lentiviral vectors to induce shRNA-mediated knockdown of the target gene. After differentiation, SC-EC with knockdown were used to form vAOs. (B) Confocal images of histological sections from scrambled and PDGFB-KD vAOs depicting reduced perivascular alignment of αSMA positive cells around CD31 positive endothelial cells within the knockdown condition. Scale bar: 25 µm. (C) Forskolin-stimulated lipolysis in vAOs with and without PDGF knockdown (N=4, n≥13). Statistical analysis was performed by Wilcoxon rank sum test. Error bars indicate 95% confidence level.

4.3 Discussion

To study the longitudinal physiology of WAT under controlled metabolic conditions, robust *in vitro* culture systems are required to replicate the essential architecture and functions of WAT[67].

For a deeper understanding of obesity in humans, vascularized functional adipocytes are an urgent need, as they facilitate molecular investigations into the roles of endothelial cells in nutrient uptake, metabolic exchange, and tissue remodeling among others during WAT expansion[53]. A well-vascularized WAT model is also critical to accurately model insulin resistance and metabolic dysfunction during diabetes progression. Despite advancements in organoid culture systems, models that integrate human stem cell-derived endothelial cells into human-derived WAT have not yet been reported. Such models also pave the way for the exploration of genetic predispositions or epigenetic adaptations to metabolic stress.

Vascularized AOs have previously been developed using microvascular fragments and SVF from mouse tissue, with the enhanced functionality of the cell culture system being observed only after transplantation[79,210]. Studies involving human-derived SVF, which includes endogenous ECs, have demonstrated the potential for vAO formation[78,79]. However, the functional capabilities, applications, and detailed cell type composition of these organoids remain unclear.

In this study, we developed a vAO model using hiPSCs, enabling simultaneous adipogenesis and angiogenesis within a 3D culture system. By systematically optimizing media compositions, we achieved stable populations of SC-ECs and adipocytes within organoid culture format, overcoming a common limitation in complex tissue models. Within the self-assembling organoid culture, vessel density increased with media that favour angiogenesis, while adipocyte formation was enhanced in media optimized for adipogenesis. Importantly, intermediate media conditions supported efficient co-development of both cell types while maintaining functionally relevant spatial organization, with vessels traversing the organoid structure. With this, the engineered cell culture system surpasses a simple adipose spheroids cluster. Notably, vAOs cultured with partial ECGM supplementation exhibited reduced adipocyte density compared to AOs while increasing adipocyte lipid droplet size. In contrast, vAOs cultured in a 75:25 ratio of adipogenesis-to-angiogenesis media exhibited enhanced β-adrenergic-induced lipolysis and increased glucose uptake, both

basal and insulin-stimulated, surpassing the additive effects observed in the respective monocultures. Further, the increased GLUT4 expression in SMCs in vAOs suggests that functional changes extended beyond adipocytes and SC-ECs.These findings highlight that our co-culture system provides a supportive microenvironment, that promotes adipocyte maturation and functionality while integrating vascular networks.

Single-cell sequencing analysis revealed that in vAOs committed PAs formed, whereas in vSVFOs lacking adipogenesis induction included FAPs that retained osteogenic marker expression, reflecting an uncommitted progenitor state with adipogenic and osteogenic potential. Overall, the observed cell transcriptomes of the vascular niche within the organoids reflected the cell type compositions of the *in vivo* WAT[165]. The adipocyte fractions were highest in AOs and progressively decreased as endothelial growth media supplementation increased. While Adipocytes expressed classical WAT markers, PAs developed specific genetic signatures of perivascular fat depots[178,179]. Classical beige adipocyte markers like e.g. *CIDEA* and *UCP1* were not detected, however PAs showed *CD81* which is linked to beige adipocyte formation upon cold exposure. The fraction of *CD81* positive cells in the vAOs correlated with increased adipogenic potential *in vitro*[180]. Despite this, the transcriptional thermogenic profile of vAOs, characterized by their complex mixture of cell types, aligned with their functional phenotype, especially their increased sensitivity to β-adrenergic-induced lipolysis. This interaction could be leveraged to design organoids with enhanced metabolic activity and responsiveness. Moreover, while mature adipocytes lacked classical beige markers, the transcriptional thermogenic profile and heightened β-adrenergic sensitivity in vAOs suggest a functional adaptation that mimics native tissue physiology.

Further transcriptomic analysis revealed that SC-ECs, regardless of the organoid type, developed capillary-like profiles with adipose tone, consistent with characteristic gene signatures from human datasets. Transcriptomic genotyping confirmed that ECs remained lineage-stable, with no transition into SVF cell types or vice versa, even under adipogenic culture conditions. The lineage stability of ECs, even under adipogenic conditions, ensures that the vascular component of the organoid retains its capillary-like characteristics, which are essential for mimicking the native tissue's nutrient and oxygen delivery functions. SC-ECs within vAOs exhibited a more mature profile compared to those in vSVFOs, as evidenced by differential gene expression analysis. However, the expression of adipocyte-specific EC markers was low, arguing

that SC-ECs did not acquire adipose-specific toning[199]. Conversely, SC-ECs in vSVFOs expressed genes associated with respiratory function. Given the strong influence of the local metabolic environment on ECs, the surrounding cells in vSVFOs clearly promoted distinct metabolic reprogramming during maturation of ECs, as evidenced by GO term analysis of their transcriptomes.

Our receptor-ligand interaction analysis revealed enhanced *PDGF*[207] and *UNC5*[206] signaling in vAOs, potentially contributing to the maturation of endothelial cells (ECs) in these organoids. *UNC5B* emerged as one of the top DEGs in vAO EC subsets, highlighting its role in vessel-adipocyte attraction signals in vAOs. *PDGF* signaling is a well-established pathway for vascular maturation, primarily through the recruitment of perivascular cells to the vessel wall[207,208]. Using our vAO model system, we generated an endothelial-specific knockdown of *PDGFB*, which impaired perivascular alignment, as evidenced by immunofluorescence staining, while leaving endothelial network formation unaffected. This disruption also hindered forskolin-stimulated adipocyte lipolysis, showing that *PDGFB*-mediated EC-pericyte interactions are critical for adipocyte function and stimulus response within a maturing vascular network. These findings are consistent with existing evidence that EC-derived signals regulate essential adipocyte functions, including insulin sensitivity, glucose uptake, and lipid homeostasis[53,54]. Thus, we demonstrated that vAOs are valuable tools for dissecting complex cellular interactions within a physiologically *relevant in vitro* microenvironment.

In summary, our study establishes a novel and robust vascularized adipocyte organoid model, enabling the simultaneous investigation of adipogenesis and angiogenesis under controlled conditions. This versatile platform provides new insights into endothelial-adipocyte crosstalk, uncovering mechanisms of cellular interaction, metabolic regulation, and adipose tissue remodeling. Furthermore, the model supports the exploration of metabolic signaling in obesity and diabetes, addressing urgent needs for innovative early detection and prevention strategies.

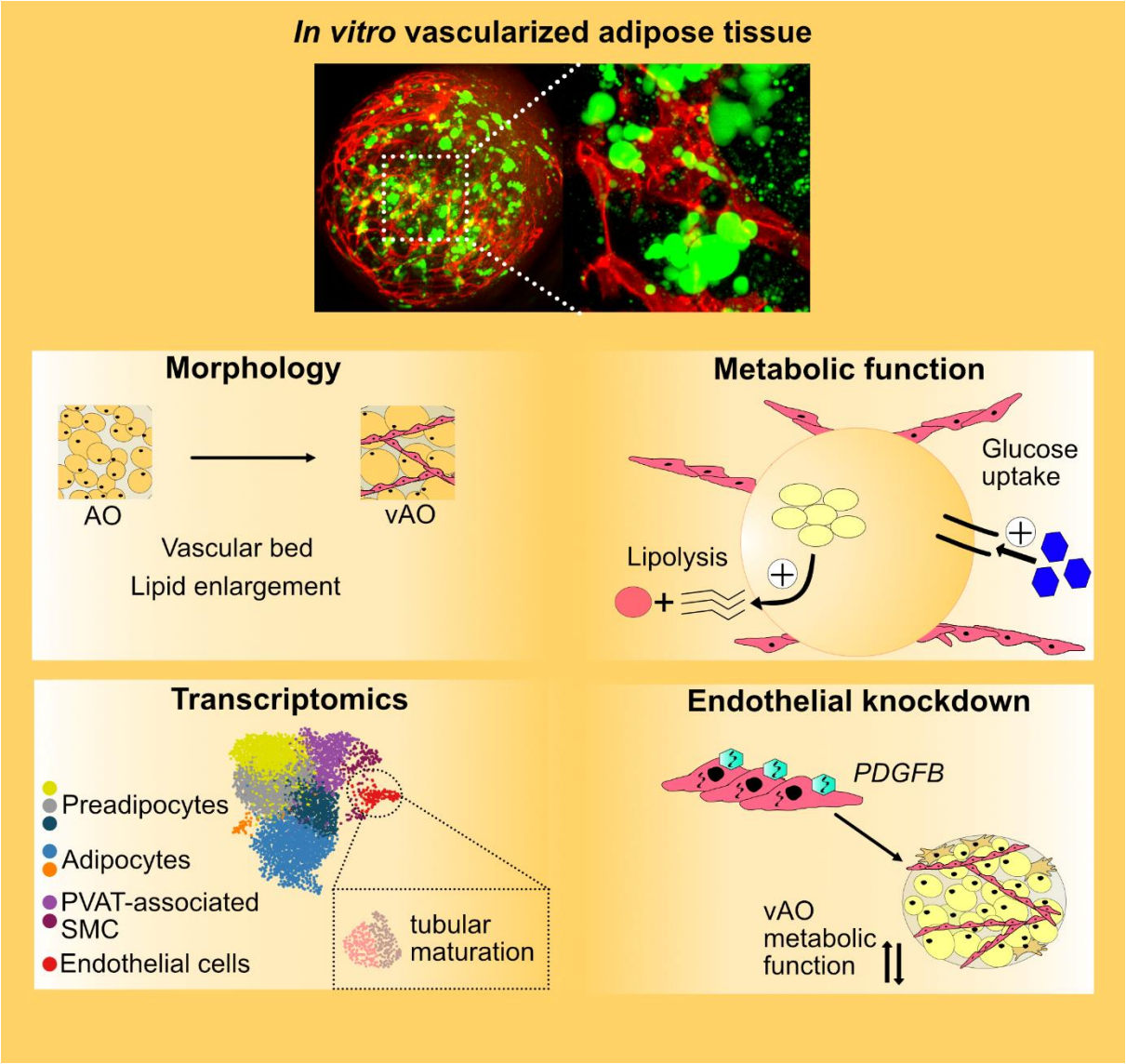

Figure 20 Graphical abstract summarizing *in-vitro* vascularized adipose tissue engineering achievements.

Adipose-derived stem cells and stem-cell derived endothelial cells were embedded in a physiologic matrix to self-assemble and mature towards *in-vitro* vascularized AT. Organoids were densified and revealed enlarged lipid droplet formation. Interestingly, organoids displayed advanced AT-specific functionality as insulin-mediated glucose uptake or ß-adrenergic lipolysis. Single cell/nuclei RNA transcriptomics revealed possible PVAT-associated adipose progenitors und tubular maturation in endothelial cells. The model was exploited for EC-adipocyte interaction studies using endothelial-specific genetic knockdown.

4.4 Declaration of contributions

The experiments, analyses, and results described in the recent chapter were carried out in the biggest part by me. These included the cultivation of hASC and ECs as well as the establishment of the 3D organoid model including media, cell ratio and

cultivation conditions . I adjusted existing protocols for functional assays such as the lipolysis and glucose uptake assay and executed these. I did whole-mount immunofluorescence staining, IF microscopy and following lipid droplet and endothelial network analysis with Scott Atwell helping me establishing a code for fiji image analysis. Additionally, I prepared samples for scRNAseq experiment where Giannis K. Deligiannis and Mateusz Strzelecki supported me establishing a protocol for nuclei extraction from organoids. I performed analysis of sc/snRNAseq data, where Yiran Zheng performed donor identification analysis and Sandra Wiedenmann generated the dataset for cell-cell communication analysis that I further analyzed. Zoë Kentischer, Caroline Remmert and me performed cryo-section IF staining. Caroline Remmert and me performed microscopy of cryo-sectioned IF staining. The lentiviral knockdown sub-study was designed by Matthias Meier and Bilal Sheikh and me. Fabiana Oliveira produced lentiviral particles and performed confirmative PCR and p24 ELISA. Fabiana Oliveira and me performed cell culture experiments for lentiviral transduction of hiPSC and passaging. I did downstream cell culture experiments, lipolysis assay and image analysis of lentiviral knockdown sub-project starting from hiPSC-to-EC differentiation. I designed the figures and Matthias Meier and me wrote the preliminary manuscript for the upcoming publication.

Acknowledgements

This work was supported by the Helmholtz Pioneer Campus and ERC Consolidator Grant (Number 772646). We thank Daniel Kokotek, Ioannis Deligiannis, Mateusz Strzelecki, Celia Martinez, and Inti I. A. de la Rosa Velazquez and G. Eckstein for helping with the sample preparation and performing the NovaSeq sequencing. Further we thank Thomas Schwarz-Romond for critically reading the manuscript.

4.5 Extended data

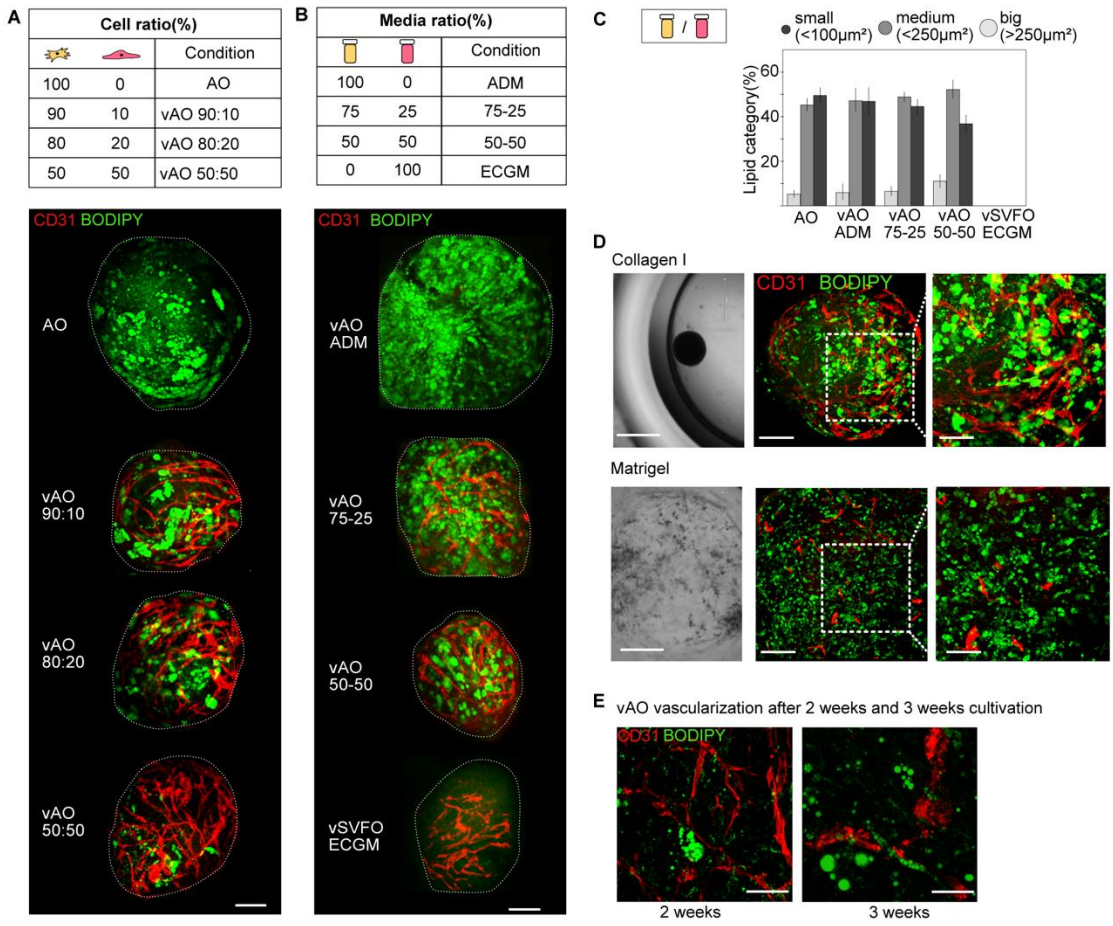

Figure S 1 Establishment of an In Vitro Engineered Vascularized Adipose Tissue Model
Related to Figure 13.

(A) Overview of tested cell ratios, shown with representative confocal 3D projections of wholemount vascularized adipose tissue organoids stained for lipid droplets (BODIPY) and endothelial markers (CD31). Scale bar: 100 µm. (B) Overview of different media conditions tested, illustrated with representative confocal 3D projections of wholemount vascularized adipose tissue organoids. Scale bar: 100 µm. (C) Lipid droplet size distribution analysis based on BODIPY-stained confocal 3D projections under different media conditions (n ≥ 4–12 from 2–5 independent experiments), corresponding to Figure 1D. Error bars represent 95% confidence intervals (CI). (D) Human adipose-derived stem cell (hASC) and self-assembled endothelial cell (SC-EC) co-cultures were cultivated in either Matrigel or collagen I hydrogel for 14 days. Fluorescent staining for lipid droplets (BODIPY) and endothelial cell structures (CD31) was performed. Scale bars: brightfield, 750 µm; confocal fluorescence images, 100 µm and 50 µm. (E) hASC-SC-EC co-cultures were cultivated for 14 or 21 days and analyzed by fluorescent staining for lipid droplets (BODIPY) and endothelial structures (CD31). Scale bar: 50 µm.

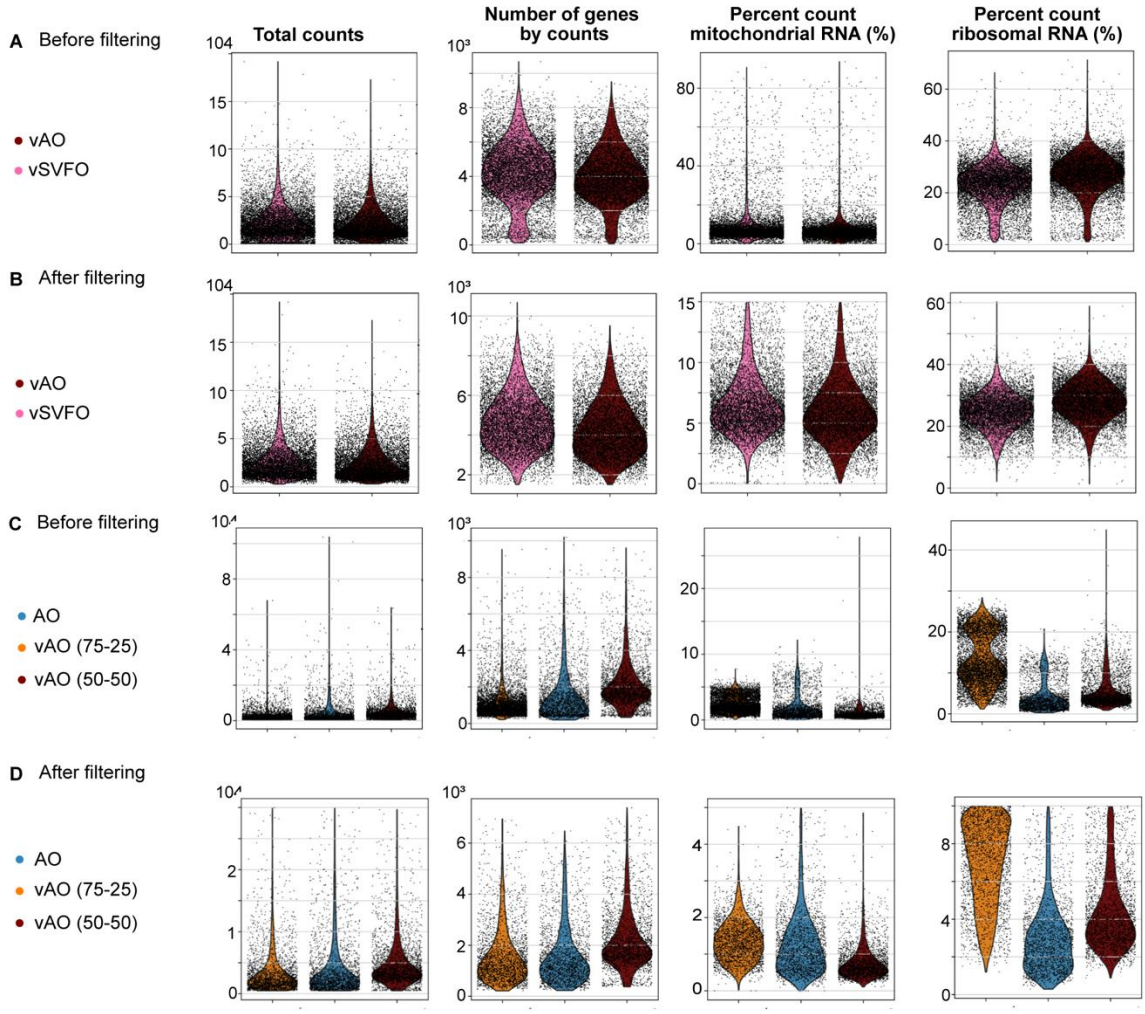

Figure S 2 Quality Parameters of Single-Cell and Single-Nuclei Datasets Before and After Filtering Related to Figures 16 and 17.

Violin plots illustrating key quality parameters, including total cell counts, the number of genes per cell, and the percentage (%) of mitochondrial and ribosomal RNA counts: (A) Two scRNA-seq datasets before filtering. (B) Two scRNA-seq datasets after filtering. (C) Three snRNA-seq datasets before filtering. (D) Three snRNA-seq datasets after filtering.

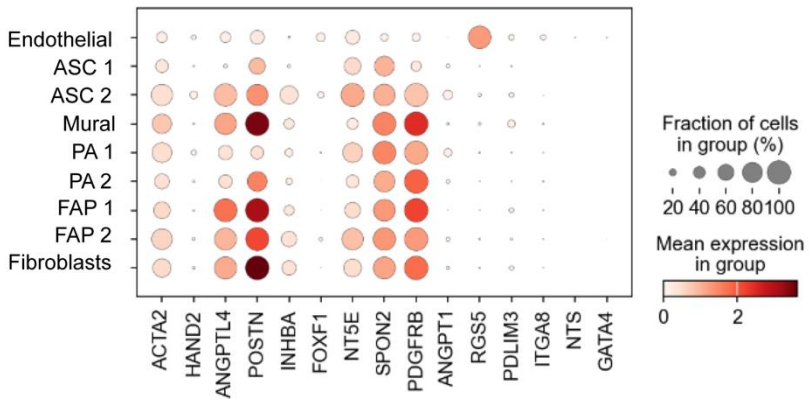

Figure S 3. Mural marker expression in the respective cell clusters found in vAOs and AOs. Related to Figure 16.

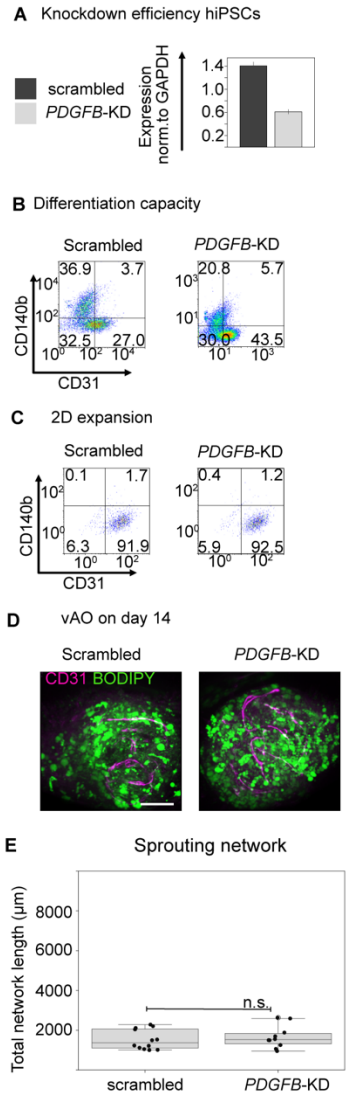

Figure S 4 Successful Lentiviral Knockdown of Genes Related to EC-Adipocyte Interaction in SC-ECs and Integration into a Vascularized Adipose Tissue Model Related to Figure 19.

(A) Validation of gene knockdown efficiency in hiPSCs by qPCR (n = 4 technical replicates). Gene expression levels were normalized to the housekeeping gene GAPDH. Error bars represent 95% confidence intervals (CI). (B) Assessment of endothelial differentiation efficiency by flow cytometry analysis of endothelial marker CD31 and perivascular marker PDGFRβ. (C) Confirmation of endothelial lineage stability after two passages via flow cytometry analysis of CD31 and PDGFRβ markers. (D) Representative confocal z-projections of wholemount vascularized adipose tissue (vascCo-AT) stained for lipid droplets (BODIPY) and endothelial structures (CD31). Scale bar: 100 µm. (E) Sprouting network analysis based on CD31-stained confocal 3D image projections. (N=3, n≥10). Error bars indicate 95% confidence level.

5 Conclusion

Being an abundant health issue worldwide, great effort is made to understand the complex causalities of metabolic syndrome-related complications like obesity, CVD and T2DM[16]. As the endothelial system is highly affected by metabolic alterations as seen for atherosclerosis, profound studies have been performed to understand the pathomechanism but unclarities still remain[95]. Mouse models have been extensively used to model metabolic syndrome-related conditions but reach limits in fully recapitulating human physiology[95]. Whilst classical human 2D cell culture models may not reflect complex vessel architecture, 3D vessel-on-chip devices have recently been engineered to rebuild endothelial lumen under flow investigating vessel function in health and diseased state[211].

During this thesis, I established an open surface, easily manipulable and scalable vessel-on-chip platform. SC-ECs were allowed to form a stable lumen within a physiological matrix while being exposed to vasculature-relevant perfusion. Flow induction on a rocking shaker system enabled for alleviated handling of multiplied amount of lumen maximizing experimental throughput per experiment. Therefore, this system marks an advancement over other available platforms that may either provide a scalable multi-well format[37] but endothelial lumen being aligned on less physiological polymer surface or more elaborate set-ups with physiological lumen matrix that only provide one sample per chip[35]. Technically, the platform was exploited for a range of biological tools as for high resolution imaging and functional assays on-chip, scRNAseq or proteomics. The open chip format facilitated extraction of single cells and unscathed whole lumen structure for downstream analysis. As other platforms showed before, flow induction leads to advanced functionality towards a static model regarding barrier integrity[35], sprouting ECM remodeling and endothelial NO-synthesis. This maturation effect was reflected by transcriptomic cell states[102] with arterial-like and *in-vivo*-resembling gene expression. Finally, the vessel-on-chip could successfully model the impact of oxidative stress during the on-set of endothelial dysfunction in atherosclerosis[42].

Next to CVD-related alterations in vasculature, recent focus has been set on the interactions of endothelial vessels with metabolically active organs like AT and how these interactions contribute to organ function in health state and in metabolic syndrome[54]. Disturbed endothelial-adipocyte interactions are now known to accelerate

the course of obesity[53]. Human 3D organoids can serve as reliable, highly controllable experimental models[67]. Vascularized AT organoid models are in development but face limitations regarding simultaneous maturation of vessels and adipocytes[78,79].

As second aim of this thesis, I bioengineered a vascularized organoid model of AT. I established media, cell ratio and cultivation conditions achieving a highly vascularized vAO model with enlarged adipocytes as sign of increasing maturity[69,70]. As other models[212] already demonstrated, vasculature lead to improved adipocyte functionality as for ß-adrenergic lipolysis. Until now, vascularized AT organoids have been studied only for single marker expression[76,212] on transcriptome level. As new achievement in the field, I executed profound studies of co-evolving endothelial and adipocyte progenitor cell states on single-cell transcriptome level. The technique revealed possible endothelial-adipocyte specific interactions that could be further mechanistically examined as shown by an endothelial-specific knock-down. Thus, the model has high potential to unravel new adipocyte-endothelial communication axes and could help to find interventions for obesity and metabolic syndrome.

In both model systems, hiPSC-derived ECs (SC-ECs) were proven to successfully form extended vessel structures and single cell transcriptome showed advancements of endothelial maturity both when cultivated under physiologic flow and in the organ-specific environment of AT. Regarding the vAO model, hiPSC-derived ECs were successfully applied in a vascularized AT organoid for the first time. HiPSC-derived ECs have advantages over classically used EC sources like HUVECs[106], as they are highly scalable while reducing donor-specific experimental differences. For the future, hiPSC may serve as cellular source for screening of patient-specific metabolic alterations in presented model platforms.

6 Outlook

In conclusion, the two newly developed models presented in this thesis achieved important functional advances towards *in-vivo* mimicking endothelial vessel and vascularized AT. For further investigations, both models were proved to be at matured engineering stage to be combined as comprehensive AT-on-chip platform with relevant organ perfusion. Connecting endothelial vessels within vAO to an outer flow-induced vascular system would probably allow EC survival also in long-term culture[213]. In the same time, longer maturation in co-culture would possibly improve adipocyte maturation *in-vitro*[70]. Not only EC react to mechanical flow stimulus, also adipocytes differentiation may benefit from perfusion[214]. The objective would be to grow matured, unilocular-like adipocytes in a vascular bed for long-term cultivation improving *in-vivo* resemblance of the system for future studies.

7 Literature

1. Rosowski, S. *et al.* Single-cell characterization of neovascularization using hiPSC-derived endothelial cells in a 3D microenvironment. *Stem Cell Rep.* **18**, 1972–1986 (2023).
2. Marder, M. *et al.* Stem cell-derived vessels-on-chip for cardiovascular disease modeling. *Cell Rep.* **43**, 114008 (2024).
3. Remmert, C., Otgonbayar, M., Perschel, J. A., Marder, M. & Meier, M. Protocol to generate a microfluidic vessels-on-chip platform using human pluripotent stem cell-derived endothelial cells. *STAR Protoc.* **5**, 103300 (2024).
4. Pugsley, M. K. & Tabrizchi, R. The vascular system: An overview of structure and function. *J. Pharmacol. Toxicol. Methods* **44**, 333–340 (2000).
5. Eichmann, A. *et al.* Vascular development: from precursor cells to branched arterial and venous networks. *Int. J. Dev. Biol.* **49**, 259–267 (2005).
6. Cong, X. & Kong, W. Endothelial tight junctions and their regulatory signaling pathways in vascular homeostasis and disease. *Cell. Signal.* **66**, 109485 (2020).
7. Campinho, P., Vilfan, A. & Vermot, J. Blood Flow Forces in Shaping the Vascular System: A Focus on Endothelial Cell Behavior. *Front. Physiol.* **11**, (2020).
8. Harrison, D. G. *et al.* Endothelial mechanotransduction, nitric oxide and vascular inflammation. *J. Intern. Med.* **259**, 351–363 (2006).
9. Halper, J. Chapter Four - Basic Components of Vascular Connective Tissue and Extracellular Matrix. in *Advances in Pharmacology* (ed. Khalil, R. A.) vol. 81 95–127 (Academic Press, 2018).
10. Yue, B. Biology of the Extracellular Matrix: An Overview. *J. Glaucoma* S20–S23 (2014) doi:10.1097/IJG.0000000000000108.
11. Plikus, M. V. *et al.* Fibroblasts: origins, definitions, and functions in health and disease. *Cell* **184**, 3852–3872 (2021).
12. Alberts, B. *et al.* Blood Vessels and Endothelial Cells. in *Molecular Biology of the Cell. 4th edition* (Garland Science, 2002).
13. Armulik, A., Abramsson, A. & Betsholtz, C. Endothelial/Pericyte Interactions. *Circ. Res.* **97**, 512–523 (2005).
14. Patan, S. Vasculogenesis and angiogenesis. *Cancer Treat. Res.* **117**, 3–32 (2004).

15. Reiterer, M. & Branco, C. M. Endothelial cells and organ function: applications and implications of understanding unique and reciprocal remodelling. *FEBS J.* **287**, 1088–1100 (2020).
16. Wang, H. H., Lee, D. K., Liu, M., Portincasa, P. & Wang, D. Q.-H. Novel Insights into the Pathogenesis and Management of the Metabolic Syndrome. *Pediatr. Gastroenterol. Hepatol. Nutr.* **23**, 189–230 (2020).
17. Xu, S. *et al.* Endothelial Dysfunction in Atherosclerotic Cardiovascular Diseases and Beyond: From Mechanism to Pharmacotherapies. *Pharmacol. Rev.* **73**, 924–967 (2021).
18. Poznyak, A. V. *et al.* Overview of OxLDL and Its Impact on Cardiovascular Health: Focus on Atherosclerosis. *Front. Pharmacol.* **11**, (2021).
19. Madamanchi, N. R., Vendrov, A. & Runge, M. S. Oxidative stress and vascular disease. *Arterioscler. Thromb. Vasc. Biol.* **25**, 29–38 (2005).
20. Ghosh, A., Gao, L., Thakur, A., Siu, P. M. & Lai, C. W. K. Role of free fatty acids in endothelial dysfunction. *J. Biomed. Sci.* **24**, 50 (2017).
21. Jebari-Benslaiman, S. *et al.* Pathophysiology of Atherosclerosis. *Int. J. Mol. Sci.* **23**, 3346 (2022).
22. Townsend, N. *et al.* Epidemiology of cardiovascular disease in Europe. *Nat. Rev. Cardiol.* **19**, 133–143 (2022).
23. Savoji, H. *et al.* Cardiovascular disease models: A game changing paradigm in drug discovery and screening. *Biomaterials* **198**, 3–26 (2019).
24. Walther, B. K. *et al.* Mechanotransduction-on-chip: vessel-chip model of endothelial YAP mechanobiology reveals matrix stiffness impedes shear response. *Lab. Chip* **21**, 1738–1751 (2021).
25. Chen, J. *et al.* Recent Progress in in vitro Models for Atherosclerosis Studies. *Front. Cardiovasc. Med.* **8**, (2022).
26. Simitian, G., Virumbrales-Muñoz, M., Sánchez de Diego, C., Beebe, D. J. & Kosoff, D. Microfluidics in vascular biology research: a critical review for engineers, biologists, and clinicians. *Lab. Chip* **22**, 3618–3636 (2022).
27. Kennedy, C. C., Brown, E. E., Abutaleb, N. O. & Truskey, G. A. Development and Application of Endothelial Cells Derived From Pluripotent Stem Cells in Microphysiological Systems Models. *Front. Cardiovasc. Med.* **8**, (2021).

28. Liu, G., David, B. T., Trawczynski, M. & Fessler, R. G. Advances in Pluripotent Stem Cells: History, Mechanisms, Technologies, and Applications. *Stem Cell Rev. Rep.* **16**, 3–32 (2020).
29. Patsch, C. *et al.* Generation of vascular endothelial and smooth muscle cells from human pluripotent stem cells. *Nat. Cell Biol.* **17**, 994–1003 (2015).
30. Roux, E., Bougaran, P., Dufourcq, P. & Couffinhal, T. Fluid Shear Stress Sensing by the Endothelial Layer. *Front. Physiol.* **11**, (2020).
31. Papaioannou, T. G. & Stefanadis, C. Vascular wall shear stress: basic principles and methods. *Hell. J. Cardiol. HJC Hell. Kardiologike Epitheorese* **46**, 9–15 (2005).
32. Bulboacă, A.-E., Boarescu, P. M., Melincovici, C. S. & Mihu, C. M. Microfluidic endothelium-on-a-chip development, from in vivo to in vitro experimental models. *Rom. J. Morphol. Embryol.* **61**, 15–23 (2020).
33. Niculescu, A.-G., Chircov, C., Bîrcă, A. C. & Grumezescu, A. M. Fabrication and Applications of Microfluidic Devices: A Review. *Int. J. Mol. Sci.* **22**, 2011 (2021).
34. Gale, B. K. *et al.* A Review of Current Methods in Microfluidic Device Fabrication and Future Commercialization Prospects. *Inventions* **3**, 60 (2018).
35. Polacheck, W. J., Kutys, M. L., Tefft, J. B. & Chen, C. S. Microfabricated blood vessels for modeling the vascular transport barrier. *Nat. Protoc.* **14**, 1425–1454 (2019).
36. Iakovlev, A. P., Erofeev, A. S. & Gorelkin, P. V. Novel Pumping Methods for Microfluidic Devices: A Comprehensive Review. *Biosensors* **12**, 956 (2022).
37. van Duinen, V. *et al.* Perfused 3D angiogenic sprouting in a high-throughput in vitro platform. *Angiogenesis* **22**, 157–165 (2019).
38. Moses, S. R., Adorno, J. J., Palmer, A. F. & Song, J. W. Vessel-on-a-chip models for studying microvascular physiology, transport, and function in vitro. *Am. J. Physiol.-Cell Physiol.* **320**, C92–C105 (2021).
39. Chu, P.-Y. *et al.* Development of vessel mimicking microfluidic device for studying mechano-response of endothelial cells. *iScience* **26**, 106927 (2023).
40. Zaragoza, C. *et al.* Animal Models of Cardiovascular Diseases. *BioMed Res. Int.* **2011**, e497841 (2011).
41. Chandra Sekar, N., Khoshmanesh, K. & Baratchi, S. Bioengineered models of cardiovascular diseases. *Atherosclerosis* 117565 (2024) doi:10.1016/j.atherosclerosis.2024.117565.

42. Su, C. *et al.* A novel human arterial wall-on-a-chip to study endothelial inflammation and vascular smooth muscle cell migration in early atherosclerosis. *Lab. Chip* (2021) doi:10.1039/D1LC00131K.
43. Sakers, A., De Siqueira, M. K., Seale, P. & Villanueva, C. J. Adipose-tissue plasticity in health and disease. *Cell* **185**, 419–446 (2022).
44. An, S.-M., Cho, S.-H. & Yoon, J. C. Adipose Tissue and Metabolic Health. *Diabetes Metab. J.* **47**, 595–611 (2023).
45. Luo, L. & Liu, M. Adipose tissue in control of metabolism. *J. Endocrinol.* **231**, R77–R99 (2016).
46. Merrick, D. *et al.* Identification of a mesenchymal progenitor cell hierarchy in adipose tissue. *Science* **364**, eaav2501 (2019).
47. Jakab, J. *et al.* Adipogenesis as a Potential Anti-Obesity Target: A Review of Pharmacological Treatment and Natural Products. *Diabetes Metab. Syndr. Obes. Targets Ther.* **14**, 67–83 (2021).
48. Rosen, E. D. & MacDougald, O. A. Adipocyte differentiation from the inside out. *Nat. Rev. Mol. Cell Biol.* **7**, 885–896 (2006).
49. Liu, X., Zhang, Z., Song, Y., Xie, H. & Dong, M. An update on brown adipose tissue and obesity intervention: Function, regulation and therapeutic implications. *Front. Endocrinol.* **13**, 1065263 (2023).
50. Rabiee, A. Beige Fat Maintenance; Toward a Sustained Metabolic Health. *Front. Endocrinol.* **11**, (2020).
51. Markussen, L. K. *et al.* Lipolysis regulates major transcriptional programs in brown adipocytes. *Nat. Commun.* **13**, 3956 (2022).
52. Ioannidou, A., Fisher, R. M. & Hagberg, C. E. The multifaceted roles of the adipose tissue vasculature. *Obes. Rev. Off. J. Int. Assoc. Study Obes.* e13403 (2021) doi:10.1111/obr.13403.
53. AlZaim, I., de Rooij, L. P. M. H., Sheikh, B. N., Börgeson, E. & Kalucka, J. The evolving functions of the vasculature in regulating adipose tissue biology in health and obesity. *Nat. Rev. Endocrinol.* **19**, 691–707 (2023).
54. Herold, J. & Kalucka, J. Angiogenesis in Adipose Tissue: The Interplay Between Adipose and Endothelial Cells. *Front. Physiol.* **11**, (2021).
55. Luk, C., Haywood, N. J., Bridge, K. I. & Kearney, M. T. Paracrine Role of the Endothelium in Metabolic Homeostasis in Health and Nutrient Excess. *Front. Cardiovasc. Med.* **9**, (2022).

56. Gogg, S., Nerstedt, A., Boren, J. & Smith, U. Human adipose tissue microvascular endothelial cells secrete PPARγ ligands and regulate adipose tissue lipid uptake. *JCI Insight* **4**, e125914.
57. Fukumura, D. *et al.* Paracrine regulation of angiogenesis and adipocyte differentiation during in vivo adipogenesis. *Circ. Res.* **93**, e88-97 (2003).
58. Varzaneh, F. E., Shillabeer, G., Wong, K.-L. & Lau, D. C. W. Extracellular matrix components secreted by microvascular endothelial cells stimulate preadipocyte differentiation in vitro. *Metabolism* **43**, 906–912 (1994).
59. Corvera, S. & Gealekman, O. Adipose tissue angiogenesis: Impact on obesity and type-2 diabetes. *Biochim. Biophys. Acta BBA - Mol. Basis Dis.* **1842**, 463–472 (2014).
60. Hildebrand, S., Stümer, J. & Pfeifer, A. PVAT and Its Relation to Brown, Beige, and White Adipose Tissue in Development and Function. *Front. Physiol.* **9**, (2018).
61. Hagberg, C. E. & Spalding, K. L. White adipocyte dysfunction and obesity-associated pathologies in humans. *Nat. Rev. Mol. Cell Biol.* **25**, 270–289 (2024).
62. Blüher, M. Metabolically Healthy Obesity. *Endocr. Rev.* **41**, bnaa004 (2020).
63. Chait, A. & den Hartigh, L. J. Adipose Tissue Distribution, Inflammation and Its Metabolic Consequences, Including Diabetes and Cardiovascular Disease. *Front. Cardiovasc. Med.* **7**, (2020).
64. Cao, Y. Adipose tissue angiogenesis as a therapeutic target for obesity and metabolic diseases. *Nat. Rev. Drug Discov.* **9**, 107–115 (2010).
65. Volz, A.-C., Huber, B. & Kluger, P. J. Adipose-derived stem cell differentiation as a basic tool for vascularized adipose tissue engineering. *Differentiation* **92**, 52–64 (2016).
66. Peirsman, A. *et al.* Vascularized adipose tissue engineering: moving towards soft tissue reconstruction. *Biofabrication* (2023) doi:10.1088/1758-5090/acd7a5.
67. Murphy, C. S., Liaw, L. & Reagan, M. R. In vitro tissue-engineered adipose constructs for modeling disease. *BMC Biomed. Eng.* **1**, 27 (2019).
68. Gibler, P. *et al.* Human Adipose-Derived Stromal/Stem Cell Culture and Analysis Methods for Adipose Tissue Modeling In Vitro: A Systematic Review. *Cells* **10**, 1378 (2021).
69. Mora, I., Puiggròs, F., Serras, F., Gil-Cardoso, K. & Escoté, X. Emerging models for studying adipose tissue metabolism. *Biochem. Pharmacol.* **223**, 116123 (2024).

70. Ioannidou, A. *et al.* Hypertrophied human adipocyte spheroids as in vitro model of weight gain and adipose tissue dysfunction. *J. Physiol.* **n/a**, (2022).
71. Rogal, J. *et al.* WAT-on-a-chip integrating human mature white adipocytes for mechanistic research and pharmaceutical applications. *Sci. Rep.* **10**, 6666 (2020).
72. Compera, N. *et al.* Adipose microtissue-on-chip: a 3D cell culture platform for differentiation, stimulation, and proteomic analysis of human adipocytes. *Lab. Chip* **22**, 3172–3186 (2022).
73. Benmeridja, L. *et al.* High-throughput fabrication of vascularized adipose microtissues for 3D bioprinting. *J. Tissue Eng. Regen. Med.* **14**, 840–854 (2020).
74. Louis, F., Kitano, S., Mano, J. F. & Matsusaki, M. 3D collagen microfibers stimulate the functionality of preadipocytes and maintain the phenotype of mature adipocytes for long term cultures. *Acta Biomater.* **84**, 194–207 (2019).
75. DeBari, M. K. *et al. Engineering 3D Vascularized Adipose Tissue Construct Using a Decellularized Lung Matrix*. 2021.06.22.449445 https://www.biorxiv.org/content/10.1101/2021.06.22.449445v1 (2021) doi:10.1101/2021.06.22.449445.
76. Acosta, F. M. *et al.* Engineering Functional Vascularized Beige Adipose Tissue from Microvascular Fragments of Models of Healthy and Type II Diabetes Conditions. *J. Tissue Eng.* **13**, 20417314221109337 (2022).
77. Yao, X. & Dani, C. A Simple Method for Generating, Clearing, and Imaging Pre-vascularized 3D Adipospheres Derived from Human iPS Cells. in *Induced Pluripotent Stem (iPS) Cells: Methods and Protocols* (eds. Nagy, A. & Turksen, K.) 495–507 (Springer US, New York, NY, 2022). doi:10.1007/7651_2021_360.
78. Acosta, F. M., Stojkova, K., Brey, E. M. & Rathbone, C. R. A Straightforward Approach to Engineer Vascularized Adipose Tissue Using Microvascular Fragments. *Tissue Eng. Part A* **26**, 905–914 (2020).
79. Muller, S. *et al.* Human adipose stromal-vascular fraction self-organizes to form vascularized adipose tissue in 3D cultures. *Sci. Rep.* **9**, 7250 (2019).
80. Niu, R.-Z. *et al.* Single-cell transcriptome unveils unique transcriptomic signatures of human organ-specific endothelial cells. *Basic Res. Cardiol.* **119**, 973–999 (2024).
81. Bondareva, O. *et al.* Single-cell profiling of vascular endothelial cells reveals progressive organ-specific vulnerabilities during obesity. *Nat. Metab.* **4**, 1591–1610 (2022).

82. THE TABULA SAPIENS CONSORTIUM. The Tabula Sapiens: A multiple-organ, single-cell transcriptomic atlas of humans. *Science* **376**, eabl4896 (2022).
83. Zhao, P. *et al.* Single-cell RNA-seq reveals a critical role of novel pro-inflammatory EndMT in mediating adverse remodeling in coronary artery–on–a–chip. *Sci. Adv.* **7**, eabg1694 (2021).
84. McInnes, L., Healy, J. & Melville, J. UMAP: Uniform Manifold Approximation and Projection for Dimension Reduction. Preprint at https://doi.org/10.48550/arXiv.1802.03426 (2020).
85. Jovic, D. *et al.* Single-cell RNA sequencing technologies and applications: A brief overview. *Clin. Transl. Med.* **12**, e694 (2022).
86. Nguyen, Q. H., Pervolarakis, N., Nee, K. & Kessenbrock, K. Experimental Considerations for Single-Cell RNA Sequencing Approaches. *Front. Cell Dev. Biol.* **6**, (2018).
87. Bergen, V., Lange, M., Peidli, S., Wolf, F. A. & Theis, F. J. Generalizing RNA velocity to transient cell states through dynamical modeling. *Nat. Biotechnol.* **38**, 1408–1414 (2020).
88. La Manno, G. *et al.* RNA velocity of single cells. *Nature* **560**, 494–498 (2018).
89. Jemal, M. High-throughput quantitative bioanalysis by LC/MS/MS. *Biomed. Chromatogr. BMC* **14**, 422–429 (2000).
90. Kassem, S. *et al.* Proteomics for Low Cell Numbers: How to Optimize the Sample Preparation Workflow for Mass Spectrometry Analysis. *J. Proteome Res.* **20**, 4217–4230 (2021).
91. Jung, S. *et al.* Integrating Vascular Phenotypic and Proteomic Analysis in an Open Microfluidic Platform. *ACS Nano* **18**, 24909–24928 (2024).
92. Sakuma, T., Barry, M. A. & Ikeda, Y. Lentiviral vectors: basic to translational. *Biochem. J.* **443**, 603–618 (2012).
93. Mátrai, J., Chuah, M. K. & VandenDriessche, T. Recent Advances in Lentiviral Vector Development and Applications. *Mol. Ther.* **18**, 477–490 (2010).
94. Singer, O. & Verma, I. M. Applications of Lentiviral Vectors for shRNA Delivery and Transgenesis. *Curr. Gene Ther.* **8**, 483–488 (2008).
95. Tran, V. *et al.* The Vascular Consequences of Metabolic Syndrome: Rodent Models, Endothelial Dysfunction, and Current Therapies. *Front. Pharmacol.* **11**, (2020).

96. Ricard, N., Bailly, S., Guignabert, C. & Simons, M. The quiescent endothelium: signalling pathways regulating organ-specific endothelial normalcy. *Nat. Rev. Cardiol.* **18**, 565–580 (2021).
97. Trimm, E. & Red-Horse, K. Vascular endothelial cell development and diversity. *Nat. Rev. Cardiol.* **20**, 197–210 (2023).
98. von Scheidt, M. *et al.* Applications and Limitations of Mouse Models for Understanding Human Atherosclerosis. *Cell Metab.* **25**, 248–261 (2017).
99. Williams, I. M. & Wu, J. C. Generation of Endothelial Cells From Human Pluripotent Stem Cells. *Arterioscler. Thromb. Vasc. Biol.* **39**, 1317–1329 (2019).
100. Vila Cuenca, M. *et al.* Engineered 3D vessel-on-chip using hiPSC-derived endothelial- and vascular smooth muscle cells. *Stem Cell Rep.* **16**, 2159–2168 (2021).
101. Cochrane, A. *et al.* Advanced in vitro models of vascular biology: Human induced pluripotent stem cells and organ-on-chip technology. *Adv. Drug Deliv. Rev.* **140**, 68–77 (2019).
102. Helle, E., Ampuja, M., Antola, L. & Kivelä, R. Flow-Induced Transcriptomic Remodeling of Endothelial Cells Derived From Human Induced Pluripotent Stem Cells. *Front. Physiol.* **11**, (2020).
103. Nguyen, D.-H. T. *et al.* Biomimetic model to reconstitute angiogenic sprouting morphogenesis in vitro. *Proc. Natl. Acad. Sci.* **110**, 6712–6717 (2013).
104. Hajal, C. *et al.* Engineered human blood–brain barrier microfluidic model for vascular permeability analyses. *Nat. Protoc.* **17**, 95–128 (2022).
105. Trietsch, S. J., Israëls, G. D., Joore, J., Hankemeier, T. & Vulto, P. Microfluidic titer plate for stratified 3D cell culture. *Lab. Chip* **13**, 3548–3554 (2013).
106. Zhang, X. *et al.* Modeling early stage atherosclerosis in a primary human vascular microphysiological system. *Nat. Commun.* **11**, 5426 (2020).
107. Compera, N., Atwell, S., Wirth, J., Wolfrum, B. & Meier, M. Upscaling of pneumatic membrane valves for the integration of 3D cell cultures on chip. *Lab. Chip* **21**, 2986–2996 (2021).
108. Schindelin, J. *et al.* Fiji: an open-source platform for biological-image analysis. *Nat. Methods* **9**, 676–682 (2012).
109. Tinevez, J.-Y. *et al.* TrackMate: An open and extensible platform for single-particle tracking. *Methods San Diego Calif* **115**, 80–90 (2017).

110. Schmidt, U., Weigert, M., Broaddus, C. & Myers, G. Cell Detection with Star-convex Polygons. in vol. 11071 265–273 (2018).
111. Wolf, F. A., Angerer, P. & Theis, F. J. SCANPY: large-scale single-cell gene expression data analysis. *Genome Biol.* **19**, 15 (2018).
112. Wolock, S. L., Lopez, R. & Klein, A. M. Scrublet: Computational Identification of Cell Doublets in Single-Cell Transcriptomic Data. *Cell Syst.* **8**, 281-291.e9 (2019).
113. Traag, V. A., Waltman, L. & van Eck, N. J. From Louvain to Leiden: guaranteeing well-connected communities. *Sci. Rep.* **9**, 5233 (2019).
114. Abdelmagid, S. A. *et al.* Comprehensive profiling of plasma fatty acid concentrations in young healthy Canadian adults. *PloS One* **10**, e0116195 (2015).
115. Hladik, D. *et al.* CREB Signaling Mediates Dose-Dependent Radiation Response in the Murine Hippocampus Two Years after Total Body Exposure. *J. Proteome Res.* **19**, 337–345 (2020).
116. Navarro, P. *et al.* General Statistical Framework for Quantitative Proteomics by Stable Isotope Labeling. *J. Proteome Res.* **13**, 1234–1247 (2014).
117. Benjamini, Y. & Hochberg, Y. Controlling the False Discovery Rate: A Practical and Powerful Approach to Multiple Testing. *J. R. Stat. Soc. Ser. B Methodol.* **57**, 289–300 (1995).
118. Uhlén, M. *et al.* The human secretome. *Sci. Signal.* **12**, eaaz0274 (2019).
119. Raudvere, U. *et al.* g:Profiler: a web server for functional enrichment analysis and conversions of gene lists (2019 update). *Nucleic Acids Res.* **47**, W191–W198 (2019).
120. Kuleshov, M. V. *et al.* Enrichr: a comprehensive gene set enrichment analysis web server 2016 update. *Nucleic Acids Res.* **44**, W90-97 (2016).
121. Rhodes, J. M. & Simons, M. The extracellular matrix and blood vessel formation: not just a scaffold. *J. Cell. Mol. Med.* **11**, 176–205 (2007).
122. Muhl, L. *et al.* Single-cell analysis uncovers fibroblast heterogeneity and criteria for fibroblast and mural cell identification and discrimination. *Nat. Commun.* **11**, 3953 (2020).
123. McCracken, I. R. *et al.* Mapping the developing human cardiac endothelium at single-cell resolution identifies MECOM as a regulator of arteriovenous gene expression. *Cardiovasc. Res.* **118**, 2960–2972 (2022).

124. Dekker, R. J. *et al.* Endothelial KLF2 Links Local Arterial Shear Stress Levels to the Expression of Vascular Tone-Regulating Genes. *Am. J. Pathol.* **167**, 609–618 (2005).
125. Bae, Y. S., Oh, H., Rhee, S. G. & Yoo, Y. D. Regulation of Reactive Oxygen Species Generation in Cell Signaling. *Mol. Cells* **32**, 491–509 (2011).
126. Galbusera, M. *et al.* Fluid shear stress modulates von Willebrand factor release from human vascular endothelium. *Blood* **90**, 1558–1564 (1997).
127. Fang, J. S. *et al.* Shear-induced Notch-Cx37-p27 axis arrests endothelial cell cycle to enable arterial specification. *Nat. Commun.* **8**, 2149 (2017).
128. Magid, R., Murphy, T. J. & Galis, Z. S. Expression of matrix metalloproteinase-9 in endothelial cells is differentially regulated by shear stress. Role of c-Myc. *J. Biol. Chem.* **278**, 32994–32999 (2003).
129. Morancho, A. *et al.* Impaired Vascular Remodeling after Endothelial Progenitor Cell Transplantation in MMP9-Deficient Mice Suffering Cortical Cerebral Ischemia. *J. Cereb. Blood Flow Metab.* **35**, 1547–1551 (2015).
130. Morawietz, H., Wagner, A. H., Hecker, M. & Goettsch, W. Endothelin receptor B-mediated induction of c-jun and AP-1 in response to shear stress in human endothelial cells. *Can. J. Physiol. Pharmacol.* **86**, 499–504 (2008).
131. Hautefort, A., Pfenniger, A. & Kwak, B. R. Endothelial connexins in vascular function. *Vasc. Biol.* **1**, H117–H124 (2019).
132. Wettschureck, N., Strilic, B. & Offermanns, S. Passing the Vascular Barrier: Endothelial Signaling Processes Controlling Extravasation. *Physiol. Rev.* **99**, 1467–1525 (2019).
133. Zeng, Y. *et al.* Tracing the first hematopoietic stem cell generation in human embryo by single-cell RNA sequencing. *Cell Res.* **29**, 881–894 (2019).
134. Schilling, K. *et al.* Translocation of Endothelial Nitric-Oxide Synthase Involves a Ternary Complex with Caveolin-1 and NOSTRIN. *Mol. Biol. Cell* **17**, 3870–3880 (2006).
135. Murthy, S. *et al.* Endothelial CaMKII as a regulator of eNOS activity and NO-mediated vasoreactivity. *PLoS ONE* **12**, e0186311 (2017).
136. Taha, A. A., Taha, M., Seebach, J. & Schnittler, H.-J. ARP2/3-mediated junction-associated lamellipodia control VE-cadherin–based cell junction dynamics and maintain monolayer integrity. *Mol. Biol. Cell* **25**, 245–256 (2014).

137. Wang, Y. L., Hui, Y. N., Guo, B. & Ma, J. X. Strengthening tight junctions of retinal microvascular endothelial cells by pericytes under normoxia and hypoxia involving angiopoietin-1 signal way. *Eye* **21**, 1501–1510 (2007).
138. Duvigneau, J. C., Esterbauer, H. & Kozlov, A. V. Role of Heme Oxygenase as a Modulator of Heme-Mediated Pathways. *Antioxidants* **8**, 475 (2019).
139. Rogero, M. M. & Calder, P. C. Obesity, Inflammation, Toll-Like Receptor 4 and Fatty Acids. *Nutrients* **10**, 432 (2018).
140. Luo, W. *et al.* Heme oxygenase-1 ameliorates oxidative stress-induced endothelial senescence via regulating endothelial nitric oxide synthase activation and coupling. *Aging* **10**, 1722–1744 (2018).
141. Di Pietro, P. *et al.* Sortilin evokes endothelial dysfunction and arterial hypertension through the dysregulation of sphingolipid metabolism and oxidative stress. *Eur. Heart J.* **41**, ehaa946.2704 (2020).
142. López-Novoa, J. M. & Bernabeu, C. The physiological role of endoglin in the cardiovascular system. *Am. J. Physiol.-Heart Circ. Physiol.* **299**, H959–H974 (2010).
143. Sangwung, P. *et al.* KLF2 and KLF4 control endothelial identity and vascular integrity. *JCI Insight* **2**, e91700.
144. Lundberg, J. O. & Weitzberg, E. Nitric oxide signaling in health and disease. *Cell* **185**, 2853–2878 (2022).
145. Jiang, H. *et al.* Mechanisms of Oxidized LDL-Mediated Endothelial Dysfunction and Its Consequences for the Development of Atherosclerosis. *Front. Cardiovasc. Med.* **9**, 925923 (2022).
146. Lilly, B. *et al.* Endothelial cell-induced cytoglobin expression in vascular smooth muscle cells contributes to modulation of nitric oxide. *Vascul. Pharmacol.* **110**, 7–15 (2018).
147. Liu, B. & Dai, Z. Fatty Acid Metabolism in Endothelial Cell. *Genes* **13**, 2301 (2022).
148. Ekmekçi, Ö. B. & Ekmekçi, H. Vitronectin in atherosclerotic disease. *Clin. Chim. Acta* **368**, 77–83 (2006).
149. Yaghoubi, A., Ghojazadeh, M., Abolhasani, S., Alikhah, H. & Khaki-Khatibi, F. Correlation of Serum Levels of Vitronectin, Malondialdehyde and Hs- CRP With Disease Severity in Coronary Artery Disease. *J. Cardiovasc. Thorac. Res.* **7**, 113–117 (2015).

150. Wang, Y. I. & Shuler, M. L. UniChip enables long-term recirculating unidirectional perfusion with gravity-driven flow for microphysiological systems. *Lab. Chip* **18**, 2563–2574 (2018).
151. Blüher, M. Obesity: global epidemiology and pathogenesis. *Nat. Rev. Endocrinol.* **15**, 288–298 (2019).
152. Ziegler, A. K. & Scheele, C. Human adipose depots' diverse functions and dysregulations during cardiometabolic disease. *Npj Metab. Health Dis.* **2**, 1–5 (2024).
153. Rodgers, A. & Sferruzzi-Perri, A. N. Developmental programming of offspring adipose tissue biology and obesity risk. *Int. J. Obes.* **45**, 1170–1192 (2021).
154. Emont, M. P. *et al.* A single-cell atlas of human and mouse white adipose tissue. *Nature* **603**, 926–933 (2022).
155. Vijay, J. *et al.* Single-cell analysis of human adipose tissue identifies depot- and disease-specific cell types. *Nat. Metab.* **2**, 97–109 (2020).
156. Gareev, I. *et al.* Therapeutic application of adipose-derived stromal vascular fraction in myocardial infarction. *iScience* **27**, 109791 (2024).
157. Sun, K. *et al.* Dichotomous effects of VEGF-A on adipose tissue dysfunction. *Proc. Natl. Acad. Sci. U. S. A.* **109**, 5874–5879 (2012).
158. Han, J. *et al.* The spatiotemporal development of adipose tissue. *Development* **138**, 5027–5037 (2011).
159. Rupnick, M. A. *et al.* Adipose tissue mass can be regulated through the vasculature. *Proc. Natl. Acad. Sci. U. S. A.* **99**, 10730–10735 (2002).
160. Cao, Y. Angiogenesis and Vascular Functions in Modulation of Obesity, Adipose Metabolism, and Insulin Sensitivity. *Cell Metab.* **18**, 478–489 (2013).
161. Farooqi, I. S. & Xu, Y. Translational potential of mouse models of human metabolic disease. *Cell* **187**, 4129–4143 (2024).
162. Klingelhutz, A. J. *et al.* Scaffold-free generation of uniform adipose spheroids for metabolism research and drug discovery. *Sci. Rep.* **8**, 523 (2018).
163. Al-Ghadban, S., Pursell, I. A., Diaz, Z. T., Herbst, K. L. & Bunnell, B. A. 3D Spheroids Derived from Human Lipedema ASCs Demonstrated Similar Adipogenic Differentiation Potential and ECM Remodeling to Non-Lipedema ASCs In Vitro. *Int. J. Mol. Sci.* **21**, 8350 (2020).
164. Mandl, M. *et al.* An organoid model derived from human adipose stem/progenitor cells to study adipose tissue physiology. *Adipocyte* **11**, 164–174 (2022).

165. Nolan, D. J. *et al.* Molecular Signatures of Tissue-Specific Microvascular Endothelial Cell Heterogeneity in Organ Maintenance and Regeneration. *Dev. Cell* **26**, 204–219 (2013).
166. Arganda-Carreras, I., Fernández-González, R., Muñoz-Barrutia, A. & Ortiz-De-Solorzano, C. 3D reconstruction of histological sections: Application to mammary gland tissue. *Microsc. Res. Tech.* **73**, 1019–1029 (2010).
167. Strzelecki, M., Yin, K., Talavera-López, C. & Martinez-Jimenez, C. P. Isolation of Nuclei from Flash-frozen Liver Tissue for Single-cell Multiomics. *J. Vis. Exp. JoVE* (2022) doi:10.3791/64792.
168. Gayoso, A. & Shor, J. JonathanShor/DoubletDetection: doubletdetection v4.2. Zenodo https://doi.org/10.5281/zenodo.6349517 (2022).
169. Korsunsky, I. *et al.* Fast, sensitive and accurate integration of single-cell data with Harmony. *Nat. Methods* **16**, 1289–1296 (2019).
170. Fang, Z., Liu, X. & Peltz, G. GSEApy: a comprehensive package for performing gene set enrichment analysis in Python. *Bioinforma. Oxf. Engl.* **39**, btac757 (2023).
171. Pico, A. R. *et al.* WikiPathways: Pathway Editing for the People. *PLOS Biol.* **6**, e184 (2008).
172. Szklarczyk, D. *et al.* STRING v10: protein-protein interaction networks, integrated over the tree of life. *Nucleic Acids Res.* **43**, D447-452 (2015).
173. Wirth, J. *et al.* Spatial transcriptomics using multiplexed deterministic barcoding in tissue. *Nat. Commun.* **14**, 1523 (2023).
174. Jin, S. *et al.* Inference and analysis of cell-cell communication using CellChat. *Nat. Commun.* **12**, 1088 (2021).
175. Heaton, H. *et al.* Souporcell: robust clustering of single-cell RNA-seq data by genotype without reference genotypes. *Nat. Methods* **17**, 615–620 (2020).
176. Bergandi, L. *et al.* Insulin Stimulates Glucose Transport Via Nitric Oxide/Cyclic GMP Pathway in Human Vascular Smooth Muscle Cells. *Arterioscler. Thromb. Vasc. Biol.* **23**, 2215–2221 (2003).
177. Ntambi, J. M. *et al.* Differentiation-induced gene expression in 3T3-L1 preadipocytes. Characterization of a differentially expressed gene encoding stearoyl-CoA desaturase. *J. Biol. Chem.* **263**, 17291–17300 (1988).
178. Ni, H. *et al.* MGP Regulates Perivascular Adipose-Derived Stem Cells Differentiation Toward Smooth Muscle Cells Via BMP2/SMAD Pathway

Enhancing Neointimal Formation. *Cell Transplant.* **31**, 09636897221075747 (2022).

179. Bolton, K. *et al.* Decorin is a secreted protein associated with obesity and type 2 diabetes. *Int. J. Obes.* **32**, 1113–1121 (2008).
180. Oguri, Y. *et al.* CD81 Controls Beige Fat Progenitor Cell Growth and Energy Balance via FAK Signaling. *Cell* **182**, 563-577.e20 (2020).
181. Angueira, A. R. *et al.* Defining the lineage of thermogenic perivascular adipose tissue. *Nat. Metab.* **3**, 469–484 (2021).
182. Chen, R., McVey, D. G., Shen, D., Huang, X. & Ye, S. Phenotypic Switching of Vascular Smooth Muscle Cells in Atherosclerosis. *J. Am. Heart Assoc.* **12**, e031121 (2023).
183. Hansson, B. *et al.* Adipose cell size changes are associated with a drastic actin remodeling. *Sci. Rep.* **9**, 12941 (2019).
184. Qiao, Q. *et al.* Adipocyte abundances of CES1, CRYAB, ENO1 and GANAB are modified in-vitro by glucose restriction and are associated with cellular remodelling during weight regain. *Adipocyte* **8**, 190–200 (2019).
185. Salameh, A. *et al.* Prohibitin/annexin 2 interaction regulates fatty acid transport in adipose tissue. *JCI Insight* **1**, e86351.
186. Kanehisa, M. & Goto, S. KEGG: Kyoto Encyclopedia of Genes and Genomes. *Nucleic Acids Res.* **28**, 27–30 (2000).
187. Wang, Y. *et al.* PDGFRα marks distinct perivascular populations with different osteogenic potential within adipose tissue. *Stem Cells Dayt. Ohio* **38**, 276–290 (2020).
188. He, T. *et al.* Suppression of preadipocyte determination by SOX4 limits white adipocyte hyperplasia in obesity. *iScience* **26**, 106289 (2023).
189. Sauer, T. *et al.* Protein Expression of AEBP1, MCM4, and FABP4 Differentiate Osteogenic, Adipogenic, and Mesenchymal Stromal Stem Cells. *Int. J. Mol. Sci.* **23**, 2568 (2022).
190. Freimert, C., Closs, E. I., Silbermann, M., Erfle, V. & Strauss, P. G. Isolation of a cathepsin B-encoding cDNA from murine osteogenic cells. *Gene* **103**, 259–261 (1991).
191. Choi, J.-W. *et al.* Enhanced Osteocyte Differentiation: Cathepsin D and L Secretion by Human Adipose-Derived Mesenchymal Stem Cells. *Cells* **12**, 2852 (2023).

192. Koli, K., Ryynänen, M. J. & Keski-Oja, J. Latent TGF-β binding proteins (LTBPs)-1 and -3 coordinate proliferation and osteogenic differentiation of human mesenchymal stem cells. *Bone* **43**, 679–688 (2008).
193. Wang, N. *et al.* LMO4 modulates proliferation and differentiation of 3T3-L1 preadipocytes. *FEBS Lett.* **587**, 3032–3037 (2013).
194. Walker, J. T., McLeod, K., Kim, S., Conway, S. J. & Hamilton, D. W. Periostin as a multifunctional modulator of the wound healing response. *Cell Tissue Res.* **365**, 453–465 (2016).
195. Han, C. Y. *et al.* Adipocyte-Derived Versican and Macrophage-Derived Biglycan Control Adipose Tissue Inflammation in Obesity. *Cell Rep.* **31**, 107818 (2020).
196. Yogi, A. *et al.* Differentiation of Adipose-Derived Stem Cells into Vascular Smooth Muscle Cells for Tissue Engineering Applications. *Biomedicines* **9**, 797 (2021).
197. Garza-Manero, S. *et al.* Maintenance of active chromatin states by HMGN2 is required for stem cell identity in a pluripotent stem cell model. *Epigenetics Chromatin* **12**, 73 (2019).
198. Cho, D. S., Lee, B. & Doles, J. D. Refining the adipose progenitor cell landscape in healthy and obese visceral adipose tissue using single-cell gene expression profiling. *Life Sci. Alliance* **2**, (2019).
199. Massier, L. *et al.* An integrated single cell and spatial transcriptomic map of human white adipose tissue. *Nat. Commun.* **14**, 1438 (2023).
200. Zhang, L. *et al.* Two-step regulation by matrix Gla protein in brown adipose cell differentiation. *Mol. Metab.* **80**, 101870 (2024).
201. Kern, J., Steurer, M., Gastl, G., Gunsilius, E. & Untergasser, G. Vasohibin inhibits angiogenic sprouting in vitro and supports vascular maturation processes in vivo. *BMC Cancer* **9**, 284 (2009).
202. Parmar, G. *et al.* Accessory subunit NDUFB4 participates in mitochondrial complex I supercomplex formation. *J. Biol. Chem.* **300**, (2024).
203. Kim, J., Kim, S.-K., Kim, H.-K., Mattson, M. P. & Hyun, D.-H. Mitochondrial Function in Human Neuroblastoma Cells Is Up-Regulated and Protected by NQO1, a Plasma Membrane Redox Enzyme. *PLOS ONE* **8**, e69030 (2013).
204. Barnett, S. N. *et al.* An organotypic atlas of human vascular cells. *Nat. Med.* **30**, 3468–3481 (2024).
205. Hermans, D. *et al.* Nectins and Nectin-like molecules drive vascular development and barrier function. *Angiogenesis* **26**, 349–362 (2023).

206. Tai-Nagara, I. *et al.* Placental labyrinth formation in mice requires endothelial FLRT2/UNC5B signaling. *Dev. Camb. Engl.* **144**, 2392–2401 (2017).
207. Bjarnegård, M. *et al.* Endothelium-specific ablation of PDGFB leads to pericyte loss and glomerular, cardiac and placental abnormalities. *Development* **131**, 1847–1857 (2004).
208. Lindahl, P., Johansson, B. R., Levéen, P. & Betsholtz, C. Pericyte loss and microaneurysm formation in PDGF-B-deficient mice. *Science* **277**, 242–245 (1997).
209. Meng, X., Nikolic-Paterson, D. J. & Lan, H. Y. TGF-β: the master regulator of fibrosis. *Nat. Rev. Nephrol.* **12**, 325–338 (2016).
210. Kang, J. H., Gimble, J. M. & Kaplan, D. L. In Vitro 3D Model for Human Vascularized Adipose Tissue. *Tissue Eng. Part A* **15**, 2227–2236 (2009).
211. Doherty, E. L., Aw, W. Y., Hickey, A. J. & Polacheck, W. J. Microfluidic and Organ-on-a-Chip Approaches to Investigate Cellular and Microenvironmental Contributions to Cardiovascular Function and Pathology. *Front. Bioeng. Biotechnol.* **9**, (2021).
212. Huttala, O., Sarkanen, J.-R., Heinonen, T. & Ylikomi, T. Presence of Vasculature Results in Faster Insulin Response in Adipocytes in Novel In Vitro Vascularized Adipose Tissue Model. 16 (2019).
213. Paek, J. *et al.* Microphysiological Engineering of Self-Assembled and Perfusable Microvascular Beds for the Production of Vascularized Three-Dimensional Human Microtissues. *ACS Nano* **13**, 7627–7643 (2019).
214. Adeniran-Catlett, A. E. *et al.* Accelerated adipogenic differentiation of hMSCs in a microfluidic shear stimulation platform. *Biotechnol. Prog.* **32**, 440–446 (2016).
215. Olmer, R. *et al.* Differentiation of Human Pluripotent Stem Cells into Functional Endothelial Cells in Scalable Suspension Culture. *Stem Cell Rep.* **10**, 1657–1672 (2018).

8 Material and media composition

8.1.1 Material list

Name	Company	Product number
2-Mercaptoethanol	Sigma Aldrich	M6250
Accutase	Sigma Aldrich	A6964
Agarose, Standard	Carl Roth	3810.2
AM-1 medium	Zen-Bio	088AM-1
B27 supplement (-Vitamin A)	Life Technologies	12587010
BMP4	PeproTech	120- 05ET-10
BODIPY	Life Technologies	D3922
BSA, fatty acid free	Sigma Aldrich	A8806
CellROX	Sigma Aldrich	C10444
CHIR 99021	Axon Medchem BV	1385
Chromium Next GEM Single Cell 3' Kit v3.1	10x Genomics	1000269
Collagen I hydrogel	Corning	354236
Collagenase P	Roche	11213857001
DAPI	Sigma Aldrich	62248
DM-2 medium	Zen-Bio	088DM-2
DMEM/F12	Thermo Fisher Scientific	31330038
DMSO, cell culture grade	Th. Geyer	APP A3672,0250
Dounce tissue grinder set	Th. Geyer	9651617
DPBS (-Mg/-Ca)	Sigma Aldrich	D8537
EGM-2	Sigma Aldrich	C-22011
Ethanol, cell culture grade	Merck	1.59010
FBS, research grade+	Sigma Aldrich	F0804
FGF-2	Miltenyi Biotech	130-093-838
Fibronectin, bovine	Life Technologies	33010018
Filter MINISART PLUS 0.20 µm sterile	Sartorius	17597----------K
FITC-Dextran	Sigma Aldrich	FD2000S
Flowmi cell filter (40 µm)	Th. Geyer	1183242
Forskolin	Abcam	ab120058
Glucose Uptake-Glo Assay	Promega	J1342
GlutaMax supplement	Thermo Fisher Scientific	35050038
Glycerol assay kit	Sigma Aldrich	MAK117-1KT

Name	Company	Product number
Glycine	Sigma Aldrich	G5417
Histofix (4% PFA)	Carl Roth	P087.4
Hoechst33342	Thermo Fisher Scientific	62249
Human adipose-derived stem cells	ZenBio	ASC-F
Insulin solution, human recombinant	Sigma Aldrich	I9278-5ML
Krebs-Ringer Solution, HEPES-buffered	Thermo Fisher Scientific	J67795.AP
Lenti-X™ p24 Rapid Titer Kit	Takara	631476
L-Glutamine	Sigma Aldrich	25030024
Lipofectamine 2000	Thermo Fisher Scientific	11668019
Matrigel (hESC qualified)	Corning	354277
Microslides µ-Slide 15 Well 3D,untreated	Ibidi	81501
mTeSR plus medium	StemCell Technologies	05825
MycoSensor PCR assay kit	Agilent Technology	302109
N2 supplement	Thermo Fisher Scientific	17502048
Neurobasal Medium	Life Technologies	21103049
Nitric Oxide Assay Kit	Sigma Aldrich	MAK454
OCT	Carl Roth	6478.2
OxLDL (from human plasma)	Life Technologies	L34357
OxLDL Dil-labeled	Life Technologies	L34358
PBS (10x)	Thermo Fisher Scientific	AM9624
Penicillin/Streptomycin	Thermo Fisher Scientific	15140122
Phalloidin-iFluor(TM) 647	Abcam	ab176759
Pluristrainer	pluriSelect	43-50020-023
PM-1 medium	Zen-Bio	088PM-1
pMD2.G plasmid	Sigma Aldrich	12259
psPAX2 plasmid	Sigma Aldrich	12260
Puromycin dihydrochloride	Santa Cruz	sc-108071
Rock inhibitor Y-27632 dihydrochloride	Abcam	HY-10583
SafeSeal SurPhob tips, 200 µl	Biozym	VT0240
shRNA mission vectors	Sigma Aldrich	CSTVRS
StemPro-34	Life Technologies	10639011
Sucrose	Sigma Aldrich	S0389

Name	Company	Product number
TBHP	Abcam	ab113851
Triton X-100	Sigma Aldrich	93443
TrypanBlue solution 0.4%	Sigma Aldrich	15250061
Trypsin-EDTA 0.05%	Sigma Aldrich	T4174
Tween 20 (10%)	BioRad	1610781
TY52156	Sigma Aldrich	5330620001
Ultra-low attachment plates	Corning	3471
Vectashield plus antifade	Biozol	VEC-H-1900-10
VEGFA	PeproTech	10-20-100

8.1.2 Antibody list

Name	Company	RRID Identifier	Host species	Dilution	Purpose
Alexa Fluor 488 anti-mouse (secondary)	Thermo Fisher Scientific	AB_141607	Donkey	1:500	IHC-Whmt/ IHC-Frz/ IHC-P
Alexa Fluor 555 anti-rabbit (secondary)	Thermo Fisher Scientific	AB_162543	Donkey	1:500	IHC-Whmt/ IHC-Frz/ IHC-P
Alexa Fluor 647 anti-mouse (secondary)	Thermo Fisher Scientific	AB_2535809	Goat	1:500	IHC-Whmt/ IHC-Frz/ IHC-P
αSMA	Thermo Fisher Scientific	AB_557419	Mouse	1:200	IHC-Whmt/ IHC-Frz
Angiopoietin2	Thermo Fisher Scientific	AB_2544773	Rabbit	1:100-1:1000	IHC-P
ARP3	Sigma Aldrich	AB_476749	Mouse	1:500	IHC-P
CD140b-PE labelled	BD	AB_397132	Mouse	2 µL/ 10^5 cells	FC/FACS
CD31-FITC labelled	BD	AB_395838	Mouse	2 µL/ 10^5 cells	FC/FACS
Claudin5	Thermo Fisher Scientific	AB_2809891	Rabbit	1:50-1:200	IHC-P

Name	Company	RRID Identifier	Host species	Dilution	Purpose
Collagen IV	Abcam	AB_305584	Rabbit	1:50	IHC-Frz
DLL4	Cell Signaling	AB_2800263	Rabbit	1:400	IHC-P
GLUT4	Abcam	AB_2191441	Rabbit	1:500	IHC-Frz
KLF4	Thermo Fisher Scientific	AB_2898967	Rabbit	1:50-1:200	IHC-P
CD31	Thermo Fisher Scientific	AB_10981955	Rabbit	1:100	IHC-Whmt/ IHC-Frz/ IHC-P
CD31	Cell Signaling	AB_2160882	Mouse	1:1000 (IHC-P) 1:400 (IHC-Frz)	IHC-Frz/ IHC-P
Perilipin1	Cell Signaling	AB_10829911	Rabbit	1:150	IHC-Frz
VE-Cadherin	Cell Signaling	AB_2077970	Rabbit	1:100	IHC-Whmt

8.1.3 Media and buffer composition

N2B27 medium[29,215]

Reagent	Stock concentration	Volume (mL)
DMEM/F12		50
Neurobasal medium		50
B27 (- Vitamin A)	50x	2
N2	100x	1
2-Mercaptoethanol	100%	0.1
Pen/Strep	100x	1
GlutaMax	100x	1

StemPro-34 complete medium

Reagent	Stock concentration	Volume (mL)
StemPro-34 medium		500
StemPro-34 supplement		13
L-Glutamine	200 mM	5
Pen/Strep	100x	5
Glutamax	100x	5

ECGM medium

Reagent	Stock concentration	Volume
StemPro-34 complete		8.5 mL
FBS		1.5 mL
VEGF	100 µg/mL	10 µL
FGF-2	100 µg/mL	10 µL

Collagen I Neutralization solution

Recipe for 1 mL neutralized Collagen I hydrogel (Corning, 4.63 mg/mL, LOT 2124001)

Reagent	Stock concentration	Volume (µL)
PBS 10x	10x	100
Water		351.99
NaOH	1 M	8.0459

Cell-hydrogel-extraction solution

Reagent	Stock concentration	Volume
Collagenase P solution		Mix well and store at -20°C until use.
Collagenase P	1.7 IU/mg	10.6 mg
DPBS		1 mL
Cell-hydrogel-extraction solution		Always prepare freshly before use.
Collagenase P solution		500 µL
Accutase		500 µL